POLITECNICO DI TORINO

Laurea Magistrale in Ingegneria Aerospaziale e Astronautica

Master Degree Thesis

Experimental assessment of nozzle flow unsteadiness through optical techniques

Supervisors

Prof. E. MARTELLI

Dr.ir. F.F.J. SCHRIJER

Dr. W.J. BAARS

Candidate

GLORIA NALLO

APRIL 2025

Ad Andrea e Miriam

Summary

This study presents a comparative experimental investigation of two key flow unsteadiness phenomena in an overexpanded thrust-optimized parabolic (TOP) rocket nozzle: the transition from Free Shock Separation (FSS) to Restricted Shock Separation (RSS) and the onset of the End Effect Regime (EER). Using a combination of high-speed Schlieren imaging, oil film visualization, and synchronized wall pressure measurements, the study explores the unsteady dynamics of flow separation and reattachment at varying Nozzle Pressure Ratios (NPR). Higher NPR visualization of cap shock is also shown and presented.

A new truncated TOP nozzle was designed and tested in a cold-flow nozzle test rig at Delft University of Technology. The truncation influences flow behavior, leading to the onset of EER at lower NPR values (∼26) compared to a non-truncated TOP nozzle. This experimental setup allowed for a detailed analysis of flow unsteadiness associated with EER and the FSS-RSS transition, including a frequency analysis performed on the exhaust plume Schlieren visualizations.

Pressure measurements confirm that the FSS-RSS transition occurs at an NPR of approximately 22, with a sudden reattachment of the FSS-induced shock to the nozzle wall. This results in strong pressure fluctuations, asymmetry-driven side loads, and the characteristic hysteresis effects between startup and shutdown conditions. At higher NPR, the End Effect Regime manifests as a global unsteady pulsation of the most downstream separation bubble, driven by external flow interactions at the nozzle lip and intermittent flow oscillations, but without hysteresis.

Comparative CFD simulations using RANS-based models successfully capture key flow structures and show strong coherence with experimental pressure data and internal nozzle flow behavior, even with the limitations of steady-state turbulence modeling.

These findings provide valuable insights into shock-induced unsteadiness in thrust optimized nozzles, contributing to the design optimization of high-thrust propulsion systems, where understanding and mitigating flow separation and side loads are critical for structural integrity and performance.

Acknowledgements

From the very beginning of my academic journey, my passion for space and rocket science has been a driving force, and much of this enthusiasm was nurtured within the lively environment of PoliTo Rocket Team. Working alongside such talented and driven colleagues — first and foremost friends —was an incredibly enriching experience that not only deepened my love for this field but also filled me with immense inspiration. The collaborative spirit and shared passion created a truly unique atmosphere where learning and growth felt as natural as having fun together.

I would like to thank my supervisor, Prof. E. Martelli from my university, an invaluable reference figure who instilled and fueled in me a passion for rocket science to the point where I now want to pursue it as my career. I am also deeply grateful for his availability, research, and precious knowledge sharing throughout the thesis project.

I would also like to express my gratitude to Dr. ir. F.F.J. Schrijer and Dr. ir. W.J. Baars from TU Delft, for their continuous help, guidance, and for welcoming me into the High Speed Lab as one of their own. They took the time to explain everything I needed to do while also giving me the autonomy and confidence to carry out my work, and they trusted me to take on important responsibilities in the use of the wind tunnel for conducting my experiments.

A sincere thank you to all the HSL laboratory technicians whose expertise and dedication were instrumental in ensuring the success of the experiments. Their hard work behind the scenes and their kind availability made this research possible, and I am deeply grateful for your contributions and helpfulness.

To my family, my guide, I simply owe you everything. A special thank you to Giuseppe Francesco and Vittoria, my brother and sister, and my biggest inspirations. To Carla and Benedetta, who, despite the physical distance, have always been incredibly close—you have believed in me, often more than I believed in myself. With love and gratitude to my colleagues and friends met at Politecnico, I will never forget your support and the moments we shared, which made everything feel lighter. Last but not least, to Emanuele, as I always say, and I mean it, half of

this degree belongs to you.

Table of Contents

List of Tables

List of Figures

Acronyms

CTIC Compressed Truncated Ideal Contoured nozzles.

CFD Computational Fluid Dynamics.

DNS Direct Numerical Simulation.

EER End-Effect Regime.

FFT Fast Fourier Transform.

FSCD Flow Separation Control Device.

FSI Fluid-Structure Interaction.

FSS Free Shock Separation.

NPR Nozzle Pressure Ratio.

PBS Polarizing Beam Splitter.

RSS partial Restricted Shock Separation.

PIV Particle Image Velocimetry.

PSD Power Spectral Density.

QWP Quarter-Wave Plate.

RANS Reynolds-Averaged Navier-Stokes.

RSS Restricted Shock Separation.

SSME Space Shuttle Main Engine.

SWBLI Shock Wave Boundary Layer Interaction.

TIC Truncated Ideal Contour.

TOC Thrust Optimized Contour.

TOP Thrust Optimized Parabolic contour.

Chapter 1

Introduction

Launch vehicles, known as rockets, represent some of the most sophisticated and challenging engineering achievements in human history. To break free from Earth's gravitational pull, these vehicles rely on powerful propulsion systems that generate the necessary momentum. Chemical rocket propulsion systems are typically composed of a propellant feed system, a combustion chamber, and an exhaust nozzle. The exhaust nozzle, in particular, plays a critical role in converting the internal energy of the propellants into kinetic energy by accelerating the combustion gases to their maximum velocity before they exit the nozzle. This acceleration is fundamental to produce the high thrust required for the rocket's ascent.

The principles governing rocket performance are captured in two fundamental equations of rocketry. The first is the Tsiolkovsky rocket equation, which highlights how the change in the rocket's velocity (Δv) depends directly on the exhaust velocity (v_e) of the combustion gases and the ratio of the rocket's initial mass (m_i) to its final mass (m_f):

$$\Delta v = v_e \ln\left(\frac{m_i}{m_f}\right) \tag{1.1}$$

The second is the thrust equation, which shows that maximizing exhaust velocity not only increases Δv but also enhances the thrust by contributing to the momentum term of the equation:

$$F = \dot{m} v_e + (p_e - p_a) A_e \tag{1.2}$$

These equations underline two fundamental design objectives for rockets: achieving the highest possible exhaust velocity and optimizing the mass by minimizing structural mass. The latter is crucial because the rocket must expel as much mass as possible through propellant consumption while retaining the smallest possible residual mass, optimizing the thrust-to-weight ratio.

The performance of the exhaust nozzle is influenced by its shape and the pressure ratio between the combustion chamber and the ambient environment. Ideally, the nozzle's design should ensure that the pressure of the gases at the exit plane (p_e) matches the ambient pressure (p_a), maximizing thrust through optimal expansion. However, as rockets ascend through varying atmospheric conditions, the ambient pressure changes, requiring engineers to select a specific design point at which optimal expansion occurs. For many modern launch vehicles, particularly those utilizing high-area-ratio Thrust Optimized Parabolic (TOP) nozzles, the design is often optimized for high-altitude, which means low-pressure environments. This is because, according to ideal rocket theory, expanding the gases to a low p_e increases the exhaust velocity v_e, enhancing performance at higher altitudes.

One significant challenge with this design choice is that engines operating at sea level experience overexpanded flow conditions. When the pressure in the combustion chamber ramps up from ambient to nominal operating pressure during startup (as the turbopump system accelerates), the nozzle flow may encounter extreme adverse pressure gradients. These conditions can induce flow separation inside the nozzle, particularly during the transitional states of Free Shock Separation (FSS), Restricted Shock Separation (RSS), and the End Effect Regime (EER). Asymmetric flow separation, in particular, can generate severe vibroacoustic loads and off-axis forces, leading to the so called side loads and consequently to potential structural damage. Historical examples include the J-2S engine, which detached from its gimbal structure, and the Space Shuttle Main Engine (SSME), which suffered from fatigue cracks and ruptured coolant lines. Similar issues have been documented in the Japanese LE-7A and the European Vulcain engines.

To address these challenges, nozzle design must not only withstand high side loads but also manage or predict the unsteady behavior of shock-induced flow separation. However, predicting precisely the magnitude of these side loads is complex due to the intricate interactions between exhaust gases and nozzle structures and the turbulence of boundary layer separation. While small-scale tests provide insights, they cannot replicate full-scale operational conditions, necessitating expensive full-scale engine tests late in the design process. These limitations drive the need for innovative research approaches that combine experimental testing with numerical simulations. In this context, cold flow experiments play an important role, as they provide valuable insights into flow behavior and separation dynamics, offering more comprehensive data compared to numerical simulations alone.

In light of this, the Aerospace Engineering faculty at Delft University of Technology has developed in 2021 a dedicated nozzle testing facility within a supersonic tunnel. This facility aims to bridge the gap between theoretical models and real-world applications by enabling detailed studies of fluid-structure interactions during startup and shutdown phases. The setup offers an opportunity to gather high-quality quantitative data, contributing to the study of rocket nozzle optimal designs.

This thesis builds upon and advances this line of research by detailing the complete process of designing, analyzing, and testing a new rocket nozzle, based on previous designs. Chapter 2 presents a comprehensive review of relevant literature, setting the foundation for the detailed test nozzle design described in Chapter 3. The experimental methodology and data processing techniques are thoroughly discussed in Chapters 4 and 5, respectively, with the key results and final conclusions presented in Chapters 6 and 7.

1.1 Research Objective and Questions

The objective of the research is defined as follows:

"The objective of this research is to experimentally investigate flow unsteadiness phenomena in a truncated Thrust-Optimized Parabolic (TOP) rocket nozzle, utilizing the TU Delft nozzle test setup. This study focuses on capturing and analyzing unsteady flow behaviors, particularly gaining insights into the end-effect regime. To accomplish this, a range of experimental techniques will be employed, including oil film visualization, synchronized wall pressure measurements, and high-speed Schlieren imaging. Additionally, the research aims to conduct an exhaust plume frequency analysis and validate the experimental findings against CFD simulations."

Building on this objective, the thesis is guided by several key research questions:

1. FSS to RSS Transition and End-Effect Regime:
   (a) At what NPR do unsteady phenomena occur?
   (b) What are the flow characteristics that distinguish Free Shock Separation (FSS), Restricted Shock Separation (RSS), and the End-Effect Regime (EER)?
   (c) What are the specific flow features linked to the End Effect Regime?
   (d) Are the experimental data coherent with previous literature findings?
   (e) How do experimental data compare to the CFD analyses results?
   (f) What are the dominant frequency characteristics of the instabilities in the exhaust plume for different NPR conditions?
2. Visualization techniques:
   (a) How do different visualization techniques compare in capturing flow separation phenomena?

(b) How does the use of oil film visualization complement optical techniques in identifying separation lines and flow reattachment?

(c) Can the implementation of a Focusing Schlieren setup provide deeper insights into the three-dimensional effects in the unsteady flow separation phenomena?

Chapter 2

Literature review

This chapter aims at presenting a literature overview of nozzle flow dynamics, including nozzle flow dynamics fundamentals, shock wave interactions and unsteady phenomena, as well as an overview of different flow visualization techniques and of frequency analysis theory.

2.1 Nozzle flow dynamics fundamentals

A nozzle is a channel with a variable cross-sectional area designed to control fluid flow. Within a nozzle, the pressure of the fluid decreases while its kinetic energy increases. The primary nozzle configurations include the convergent nozzle, where subsonic expansion occurs, and the convergent-divergent, or de Laval nozzle, used for supersonic expansion. The design of the latter relies on Hugoniot's theorem, which relates the area and Mach number in a supersonic flow channel. Nozzle theory is well-established and widely applied in various propulsion systems. Extensive experimental data also exists for jet flow characteristics, further validating the theoretical framework.

2.1.1 Ideal nozzle

An ideal nozzle operates under the assumption of isentropic flow, wherein the flow process is both adiabatic (no heat transfer) and reversible (no frictional losses). Under these conditions, energy losses are minimized, allowing for the efficient conversion of thermal energy into kinetic energy, thereby maximizing thrust performance. The behavior of the flow within an ideal nozzle is governed by the conservation laws of mass, momentum, and energy, providing a robust theoretical model for nozzle performance prediction.

In a typical nozzle flow process, the fluid enters the settling chamber at high pressure and temperature, where total and static thermodynamic conditions are initially equivalent. As the flow expands through the convergent-divergent nozzle, it undergoes acceleration, potentially achieving supersonic velocities at the exit. The isentropic flow relations form the basis for the governing equations, enabling accurate characterization of the nozzle's performance.

A critical parameter in the analysis of nozzle performance is the Nozzle Pressure Ratio (NPR), defined as the ratio of the total pressure in the settling chamber to the ambient pressure at the nozzle exit. When the NPR exceeds the critical pressure ratio, determined using a Mach number M=1 in isentropic flow equations, the flow becomes supersonic downstream of the throat (where M=1). This supersonic transition is essential for achieving optimal thrust in high-speed propulsion systems.

In practical rocket applications, truncated ideal contours (TIC) are frequently employed as a compromise between the theoretical performance of a full-length ideal nozzle and the physical constraints of spacecraft design. The TIC nozzle maintains near-optimal thrust performance while offering a reduced length, thereby improving feasibility and integration within rocket architectures. Examples of TIC designs include the LR-115, Viking, and RD-0120 nozzles.

Ahlberg et al.R [1] introduced a graphical methodology for identifying the optimal truncation point of TIC nozzles. This approach involves plotting a complete set of ideal nozzle contours alongside lines representing constant surface area, exit diameter, length, and vacuum thrust coefficient. Within specific design constraints—such as expansion ratio, surface area, or nozzle length—an optimization process can then be conducted to determine the truncation point that maximizes performance while meeting practical design requirements.

2.1.2 TOP nozzle

A Thrust Optimized Parabolic (TOP) nozzle is specifically engineered to enhance performance at sea level, addressing the critical challenge of flow separation. This design differs from a Thrust Optimized Contour (TOC) nozzle primarily in the location of the internal shock. In a TOC nozzle, the shock forms downstream of the last left-running characteristic line, ensuring wall pressure remains unaffected by the shock. Conversely, in a TOP nozzle, the shock occurs upstream of this characteristic line, resulting in a higher wall pressure at the nozzle exit. This increased exit pressure provides a valuable margin against flow separation, which is crucial in sea-level operation where ambient pressure is high.

A notable example of this approach is the Space Shuttle Main Engine (SSME) nozzle, which initially featured a TOC design. However, computational studies indicated that the exit wall pressure would be approximately 31% of ambient sea-level pressure, a condition associated with high separation risk. To mitigate this, engineers performed a parametric study of TOP nozzle contours, exploring various parabolic designs. The optimized TOP design introduced additional flow turning, generating an internal shock that increased the exit pressure by 24% while sacrificing only 0.1% nozzle efficiency. This strategic design adjustment enabled the SSME nozzle to operate reliably at sea level, combining high performance with stability.

The Vulcain engine nozzle also adopted a parabolic contour, leveraging the TOP nozzle advantages for European Ariane launch vehicles. The higher wall pressure at the nozzle exit not only prevents flow separation but also enhances operational robustness during the liftoff phase, where pressure fluctuations are most pronounced. Overall, the TOP nozzle design offers an important balance between efficiency and reliability, particularly in multi-environment missions where engines must perform effectively from sea level to vacuum conditions.

2.1.3 Exhaust Plume

Rocket engines designed for first or main-stage propulsion, including the American Space Shuttle Main Engine (SSME), the European Vulcain, and the Japanese LE-7, are engineered to function effectively across a broad spectrum of ambient pressures, from approximately 1 bar at sea level to near-vacuum conditions at high altitudes. As the rocket ascends, the ambient pressure around the nozzle significantly drops, leading to distinct flow regimes: overexpanded, adapted, and underexpanded flow conditions.

Overexpanded Flow

At low altitudes, the ambient pressure exceeds the nozzle exit pressure, resulting in an overexpanded flow condition. In this scenario, the exhaust flow must adjust to the high ambient pressure through a network of oblique shocks and expansion waves, giving the exhaust plume its characteristic barrel-like shape.
Different shock patterns can occur in overexpanded nozzles, including:

- **Classical Mach Disk**: Associated with strong overexpansion, featuring a normal shock along the centerline of the exhaust flow.
- **Cap-Shock Pattern**: Typically found in nozzles with internal shocks (e.g., TOC, TOP, and CTIC nozzles), and characterized by a distinctive cap-like shock structure.
- **Apparent Regular Shock Reflection**: Occurs when the degree of overexpansion is reduced, allowing the exhaust flow to adapt to the ambient pressure without forming a Mach disk.

For ideal and TIC nozzles, as the overexpansion decreases, the exhaust flow may transition from a Mach disk pattern to an apparent regular shock reflection. This transition happens when mildly overexpanded flows adapt to ambient conditions without generating intense shock systems. Conversely, nozzles with internal shocks, such as TOC, TOP, and CTIC, tend to produce the cap-shock pattern. This behavior is depicted in Figure 2.1 (b), which illustrates the Vulcain nozzle's exhaust plume with a parabolic contour. Experimental studies on sub-scale models conducted by the European Flow Separation Control Device (FSCD) group have also confirmed the stable presence of the cap-shock pattern in parabolic sub-scale rocket nozzles.

Adapted Flow

During the ascent, there is a phase where the ambient pressure matches the nozzle exit pressure, achieving adapted flow conditions. At this point, the exhaust plume appears well-collimated, and shock structures are minimized, indicating peak nozzle performance. However, this condition is typically short-lived, as the ambient pressure continues to drop with increasing altitude.

Underexpanded Flow

When the rocket reaches high altitudes, the ambient pressure becomes much lower than the nozzle exit pressure, leading to an underexpanded flow. The exhaust gases continue to expand beyond the nozzle exit, resulting in a broad and visibly expanded exhaust plume. This phenomenon is clearly visible in images like Figure 2.1 (d), captured during a Saturn 1-B launch, where the large plume behind the rocket demonstrates the ongoing expansion of exhaust gases.

Transient Startup and Shutdown Behavior

During the startup and shutdown phases of the rocket engine, the Nozzle Pressure Ratio (NPR) undergoes dynamic changes. At startup, the NPR increases, guiding the nozzle through overexpanded, adapted, and potentially underexpanded flow states. During shutdown, this sequence is reversed as the NPR decreases. These transient behaviors are crucial for designing rocket nozzles that should allow to manage rapid pressure changes safely.

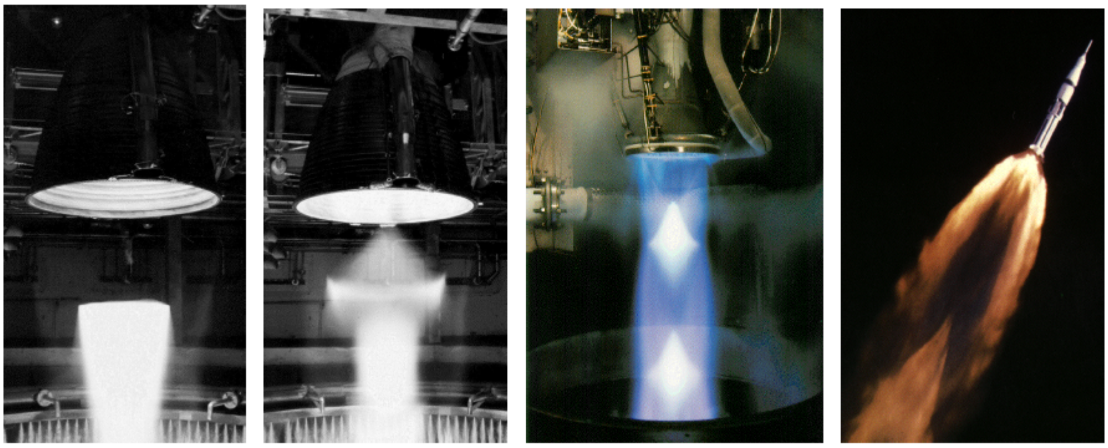

Figure 2.1: Exhaust plume pattern: (a) Vulcain, overexpanded flow with Mach disk, (b) Vulcain, overexpanded flow with cap-shock pattern, (c) RL10-A5, overexpanded flow with apparent regular reflection, (d) underexpanded flow, photographed during launch of Saturn 1-B (Courtesy: SNECMA, CNES, NASA).

2.2 Shock Wave Boundary Layer Interaction

Shock wave boundary layer interactions (SWBLI) play a crucial role in understanding the flow field within rocket nozzles, especially under supersonic conditions. Before diving into the specifics of nozzle flow behavior, it is important to grasp the fundamental concepts of how shock waves interact with boundary layers, as established through studies on canonical flat-plate supersonic boundary layers.

The boundary layer's shape significantly influences how it responds to incoming shock waves. In rocket nozzles, the boundary layer is typically turbulent, exhibiting a low shape factor and a full velocity profile. Unlike laminar flows, where the Reynolds number might play a substantial role, high-speed turbulent boundary layers are predominantly governed by inertial forces, making the shape factor the primary parameter in SWBLI considerations.

Shock wave boundary layer interactions can manifest as either weak or strong interactions. In weak interactions, the boundary layer remains attached to the surface, while in strong interactions, it separates from the wall. This discussion focuses on strong interactions, as they are associated with flow separation and are more relevant to rocket nozzle flows. When strong interactions occur, the boundary layer separation may be followed by reattachment downstream, leading to the formation of a separation bubble. According to Babinsky and Harvey [4], the pressure distribution within this bubble allows it to be modeled as a quasi-isobaric "dead air" region, wedge-shaped and bounded by a slip line.

In a typical strong interaction scenario, the incoming shock wave (C1) initiates

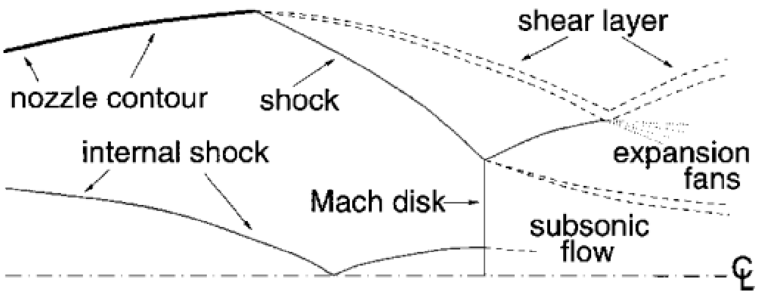

(a) Mach disk

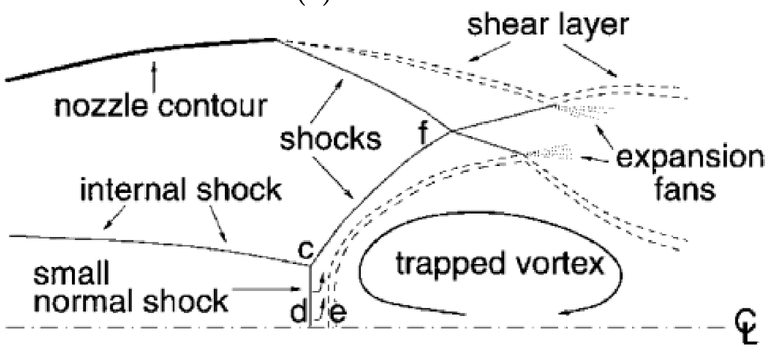

(b) Cap-shock pattern with trapped vortex

Figure 2.2: Shock patterns in the exhaust plume of a thrust-optimized nozzle with internal shock [2]

the boundary layer separation. The separation bubble's isobaric region generates an oblique separation shock (C2), which interacts with the primary shock wave. The reflected shock (C4) strikes the isobaric region at a specific point (I), immediately followed by an expansion fan to maintain a smooth pressure distribution. If the flow reattaches, an additional oblique shock (C5) forms. Whether the flow reattaches or not is highly influenced by whether the incoming shock is normal or oblique.

The interaction between shock waves and turbulent boundary layers is rarely steady. Instead, SWBLI exhibits dynamic behavior, which can significantly impact side-load generation in rocket nozzles. The unsteady nature of SWBLI is particularly critical because the highest side loads often coincide with regions of elevated heat transfer, amplifying the adverse effects of unsteady separation in real world applications. Experimental and numerical studies, particularly on flat-plate compressive ramps, have shed light on this unsteady behavior.

A key finding from these studies is that the unsteadiness frequency of SWBLI is much lower than the characteristic frequency of the turbulent boundary layer, $\frac{U_\infty}{\delta_i}$, and the flow behavior in the interaction region is highly intermittent. One

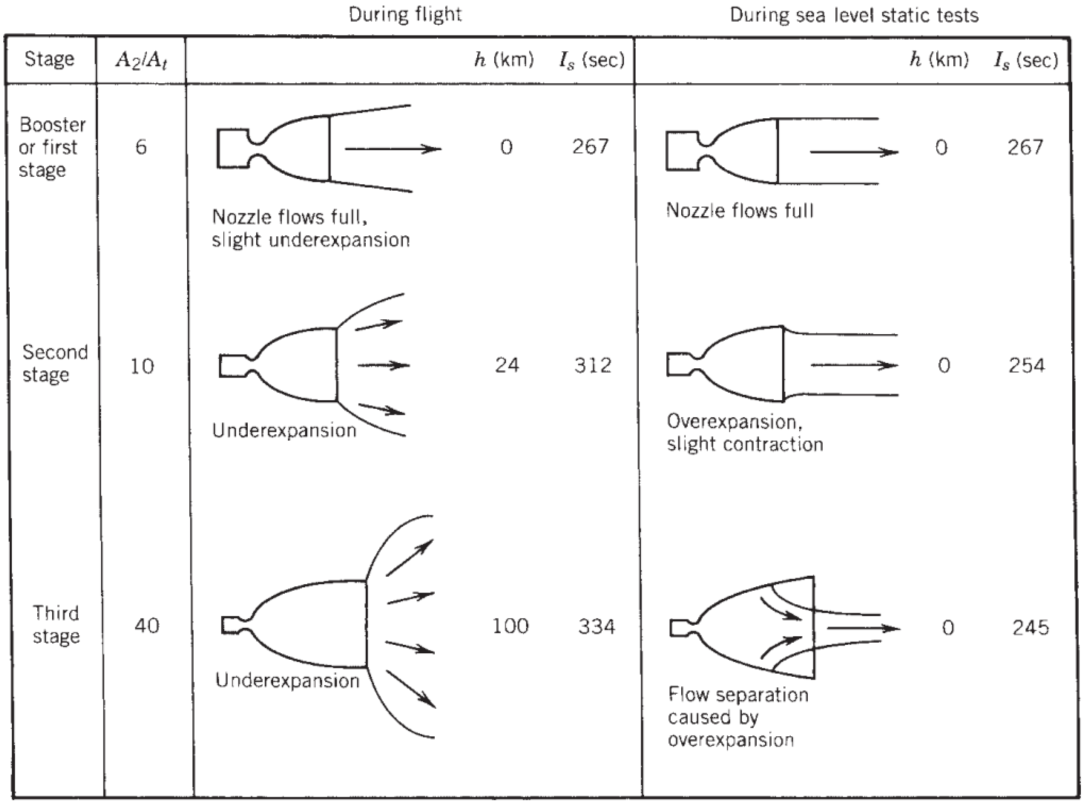

Figure 2.3: Simplified sketches of three different flow regimes in rocket engine nozzles [3]

important metric to characterize this unsteadiness is the maximum zero-crossing frequency ($f_{c,max}$), which measures how often the shock foot crosses a specific point within the intermittent region per second. Since this frequency varies across the region, the maximum frequency is typically used for analysis. Dolling's research [6] indicated that the Strouhal number, defined as:

$$St = \frac{f_{c,max} L_i}{U_\infty} \tag{2.1}$$

where L_i is the length of the intermittent region and U_∞ is the free stream velocity, generally falls within the range of 0.01 to 0.03 for flat-plate, zero-pressure gradient boundary layers. Further studies by Dussauge et al. [7] found that this Strouhal number remains relatively constant across different geometries and Mach numbers, offering a valuable scaling parameter when comparing full-scale rocket nozzles with smaller-scale experimental setups.

When the natural frequency of a rocket nozzle's structure approaches the

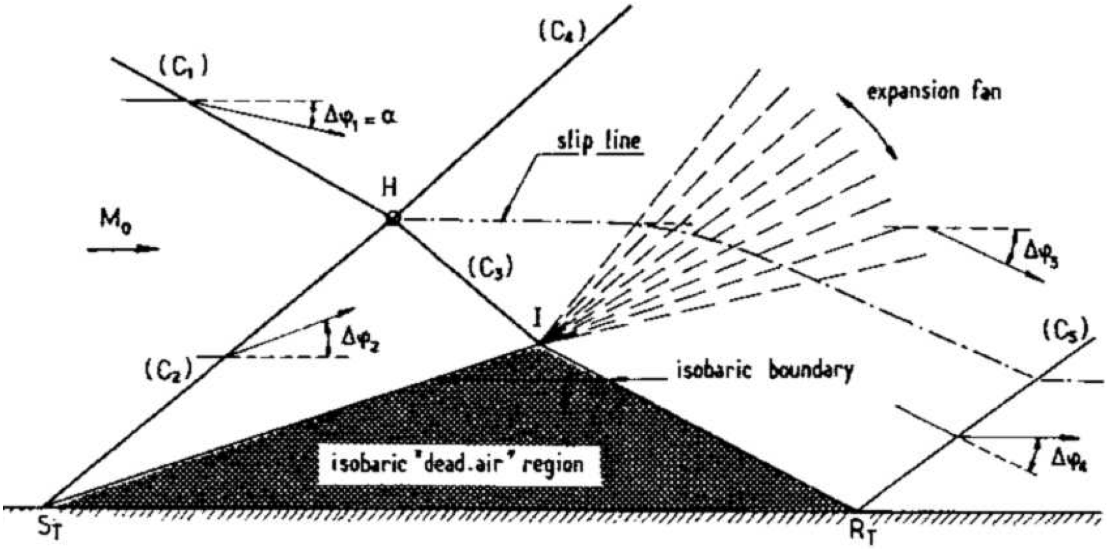

Figure 2.4: Inviscid shock wave interaction with boundary layer as suggested by Délery and Marvin [5]

maximum zero-crossing frequency, resonance could occur due to fluid-structure interactions. Such resonance may lead to substantial increases in side loads, posing risks to nozzle integrity.

The underlying causes of SWBLI unsteadiness have been widely debated. Some researchers, such as Erengil and Dolling [8], suggest that pressure fluctuations in the incoming boundary layer contribute to this behavior. Ünalmis and Dolling [9] proposed that low-frequency thickening and thinning of the boundary layer might drive the unsteadiness, while Beresh et al. [10] attributed it to fluctuations in the shape factor of the boundary layer. Ganapathisubramani et al. [11] added another perspective, linking the unsteadiness to alternations between low and high momentum regions within the boundary layer.

Other theories focus on the separation bubble's intrinsic unsteadiness, independent of upstream flow conditions. Piponniau et al. [12] argued that the bubble's unsteadiness might stem from vortex shedding within the mixing layer post-separation. This hypothesis was supported by direct numerical simulations (DNS) conducted by Priebe and Martin [13].

It is likely that SWBLI unsteadiness arises from a combination of upstream boundary layer effects and downstream separation bubble dynamics. Large-scale flapping motions of the separation bubble could be influenced by downstream conditions, whereas small-scale unsteadiness might primarily depend on upstream boundary layer characteristics. This complex interplay of factors makes SWBLI a critical area of study for optimizing rocket nozzle design and performance, particularly under varying operational conditions.

2.3 Flow separation

Flow separation within rocket nozzles is a critical phenomenon influencing nozzle performance, particularly at low Nozzle Pressure Ratios (NPR). The internal flow structures become increasingly complex as the NPR decreases, with notable differences between startup and shutdown behaviors. Two primary types of flow separation structures are identified in rocket nozzles: Free Shock Separation (FSS) and Restricted Shock Separation (RSS). While FSS can occur in any nozzle type, RSS is specific to Thrust Optimized Parabolic (TOP) nozzles due to the interaction between the internal shock and the Mach disk. Although these flow structures are often represented in two-dimensional schematics, they actually manifest as annular structures around the entire nozzle. The origins of the End Effect Regime is also presented.

The foundational understanding of flow separation originates from Prandtl's 1904 work [14], which demonstrated that low-friction flows around bodies can be divided into two distinct regions: a thin boundary layer near the surface and a potential flow region where friction effects are negligible. Within the boundary layer, the no-slip condition at the wall leads to a velocity profile that is significantly influenced by both frictional forces and the acceleration from the outer flow. The static pressure, which remains relatively uniform across the boundary layer, is governed by the main flow.

When the wall pressure gradient is favorable or zero, the boundary layer typically remains attached to the wall. However, an adverse wall pressure gradient—where the pressure increases in the flow direction—can lead to flow separation. In such cases, fluid particles close to the wall, having lower kinetic energy due to reduced velocities, may not withstand the rising pressure. This can cause the flow to reverse and generate a recirculation region near the wall.

Flow separation thus requires both friction and an adverse pressure gradient. If either of these conditions is mitigated, separation can be prevented. Prandtl's experiments, such as those involving flow around rotating cylinders or diffusers with boundary layer suction, effectively demonstrated methods to prevent flow separation. Moreover, if the adverse pressure gradient is weak, the natural momentum exchange within the boundary layer may supply enough kinetic energy to the particles at the wall, allowing them to resist flow reversal. Turbulent boundary layers, characterized by a higher lateral exchange of momentum, tend to separate later than laminar boundary layers, where momentum transfer is limited to molecular motion.

This understanding of flow separation is essential for discussing the specific mechanisms of FSS and RSS phenomena, as well as the Extreme Expansion Ratio

(EER) effects that influence rocket nozzle operation at varying altitudes and pressure conditions.

2.3.1 Free Shock Separation

Free Shock Separation (FSS) in an overexpanded nozzle occurs when the flow separates from the nozzle wall at a specific, low pressure ratio between the internal wall pressure and the ambient pressure and the main cause is the adverse pressure gradient. A schematic representation of the phenomenology, illustrating the wall pressure profile, compression and expansion waves, and the boundary shear layer edge, is provided by Frey and Hagemann [2] and depicted in Figure 2.5.

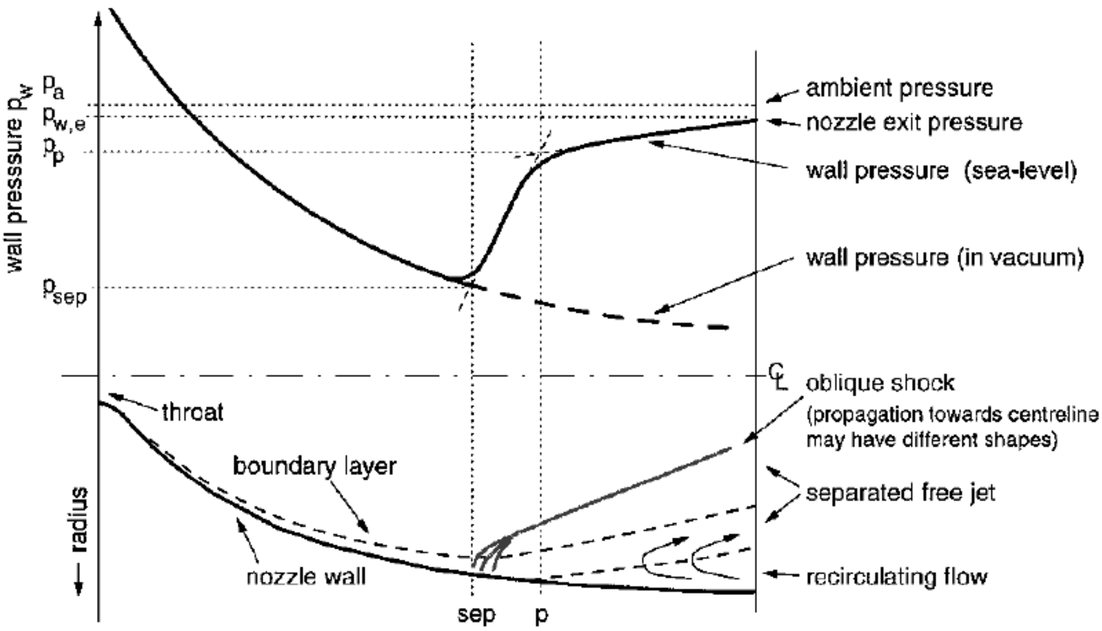

Figure 2.5: Schematic sketch of the flow in FSS configuration [2]

The separation process generates an oblique separation shock, which undergoes direct Mach reflection at the nozzle centerline, resulting in the formation of a Mach disk in the central region of the nozzle. The phenomenon of FSS is characterized by an initial drop in pressure at the incipient separation point (p_i), followed by a rapid rise to a plateau pressure, which is slightly lower than the ambient pressure (p_a). The separation shock is highly unsteady, with low-frequency oscillations dominating the motion of the separation point between the initial detachment location and the plateau pressure region. These oscillations account for up to 80-90% of the total energy below a given frequency threshold, contributing to pressure fluctuations along the nozzle wall.

Experimental studies have shown that after separation, the wall pressure does not remain constant but gradually increases from p_p to p_e due to the inflow of ambient gas and the recirculation effects in the downstream region. This gradual rise in pressure is a distinguishing feature of FSS and has been observed in many cold gas tests. Historically, it has been noted that the ratio of separation to ambient pressure (p_i/p_a) decreases with increasing nozzle pressure ratio (p_0/p_a), a trend attributed to Mach number effects. However, when the separation point nears the nozzle exit—approximately at 80% of the nozzle's length—this trend reverses. Instead of continuing to decrease, p_i/p_a starts increasing as the plateau pressure approaches ambient pressure. At this stage, the flow appears to be attached to the nozzle exit, but pressure sensors still detect a distinct pressure rise, known as incipient separation at the exit. This reversal in behavior is crucial in understanding the transition between different separation regimes and has significant implications for nozzle performance, pressure loads, and overall stability.

2.3.2 Restricted Shock Separation

Restricted Shock Separation (RSS) is a distinct flow phenomenon occurring in highly overexpanded nozzles at relatively high nozzle pressure ratios (NPR), where the separated flow reattaches to the nozzle wall after separation. Unlike Free Shock Separation (FSS), in which the separated flow remains detached from the nozzle wall, RSS results in the formation of one or multiple annular separation bubbles along the nozzle wall due to the interaction of the internal shock with the nozzle centerline. This reflection creates a radially outward momentum that exceeds the radially inward momentum generated by the separation shock, forcing the flow back onto the nozzle wall and leading to reattachment. The interaction pattern between the internal shock, reflected or conical shock, and the separation shock is referred to as a cap shock pattern [2, 15].
The existence of a recirculation region behind the Mach stem in the RSS regime has been confirmed by several studies [**88**, **89**]. Due to non-uniformities in the upstream kernel flow, the Mach stem is not perfectly straight, leading to variations in shock strength. This generates radial velocity and entropy gradients, enhancing downstream vorticity. The resulting vortex can obstruct the kernel flow by introducing a radial flow component directed toward the nozzle wall [**76**, **87**]. Furthermore, the pressure distribution in the RSS regime is considerably more complex than in FSS. The presence of reattachment shocks causes localized pressure increases above atmospheric levels, just behind the separation bubble [**12**]. Additionally, the pressure rise across the separation shock in RSS is lower than in FSS due to a weaker adverse pressure gradient. Consequently, the separation point in RSS shifts further downstream compared to FSS [**12**]. During the transition from FSS to RSS, or vice versa, the separation point undergoes rapid movement

upstream or downstream. In some cases, the flow oscillates between FSS and RSS, a phenomenon known as *partial RSS* (pRSS) [**90**].

The transition from FSS to RSS occurs at a well-defined pressure ratio, during which a closed recirculation zone forms with static pressures significantly below ambient levels [**8**, **3**]. As chamber pressure increases further, the reattachment point migrates toward the nozzle exit, eventually causing the recirculation zone to open into the ambient flow. This leads to a pressure rise behind the separation shock, which forces the separation point upstream once again, resulting in a cyclic opening and closing of the recirculation zone [**3**, **8**]. This periodic transition between RSS and FSS is known as the *end effect* [**3**, **8**]. Similar behavior is observed during nozzle shutdown, where the transition from FSS to

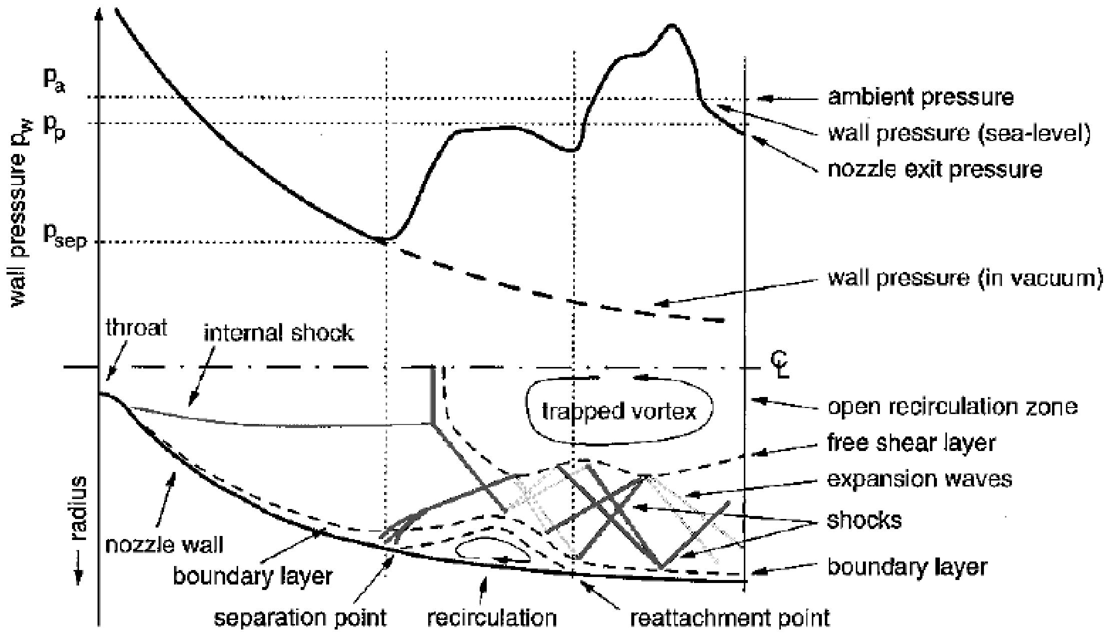

Figure 2.6: Schematic sketch of the flow in RSS configuration [2]

2.3.3 End Effect Regime

At higher nozzle pressure ratio, the transition from the FSS to the RSS flow condition gives rise to an additional unsteady effect known as the "End Effect Regime" (EER). This phenomenon, less analyzed in literature and experiments with respect to the previous two, occurs prior to achieving stable nominal flow conditions and is characterized by another peak in side loads, which manifests when the reattachment point reaches the nozzle exit [16]. Frey and Hagemann [17] proposed that this peak may be attributed to a self-sustained periodic oscillation

between the FSS and RSS regimes, potentially driven by the pressure differential between the ambient environment and the plateau pressure within the recirculation bubble.
The EER is marked by significant global unsteadiness and substantial wall pressure fluctuations at high pressure ratios. This global quasi-axial pulsation results in extreme levels of fluctuations, with side loads influenced by minor pressure differences superimposed upon a substantial axisymmetric global unsteadiness. The structure of the RSS configuration maintains its form while moving downstream as the chamber-to-ambient pressure ratio increases. Once the reattachment line reaches the nozzle lip, the recirculation bubble transitions to open to the ambient atmosphere. Experimental results published for thrust-optimized contour nozzles [18, 19, 20] indicate that the end-effects regime typically exhibits high side loads comparable to the peak levels observed just before the FSS to RSS transition.

2.3.4 Hysteresis effects

Numerous studies have highlighted the presence of significant hysteresis in the transition from FSS to RSS, particularly between startup and shutdown phases [2, 15]. These investigations reveal that the NPR required for the FSS to RSS transition during startup is much higher than that observed during shutdown. Interestingly, the EER appears unaffected by this hysteresis. The difference is substantial, with startup transition NPR reaching 32, whereas during shutdown, it is only 14, as found in the tests conducted by Hagemann et al. [15]. They also observe minor variations in the separation pressure ratio p_i/p_p between startup and shutdown, which results in slightly altered separation points. Given that the normal shock location remains stable, the conical shock exerts a radially outward momentum at lower NPR, enabling the flow to remain attached for a longer time. Additionally, the recirculation zone behind the Mach stem might stay relatively stable at lower NPR, continuing to block the kernel flow. According to Martelli et al. [22], hysteresis is only observed when the transition point is considered as a function of NPR, but it completely vanishes when the plateau pressure ratio p_c/p_p is taken into account instead.

2.4 Side loads and aeroelasticity

Side loads in rocket nozzles are lateral forces acting perpendicular to the thrust direction, imposing structural stress, potentially destabilizing the launcher, and increasing the risk of engine failure. These forces arise due to the complex flow dynamics within the nozzle.

During the operational phases of a rocket nozzle, side loads are always present, but they reach their peak intensity during startup and shutdown phases. According

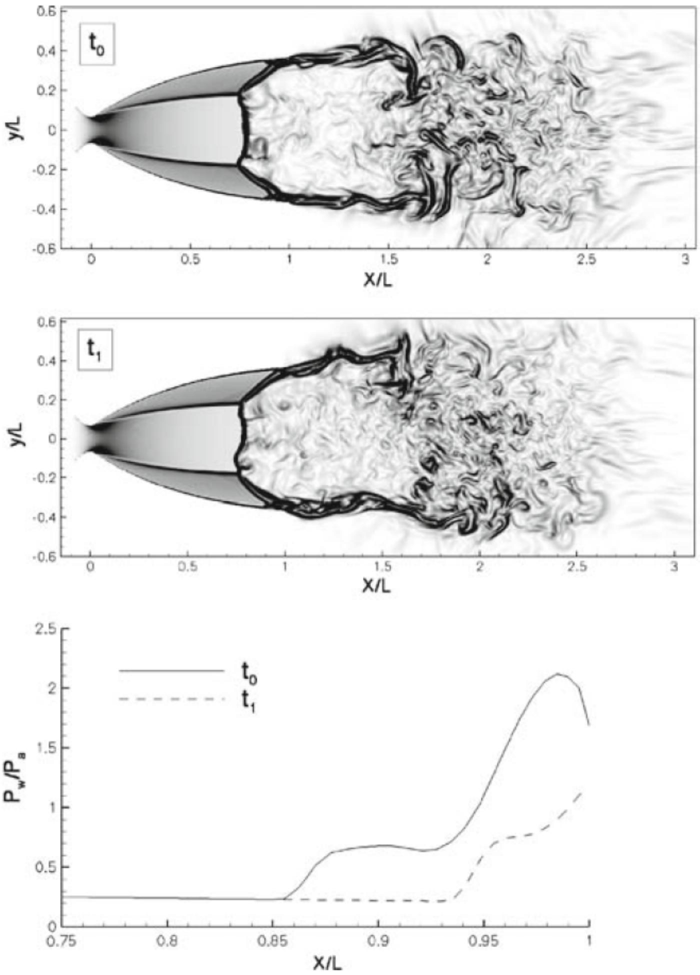

Figure 2.7: RSS and EER numerical schlieren and streamwise wall pressure distribution on the upper wall (Y/L > 0) at two instants of the cycle [21]

to Hagemann et al. [15], several factors contribute to elevated side loads during these transients. One significant factor is the aforementioned transition between Free Shock Separation (FSS) and Restricted Shock Separation (RSS) flow structures, which can introduce considerable asymmetry in the flow behavior.

Additionally, a globally asymmetrical separation line within the nozzle can generate uneven pressure distributions, leading to lateral forces. Unsteady pressure fluctuations, either at the separation point or in the downstream flow region, also contribute to side load generation, as these oscillations can produce dynamic imbalances. Furthermore, the interaction between the aerodynamic flow and the structural dynamics of the nozzle—known as fluid-structure interaction (FSI)—can amplify these loads, especially when coupled with aeroelastic effects. External

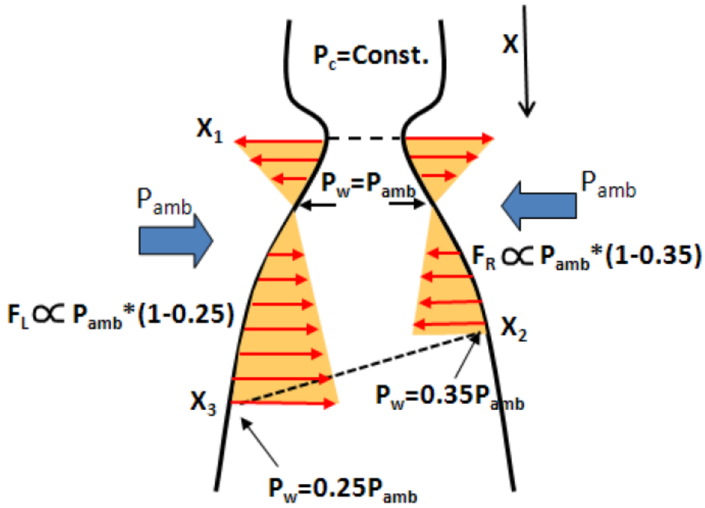

Figure 2.8: Simple schematic of the aerodynamics forces that cause side loads [23]

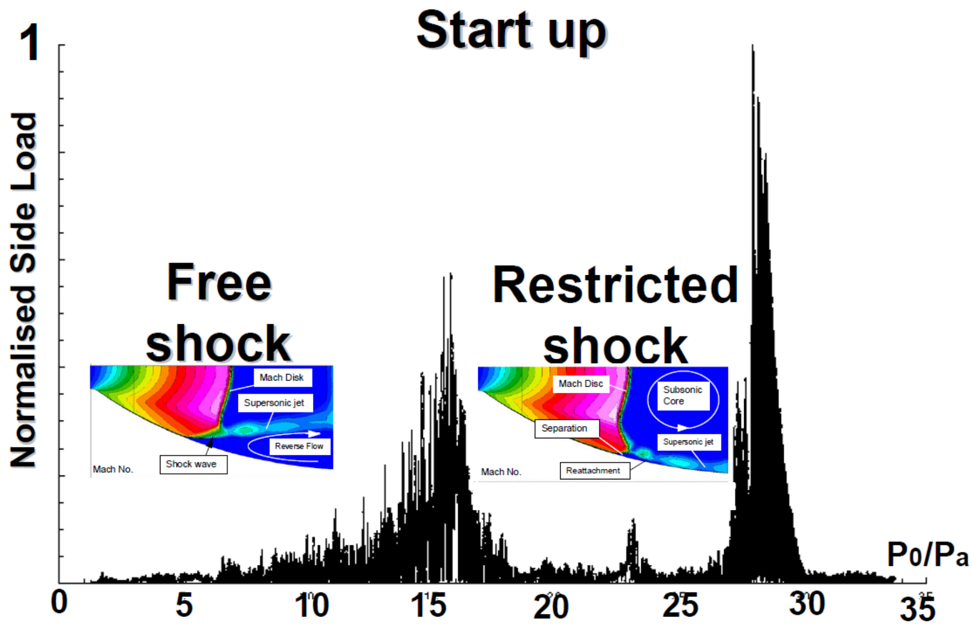

Figure 2.9: Normalised side load torque vs. feeding to ambient pressure ratio during start up [24]

pressure instabilities in the surrounding environment and asymmetries in the hardware design further exacerbate the issue.

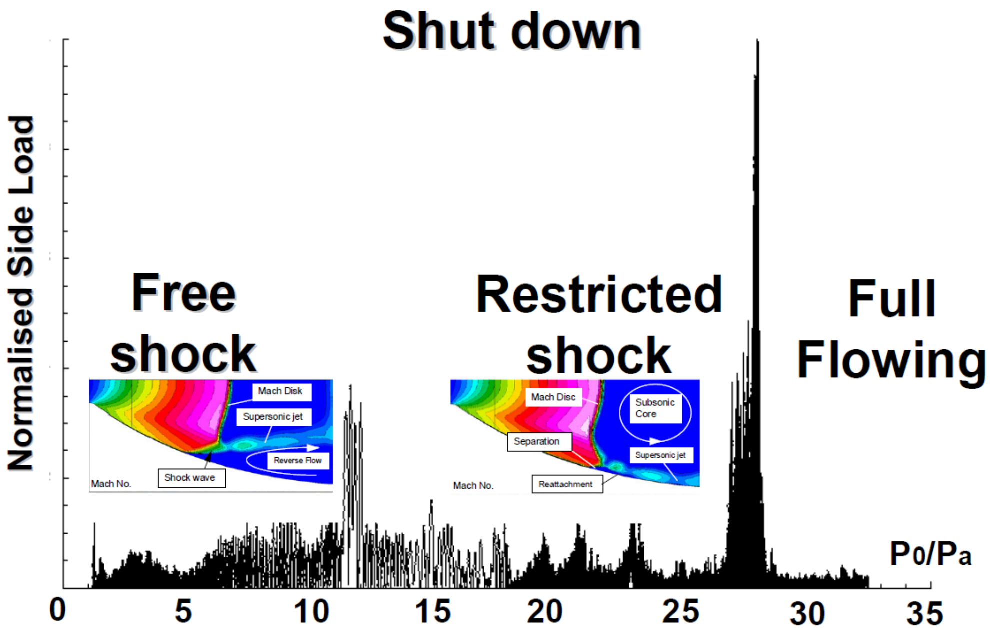

Figure 2.10: Normalised side load torque vs. feeding to ambient pressure ratio during shut down [24]

Among these contributing factors, the focus of the current research is on aerodynamic side loads driven by asymmetric flow separation, unsteady pressure behavior, and fluid-structure coupling. It is crucial to distinguish between aerodynamic and structural side loads, as the latter can be intensified through FSI mechanisms, which can lead to significant structural stress. A major source of side loads is the non-uniform flow separation within the nozzle. When the internal flow becomes overexpanded—meaning the exhaust pressure drops below the surrounding atmospheric pressure—shock-induced separation occurs, disrupting the flow symmetry. Boundary layer separation, influenced by varying boundary layer thicknesses along the nozzle walls, generates localized low-pressure zones that contribute to asymmetric flow patterns. Even in well-designed nozzles, turbulent flow can introduce random and unpredictable asymmetries, further complicating load behavior. Flow-induced oscillations and resonance effects also play a critical role in generating side loads. Some nozzles exhibit low-frequency oscillations due to the cyclic process of flow separation and reattachment, leading to pulsating lateral forces. When these oscillations resonate with the natural frequencies of the rocket structure, the impact of side loads can be significantly magnified. Additionally, acoustic interactions within the nozzle can enhance side loads, particularly in larger engines, where the interaction of acoustic waves with separation phenomena can amplify the resulting forces. This section delves deeper into the mechanisms behind side load generation,

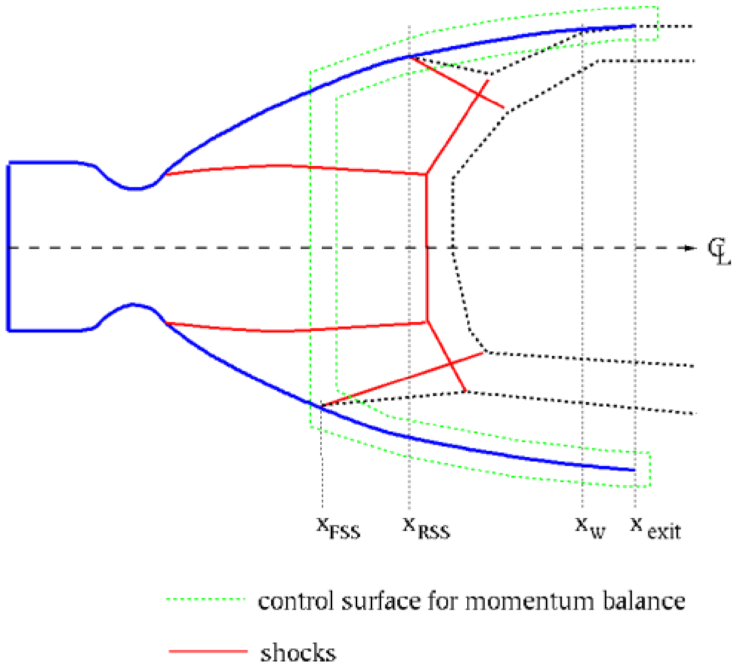

Figure 2.11: Asymmetric flowfield inside nozzle at instant of FSS-RSS transition [24]

exploring the influence of asymmetric separation, pressure pulsations, and fluid-structure interactions. It also examines the asymmetric separation line model as a predictive tool and discusses the broader implications of FSI and aeroelasticity on rocket nozzle performance.

2.5 Visualization techniques

2.5.1 Schlieren

The schlieren technique is an optical method widely used to qualitatively visualize changes in the density of transparent media such as air, water, or gases. It achieves this by detecting the deflection of light rays as they traverse regions with varying refractive indices. These density variations—often arising from differences in temperature or pressure—result in visual patterns that can be recorded on a screen or captured with a camera. Developed in the 19th century, schlieren imaging has become an essential tool in fluid dynamics and aerodynamics for studying phenomena such as shock waves, turbulence, and thermal convection with high sensitivity and precision.

Non-intrusive, optical-based methods like schlieren take advantage of the fact that light refracts when passing through an inhomogeneous, compressible medium. According to the Gladstone-Dale relation, the refractive index n of a gas is given by

$$n = 1 + K\rho \tag{2.2}$$

where K is the Gladstone-Dale constant (approximately $2 \times 10^{-4}\,\mathrm{m^3/kg}$ for air) and ρ is the density. Additionally, when light encounters a boundary between two substances with different refractive indices, it is bent according to Snell's law:

$$n_1 \sin\theta_1 = n_2 \sin\theta_2 \tag{2.3}$$

More specifically, in gaseous media, light rays are invariably deflected toward regions of higher density.

By illuminating a test region with a point-source light that has been shaped through a series of lenses and mirrors—as illustrated in Figure 2.12—a schlieren image of the phenomenon can be obtained. In such an image, spatial density gradients $\nabla\rho$ in an otherwise transparent medium become visible. According to [25], the change in image intensity is proportional to these density gradients:

$$\frac{\Delta I}{I} = \frac{f}{a} K W \frac{\partial\rho}{\partial x} \tag{2.4}$$

where f is the focal length of the camera, a is the fraction of light hitting the camera sensor, W is the width of the light source, and K is the Gladstone-Dale constant.

One of the distinguishing features of schlieren imaging, compared to techniques like shadowgraphy, is the use of a knife-edge. After light passes through the test section, a parabolic mirror is used to focus the light, and a knife-edge is strategically placed at the focal point. This knife-edge blocks a significant portion of the light that has not been deflected by density gradients, while allowing bent rays to pass through and reach the camera sensor. The result is an image where variations in pixel intensity directly correspond to changes in the medium's density. The sensitivity of the system is directly related to the amount of light blocked by the knife-edge; a smaller value of a leads to higher sensitivity in detecting density changes.

Without the knife-edge, all refracted and non-refracted rays continue to the camera sensor. The system now records variations in light intensity caused by second-order density gradients rather than first-order gradients. The result is a shadowgraph image, where changes in brightness correspond to regions of varying density, but with less edge definition compared to Schlieren.

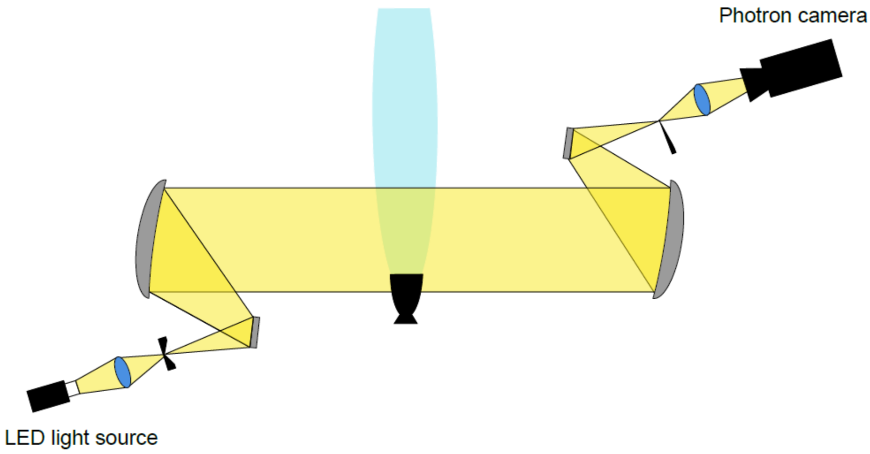

Figure 2.12: Z-type Schlieren scheme [26]

2.5.2 Focusing Schlieren

The focusing schlieren technique is an advanced version of the traditional schlieren method and offers better spatial resolution and flexibility. Like traditional schlieren, the focusing schlieren technique relies on the deflection of light rays caused by refractive index variations in a fluid. By utilizing a structured light pattern and a carefully designed lens system, this technique captures detailed images of aerodynamics phenomena with enhanced depth resolution. It stands out from traditional Schlieren methods by offering adjustable focus capabilities, enabling to explore complex three-dimensional dynamics and removing disruptions caused by density gradients outside the target area, allowing for more precise observations.
Two different configurations exist: the common focusing schlieren and the self-aligning focusing schlieren.
The first setup, illustrated in various studies ([27]), involves a combination of optical components including a light source, Fresnel lens, source grid, Schlieren lens, cutoff grid, condenser lens, and a digital camera, all mounted on precision translation stages and optical rails. The source and cutoff grids, which consist of alternating opaque and transparent slices, function similarly to the light source and knife edge in a traditional Schlieren setup, but with the added complexity of providing multiple light sources and knife edges. This design, along with the Schlieren lens, achieves the unique narrow depth of focus characteristic of this technique. However, there are significant challenges associated with implementing a focused Schlieren system that make it less attractive. The first challenge is the manufacturing of the cutoff grid, which requires extremely small spacings to achieve the desired focal depth, demanding high precision that is often achieved using laser cutting techniques. The second challenge is the alignment of the optical components, which requires higher

than usual levels of accuracy to ensure the system functions correctly. Despite these challenges, the necessary optical components are generally accessible, with many available from specialized suppliers at reasonable costs. When designing a focused Schlieren system, it is crucial to consider the various parameters that govern its performance, such as sensitivity, depth of focus, image resolution, and field of view. A closed system of equations can be employed to model the setup and optimize these parameters before determining grid spacing and the distances between components. Prematurely minimizing any single parameter can impose unnecessary constraints on the design, leading to suboptimal performance. Given that focusing Schlieren is not a widely used method, a careful and systematic approach is required to determine acceptable values for these variables, ensuring that the system meets the specific goals of the experiment.

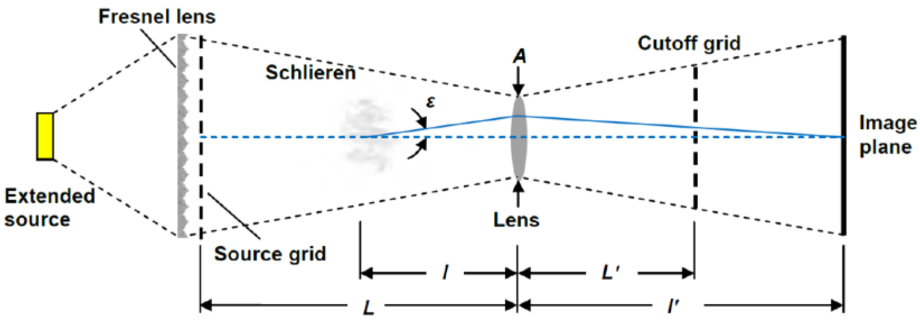

Figure 2.13: Focusing Schlieren scheme

Secondly, here is presented a compact, self-aligned focusing schlieren system that simplifies experimental setups by removing the need for separate source and cutoff grids, reducing alignment complexity. It adjusts sensitivity through light polarization, preventing glare and reflections. Unpolarized light passes through a polarizing beam splitter (PBS), creating vertically polarized light that moves through a grid, polarizing prism, and quarter-wave plate (QWP), becoming right-circularly polarized. After passing through the test object and reflecting off a retroreflective background, the light changes to left-circularly polarized, re-passing the object for increased sensitivity. The system enhances imaging by refocusing and polarization adjustment, transmitting the light to an imaging sensor for analysis.

Although the second setup was considered, the classic setup was ultimately chosen for the experiments due to the difficulty in sourcing specific components, which were limited in availability, costly and time-consuming because of shipping times. The experimental setup implementation of the technique is detailed in the following chapters.

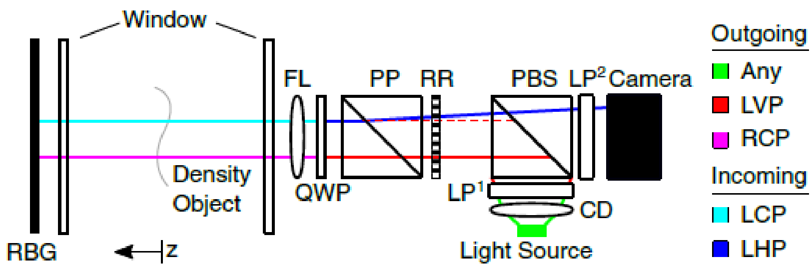

Figure 2.14: Self-aligning Focusing Schlieren scheme

2.5.3 Oil film

Shock wave boundary layer interactions, although often studied under the assumption of two-dimensionality, are inherently three-dimensional phenomena. The random and three-dimensional nature of velocity fluctuations distorts the separation line spanwise, leading to irregular patterns. This three-dimensionality is evident in oil flow visualizations such as those by Settles [28], where streamwise streaks of varying lengths and spacings downstream of the separation line highlight spanwise motion.

Oil film visualization is a widely used technique for analyzing flow patterns, particularly within boundary layers, and for identifying critical points like flow separation. This method provides insights into fluid-surface interactions and helps assess turbulence effects on flow behavior [29]. The technique relies on applying a specially prepared paint mixture that moves with the surface oil under aerodynamic forces during wind tunnel tests, leaving visible streaks that indicate flow direction. The paint must remain stable during the test until the desired conditions are achieved and dry sufficiently to resist gravity once the airflow ceases.

The procedure for applying the paint varies depending on the experimental requirements. In nozzle flow experiments, the paint is applied to the nozzle's internal walls, unlike in wind tunnels where it is commonly applied to the windows. Streak patterns form as the oil flows, depositing pigments in the wakes of small pigment concentrations, eventually creating elongated streaks aligned with the flow.

Proper surface preparation is crucial for effective oil film application. The surface is usually pre-wet using a medium applied with a soaked rag. For larger surfaces, a foam roller is often employed at a slight angle to ensure uniform coverage, while brushes are used for finer applications, requiring circular motions to achieve consistency.

The principles behind the oil film technique are similar across high-speed and low-speed wind tunnels, although in high-speed applications, the choice of oil medium is critical for ensuring stability during extended tests. Paint mixtures differ between laboratories, with additives and pigments tailored for specific needs. Titanium dioxide (TiO_2) is an opaque pigment that provides high contrast on dark surfaces but requires additives to prevent clumping. For light surfaces, Lampblack, a carbon-based pigment, is preferred due to its larger particle size, ensuring stable patterns. Kaolin (China clay), which becomes transparent when wet, is effective for distinguishing laminar and turbulent regions once dried. Fluorescent pigments like Dayglo enhance visibility and contrast, making them ideal for high-visibility tests.

The only previous example found in literature for oil flow technique specifically applied to rocket test nozzles in cold flow is from Verma and Haidn [30], where they use it to investigate the shock motions and related flow characteristics during restricted shock separation (RSS) conditions. Their experimental investigation, carried out in the P6.2 cold gas facility at DLR Lampoldshausen, focused on a subscale thrust optimized parabolic nozzle. The study revealed the presence of both translational ("flapping") and spanwise ("rippling") motions of the separation shock, as well as low-frequency expansion and contraction of the separation bubble. These results demonstrate the capability of the oil flow technique in visualizing complex shock behaviors under cold flow conditions.

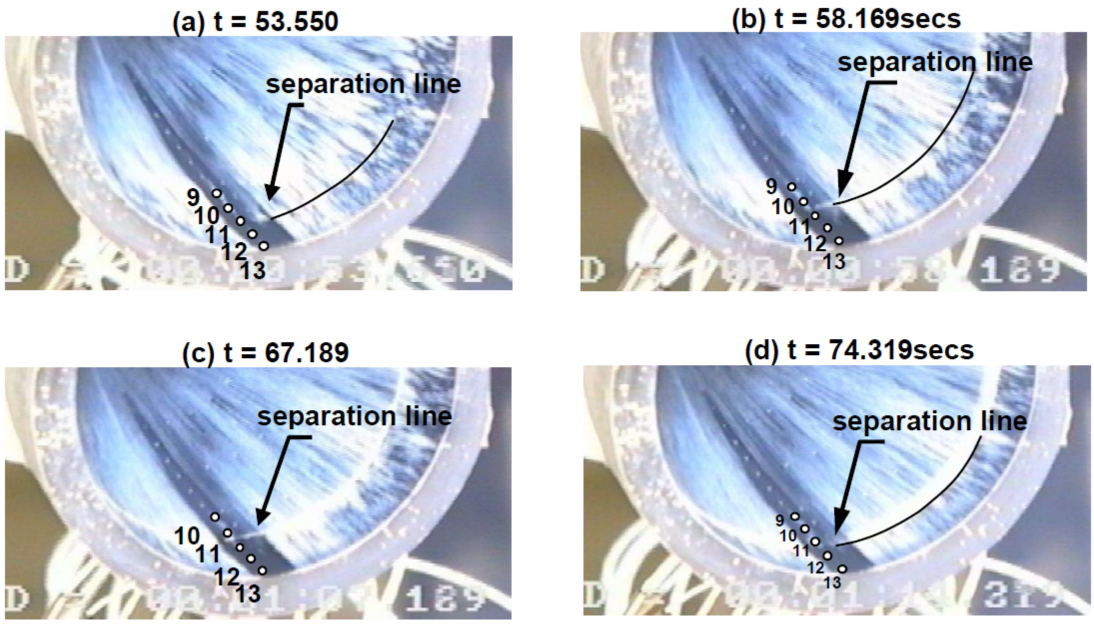

Figure 2.15: Surface oil visualization pictures during the test run showing separation movement [30]

2.6 Frequency analysis

Frequency analysis is an important tool for understanding the dynamic behavior of fluid flows, particularly in systems where unsteady pressure fluctuations play a significant role. By decomposing pressure signals into their spectral components, it is possible to identify dominant frequencies, transient events, and the overall energy distribution within the system. Common techniques used in frequency analysis include Fourier transforms, wavelet transforms, and time-frequency analysis. While Fourier analysis is well-suited for stationary signals, wavelet transforms allow for the investigation of non-stationary phenomena by preserving temporal variations in the spectral content.
In the context of overexpanded rocket nozzles, frequency analysis can help in characterizing the internal shock-boundary layer interactions, separation and reattachment processes, and unsteady loads acting on the nozzle structure. These insights are essential for predicting and mitigating potentially harmful pressure fluctuations that can compromise nozzle performance and structural integrity.
A study conducted by Baars and Tinney (2013) [31], focuses on the analysis of transient wall pressures in an overexpanded, large area ratio nozzle. The research aims to understand the flow and shock structure patterns during both fixed and transient nozzle operations by utilizing spatial Fourier transformations and time-frequency analysis. To investigate the unsteady nature of wall pressure, the authors performed a Fourier-azimuthal decomposition. This technique allowed for the extraction of azimuthal mode coefficients, reducing the complexity of single-point measurements and providing insight into the global behavior of the flow. The results indicated that for both fixed and transient operations, the axisymmetric breathing mode ($m = 0$) contained the majority of the resolved energy. This mode was found to be dominant across all test conditions, demonstrating the primarily axisymmetric nature of the pressure fluctuations. A time-frequency analysis was conducted using the Morlet wavelet transform to better characterize the spectral behavior of the wall pressure signatures over time. This approach was particularly useful in identifying transient events and localized spectral phenomena that would otherwise be obscured in traditional Fourier-based analysis.
The three major low-frequency events ($f < 400$ Hz) were identified during the start-up phase of the nozzle:

- FSS to RSS Transition: The transition from free shock separation (FSS) to restricted shock separation (RSS) resulted in a sharp increase in unsteady pressure fluctuations, particularly near the incipient separation shock.

- Passage of the Reattachment Line: As the flow evolved, the reattachment line of the first separation bubble moved downstream, causing significant spectral activity around 100 Hz.

- End-Effects Regime: Once the first separation bubble opened intermittently to ambient pressure at the nozzle lip, a highly unsteady phase characterized by intense fluctuations around 150 Hz was observed.

The study also analyzed how variations in the transient ramp rate affected wall pressure unsteadiness. It was found that even small deviations in ramp rate significantly influenced the energy levels experienced by the nozzle wall. Higher ramp rates led to increased wall pressure intensity, particularly near the reattachment points of separated bubbles. The results suggest that the ramp rate plays a critical role in determining the extent of unsteadiness and potential structural loading on the nozzle.

A comparison of spectral properties between transient and fixed NPR (Nozzle Pressure Ratio) conditions revealed that while the general spectral characteristics remained similar, transient operations exhibited enhanced energy levels at key transition points. This suggests that steady-state analyses may not fully capture the dynamic complexity of real-world nozzle operations, particularly during start-up phases.

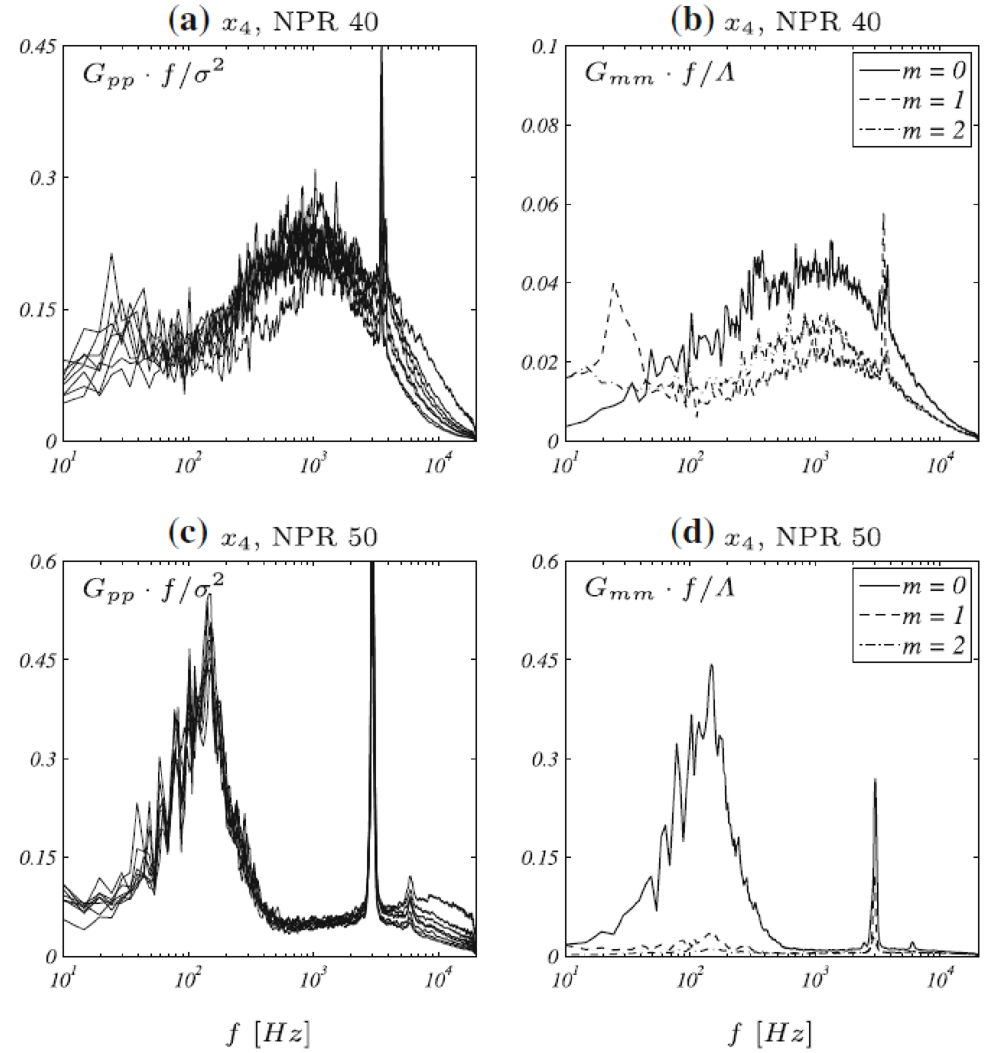

Figure 2.16: (a), (c): Power spectral densities from dynamic pressure transducers at NPR=40 (RSS) and NPR=50 (end effects). (b), (d) Frequency-dependent eigenspectra of the first three Fourier azimuthal modes

Chapter 3

Nozzle Design

This chapter outlines the iterative process that led to the final design of the test nozzle, guided by the design requirements. It details the contour selection procedure and nozzle sizing and validates the nozzle flow behavior using Computational Fluid Dynamics methods. Final nozzle parameters and preliminary side load calculations are also presented.

3.1 Design requirements

The specific design requirements for the test nozzle were established to ensure effective testing outcomes while observing the constraints and limitations of the nozzle rig and testing facility. These requirements are listed below:

Identifier	**Requirement**
NOZ-01	The nozzles shall be cheap and fast to produce
NOZ-02	The nozzle shall be rigid (stiff), not flexible
NOZ-03	The nozzle wall shall host 3 arrays of 16 pressure sensors
NOZ-04	The nozzle shall demonstrate the End Effect Regime at NPR < 32
NOZ-05	The internal wall of the nozzle shall be as smooth as possible
NOZ-06	The nozzle shall be easily attachable and removable from the nozzle rig

Table 3.1: Nozzle design requirements

3.2 Contour selection

For the selection of the nozzle contour in these experiments, the same thrust-optimized parabolic (TOP) contour used by De Kievit [26] in previous studies at the TU Delft nozzle facility was chosen as the starting point. De Kievit's work provided a validated baseline for further modifications, ensuring continuity with existing research and enabling meaningful comparative analysis. The selected design, known as the PAR3 contour, was originally developed by Ruf et al. [32] for test campaigns at NASA Marshall Space Flight Center. This contour was chosen due to its thrust-optimized characteristics and distinct expansion angle. In fact, unlike conventional TOP nozzles, the PAR3 contour features a higher expansion angle of 40°, which ensures that the transition from Free Shock Separation (FSS) to Restricted Shock Separation (RSS) occurs within a practical nozzle pressure ratio (NPR) range.

For the present research, the PAR3 contour was adopted as a reference but was truncated in order to better align with the experimental objectives. This modification was aimed at investigating how reducing the nozzle length influences flow separation and transition behavior. Specifically, given previous findings suggesting that shortening the nozzle could lower the NPR at which the End-Effect Regime occurs, this alteration was implemented to examine its behavior and the related separation dynamics, while also fulfilling the defined nozzle design requirements. For completeness, Table 3.2 provides an overview of the nozzle parameters used in previous experiments, along with their respective references.

No.	r^* [mm]	ϵ	Scale	q_{RSS}	FSS $\rightarrow$ RSS	EER	Unsteadiness Frequency [Hz]	Source
1	19.05	30.5	1:6.8	13	23.1-23.6	48	150-1500	[33, 32]
2	19.05	38	1:6.8	-	24.3	-	150-1500	[34]
3	10	30	1:13.1	9	31	36	-	[15, 35, 36]
4	33.54	20	1:3.9	-	15	28	100	[37, 38]
5	13.6	30.32	1:9.6	7	24	45	50-100	[39]
6	6.35	30.29	1:20.5	-	22	37-39	100-3000	[40, 41]
7	10	15.21	-	-	13.5	30	-	[42]
8	10.2	7.36	-	-	-	20	-	[43]

Table 3.2: Parameters of nozzles used in previous transient investigations.

The original and truncated nozzle contours are showed in Figure 3.1 for a direct dimension comparison. The first iteration on the truncation was guided by pressure data from De Kievit's experiments on the FSS-to-RSS transition [26], specifically targeting the location of the last observed pressure peak as the cutoff point. Detailed nozzle contour coordinates are provided in the appendix.

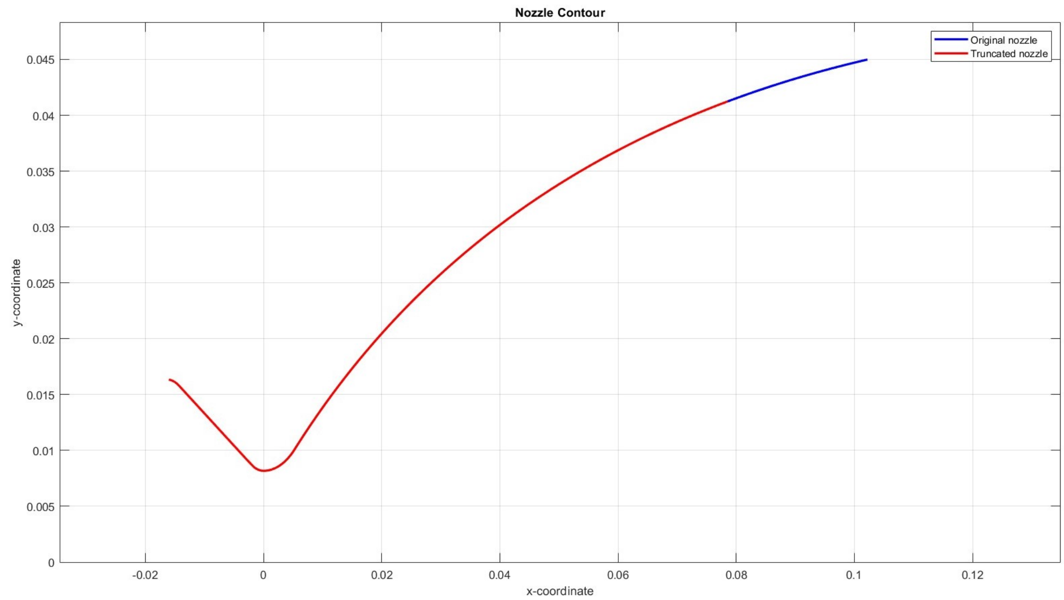

Figure 3.1: Truncated TOP nozzle contour

3.2.1 CFD design validation

A Computational Fluid Dynamics analysis was conducted using Ansys Fluent 2023 R1 version to validate the nozzle design and, above all, to investigate the effective presence of the End Effect Regime in the wanted NPR range, according to the wind tunnel limitations. The primary goal was to identify the location where EER phenomena occur, that is when the reattachment line reaches the nozzle lip, resulting in the recirculation bubble randomly opening to the ambient atmosphere, causing a local pressure peak close to the nozzle exit section.
The CFD analysis was simplified using a plane 2D nozzle geometry, carefully modeled and meshed with a very fine grid. The mesh was especially refined, using the Edge Sizing function with a suitable Bias Factor, along the nozzle wall, at the throat, and at the exit of the nozzle to ensure accurate resolution of boundary layers, separation points, and recirculation zones.

A 2D axisymmetric model was chosen for this analysis to further simplify the computational domain, using the nozzle axis as the symmetry line. The computational domain extends beyond the nozzle to provide sufficient space for the flow to fully develop, enabling a detailed investigation of the plume behavior, which is later compared with schlieren analyses. A steady-state simulation was conducted using the Reynolds-Averaged Navier-Stokes (RANS) equations, an approach selected for its ability to efficiently capture essential flow dynamics while maintaining computational efficiency. The SST k-omega turbulence model was

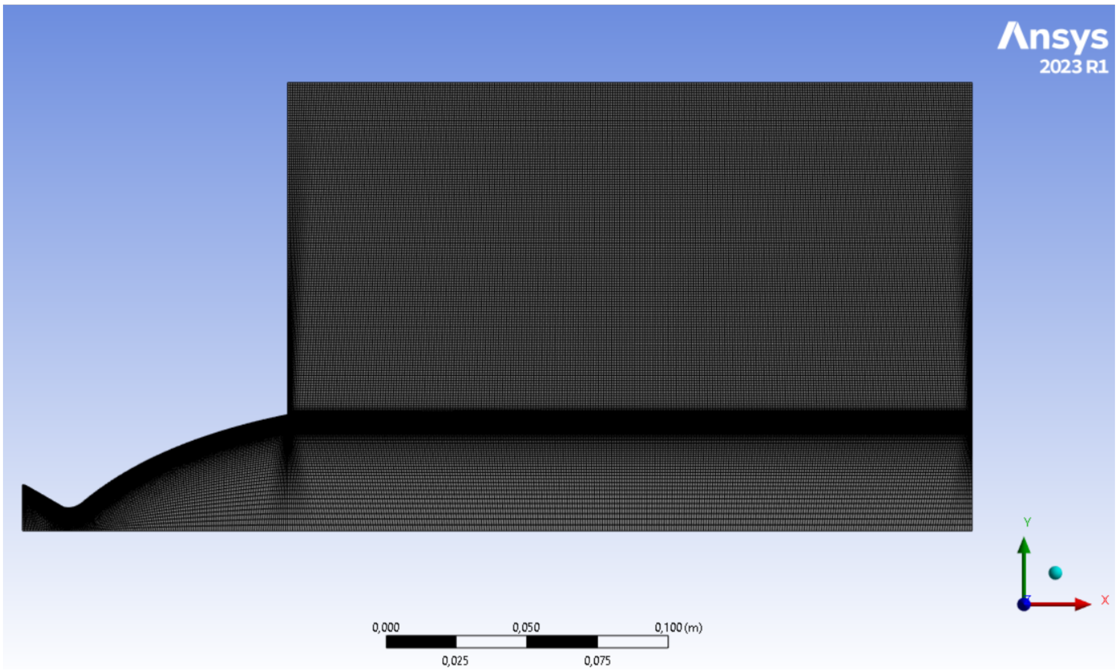

Figure 3.2: Mesh

employed to accurately capture complex flow behaviors, including recirculation and separation [44], which are crucial for visualizing separation effects. However, smaller flow structures and pressure fluctuations are not resolved in this type of analysis. Dry air was used to replicate the wind tunnel conditions.
Different versions of the truncated nozzle, each with varying lengths (x-axis), were tested at different NPR values. The analysis described above was repeated iteratively multiple times until the expected physical phenomena occurred. The NPR range considered for this analysis was from 19 to 23 for the FSS/RSS transition and from 24 to 30 for capturing the End Effect. The numerical results identified, in a final version of the nozzle, NPR = 21 as the threshold for the Free Shock to Restricted Shock transition, where the flow begins to attach to the wall and interact with the boundary layer, as shown in Figure 3.3. Similarly, the End Effect was observed at NPR = 25, as depicted in Figure 3.4.

This preliminary analysis confirmed that the nozzle design would have been capable of capturing the End Effect Regime at a nozzle pressure ratio consistent with the maximum pressure limits of the wind tunnel. As expected, as the nozzle pressure ratio increases, the shock structure from the TOP nozzle remains intact and shifts downstream.
On the other hand, it is important to emphasize that in reality, unsteady transition phenomena are inherently asymmetrical, with significant three-dimensional effects.

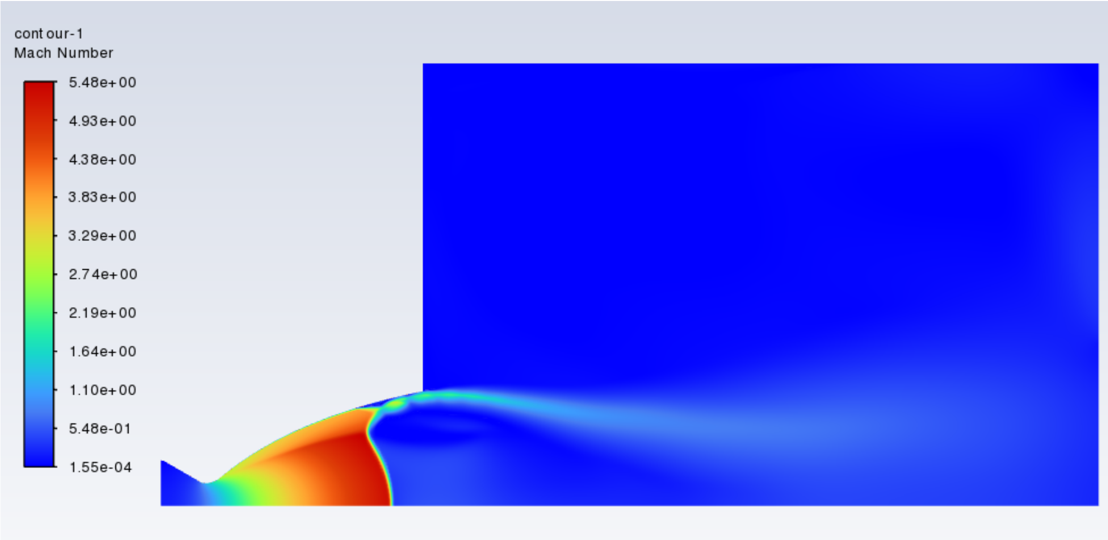

Figure 3.3: Mach contour (NPR=21)

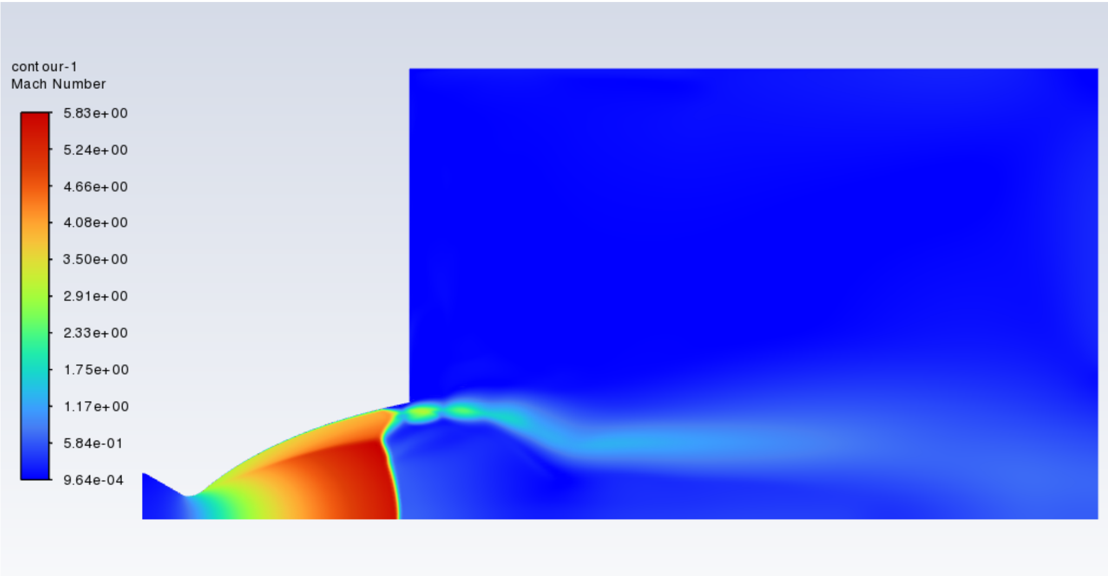

Figure 3.4: Mach contour (NPR=25)

Additionally, the simulation may predict these phenomena slightly downstream, resulting in a shifted Mach disk position.
Further discussion on the numerical results, in comparison to the experiments, will be presented in the Results chapter.

3.3 Nozzle parameters

The characteristic parameters of this validated nozzle are calculated and presented, based on the specified expansion ratio, chamber and atmospheric pressure, and mass flow rate. The mass flow rate, determined a priori using the choked flow equation, represents the maximum achievable flow rate through the nozzle.

Given:

- $P_c = 4{,}000{,}000\,\mathrm{Pa}$ (40 bar),
- $P_a = 101{,}325\,\mathrm{Pa}$,
- $T_c = 288\,\mathrm{K}$
- $A_e = \pi R_e^2 = 0.005{,}311\,\mathrm{m}^2$,
- $\varepsilon = 25.33$,
- $\gamma = 1.4$,
- $c_p = 1{,}005\,\mathrm{J\,kg^{-1}\,K^{-1}}$,,
- $R = 287\,\mathrm{J\,kg^{-1}\,K^{-1}}$,
- $\dot{m} = 2\,\mathrm{kg\,s^{-1}}$

Exit pressure is calculated using the isentropic relation:

$$P_e = P_c \cdot \left(\frac{1}{\varepsilon}\right)^{\frac{\gamma}{\gamma-1}} \tag{3.1}$$

Exit velocity is calculated using:

$$v_e = \sqrt{\frac{2\gamma R T_c}{\gamma - 1}\left(1 - \left(\frac{P_e}{P_c}\right)^{\frac{\gamma-1}{\gamma}}\right)} \tag{3.2}$$

Thrust is calculated as:

$$F = \dot{m} v_e + (P_e - P_a) A_e \tag{3.3}$$

Thermodynamic efficiency is given by:

$$\eta_t = \frac{\frac{1}{2}\dot{m} v_e^2}{\dot{m} c_p T_c} = \frac{\frac{1}{2} v_e^2}{c_p T_c} \tag{3.4}$$

Finally, the Reynolds number is calculated using values from Computational Fluid Dynamics and reported in Table 3.4, along with other computed nozzle parameters, serving as a reference for nozzle performance.

Property	**Value**	**Unit**
Throat radius (R_t)	8.175	mm
Exit radius (R_e)	41.135	mm
Expansion ratio ($\varepsilon = A_e/A_t$)	25.33	-
Chamber pressure (P_c)	40	bar
Atmospheric pressure (P_a)	101.325	kPa
Chamber temperature (T_c)	288	K
Mass flow rate ($\dot{m}$)	2	$\mathrm{kg\,s^{-1}}$

Table 3.3: Measured nozzle data

Property	**Value**	**Unit**
Exit pressure (P_e)	30.36	kPa
Exit velocity (v_e)	718.95	$\mathrm{m\,s^{-1}}$
Thrust (F)	712.7	N
Thermodynamic efficiency (η_t)	92.67	%
Exit Reynolds number (Re)	$3.61 \cdot 10^{-6}$	-

Table 3.4: Calculated nozzle performance values

3.3.1 Effects of nozzle truncation

Some key considerations regarding the effects of nozzle truncation, beyond the intended reduction of the NPR at which transition phenomena occur (primary goal of the new design), are analyzed by comparing the performance of nozzles with two different expansion ratios: $\varepsilon = 25.33$ (used in the current research) and $\varepsilon = 30.29$ (studied in previous research at the same facility [26, 45]). Calculations are performed under identical input conditions, including chamber pressure, atmospheric pressure, temperature, and mass flow rate. The results demonstrate that a higher expansion ratio ($\varepsilon = 30.29$) yields notable performance enhancements, as predicted by theoretical expectations. Specifically, the exit pressure (P_e) decreases from 30.36 kPa to 26.15 kPa, leading to improved adaptation to atmospheric conditions and reduced over-expansion. As a result, thrust (F) increases from 712.7 N to 731.6 N, corresponding to a gain of 18.9 N. Additionally, the thermodynamic efficiency (η_t) improves from 92.67 % to 96.65 %, highlighting a more effective conversion of chamber energy into kinetic energy. This outcome was expected, as the current nozzle design is a modified version of a contour originally optimized for thrust but modified for research purposes.

3.4 Side loads calculations

Some final theoretical calculations on side loads, for the sake of completeness, are here performed, since the side loads will not be directly object of laboratory measurements in the wind tunnel. Those calculations are based on the wall pressure data taken from the CFD analysis showed above.
Under pure free shock conditions, a simplified model is derived by assuming a tilted flow separation. This assumption is foundational to several side load models, such as those developed by Pratt and Whitney, Rocketdyne, Aerojet, and Schmucker [46, 47] . When the wall pressure distribution is asymmetric, the integrated force acting over the nozzle wall results in a nonzero side force.

The general equation for the side load F_{sl} is given by:

$$F_{sl} = \int_0^L \int_0^{2\pi} (p_a - p_w) \cos(\tau) \, dA \tag{3.5}$$

where dA represents a nozzle surface element, τ is the local contour angle of the nozzle, and p_a and p_w are the atmospheric and wall pressures, respectively. The integration is performed over the entire length of the nozzle L, and over the angular dimension of the nozzle surface, from 0 to 2π.

This equation can be simplified as:

$$F_{sl} \approx (p_a - p_i) \, A_{sl} \tag{3.6}$$

where A_{sl} is the nozzle surface area affected by asymmetric flow. In this equation, p_i represents the pressure at the location of the flow separation. As A_{sl}, the effective area over which the pressure difference acts, is obtained in the Schmucker model by considering the variation of the position of separation caused by pressure fluctuations. These fluctuations are assumed to be proportional to the nominal wall pressure p_w. This assumption is empirically valid in the attached flow region. The model depends on several empirical constants, which must be determined for each new nozzle.

This model, based on the assumption of tilted flow separation, provides an estimate of the side load by calculating the pressure difference acting over the nozzle surface, integrated over the appropriate region where asymmetric flow influences the nozzle wall. However, it does not account for the influence of the incoming boundary layer or the characteristics of the downstream flow. More importantly, this approach is quasi-static and does not model the time dependence of the pressure forces.

The side load calculations are implemented in MATLAB using wall pressure data from the CFD simulations. The calculations are performed using the two approaches: the original formula, which involves integrating the pressure distribution over the nozzle surface, and an approximated model for a quicker estimation.

Initially, the geometry data of the nozzle and the pressure data from the CFD analysis are loaded. Geometric conversions are made, and the CFD pressure data is interpolated along the axial positions of the nozzle. For the original formula, the side load force is computed by numerically integrating the pressure difference between the wall pressure and atmospheric pressure over the nozzle surface. This integration considers both the radial angle of the nozzle and the axial distance. On the other hand, the approximated formula simplifies the calculation by assuming a constant pressure difference over the effective area of the nozzle surface where asymmetric flow occurs. This provides a less precise result. The results from both methods — original and approximated — are compared in Table 3.5.

NPR	F_{sl} **(Original Formula) [N]**	F_{sl} **(Approximated) [N]**
21 (FSS to RSS)	72.48	80.82
25 (EER)	25.64	29.42

Table 3.5: Side Load Force Calculated for the Two CFD Cases: Original and Approximated Methods

It can be concluded that the maximum side loads occur under Restricted Shock separation conditions, with a value approximately 10% of the nozzle's theoretical thrust, a result consistent with previous literature [48].

Chapter 4

Experimental methodology

This chapter provides an overview of the experimental setup and methodology, beginning with the manufacturing of the previously analyzed nozzle, followed by the implementation of pressure sensors within it, and its integration into the testing system. It will also include a discussion on the circuit control interfaces and the practical application of the different visualization techniques.

4.1 Nozzle manufacturing

The test nozzle was manufactured using 3D printing with PLA, basing on the validated contour and the nozzle rig matching requirements. Since it was not meant to be compliant for this research, high infill percentage was used during the printing process, and the walls were intentionally made thicker to enhance the nozzle's rigidity, minimizing movement and reducing its susceptibility to vibrations, or rupture due to cracks. 3D printing was not only the fastest manufacturing option, but it also allowed for the quick production of a different contour prototype if this one proved unsuitable for the EER caption, due to a possible mismatch between numerical and experimental tests.

In the post-printing process, the internal surface of the nozzle was carefully sanded to reduce surface roughness, which is definitely more likely in a printed nozzle than in an aluminum-manufactured one. In addition, 0.3mm holes were drilled in order to enable the connection between the blind holes for pressure sensors array and the internal part of the nozzle, subject to the air flow. Those holes need to be as small as possible in order to not influence the internal flow behavior, allowing a correct data reading.

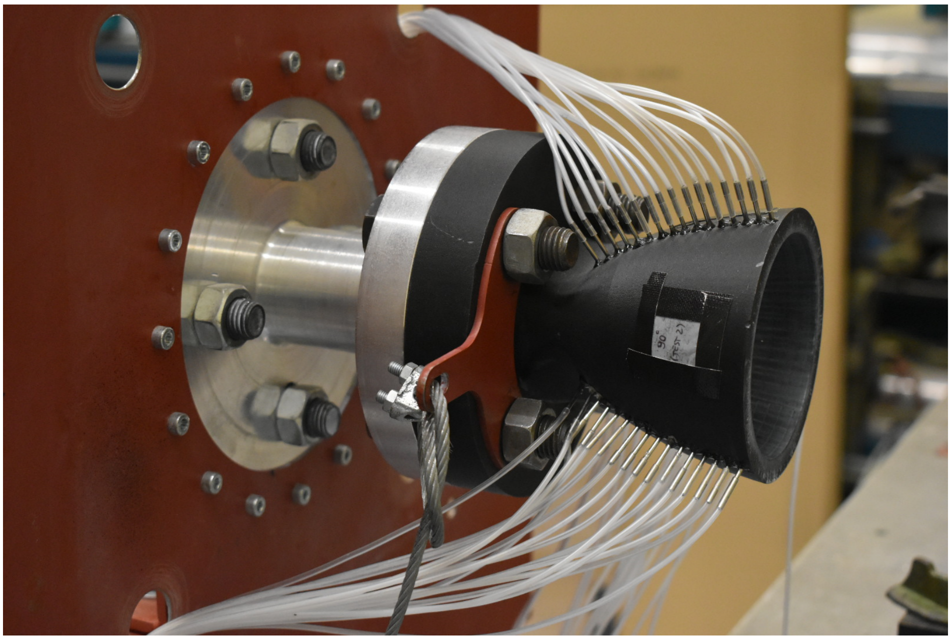

Figure 4.1: 3D printed nozzle connected to ASCENT rig

4.2 Test setup

The current research test setup is now described in detail. First, an overview of the test facility and its operational principles is provided. Next, the data acquisition scheme and its settings are outlined, followed by a detailed description of the pressure sensors and software interfaces. Finally, the configurations of Schlieren, focusing Schlieren, and oil film techniques are presented.

4.2.1 ASCENT nozzle test facility

The experimental activities presented in this thesis have been conducted using the ASCENT test rig, horizontal test bench located in the ST-15 supersonic wind tunnel of the Delft University of Technology High Speed Laboratories [49].
The components of the test setup are indicated in Fig. 4.2. The rig diffuser is designed to be connected through a flexible hose to the upstream circuit, where the NPR is controlled using a hand operated control valve and a main valve is pneumatically actuated to allow the pressurization the circuit. The nozzle rig is supported by four structural legs, which are clamped securely to the terrain to maintain its position and withstand the loads generated by the nozzle. The ST-15 diffuser is employed in order to let the air exit from the laboratory and from the building.

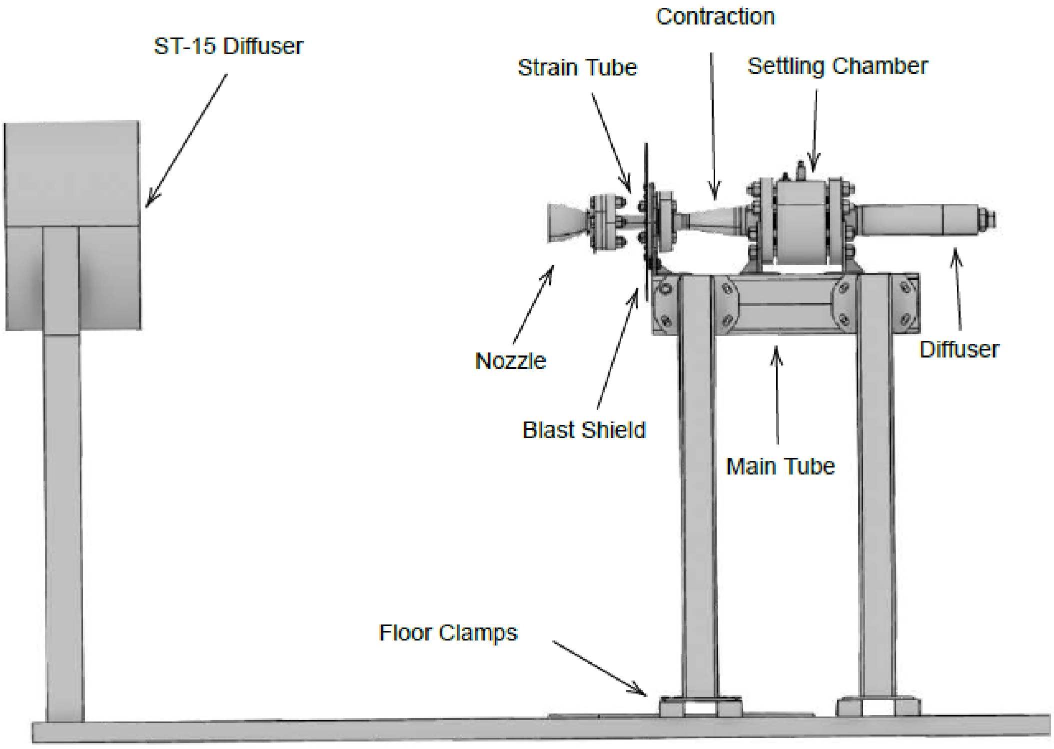

Figure 4.2: ASCENT rig [26]

The working fluid employed is dry, unheated air ($T_0 = 288K$) supplied from an external pressure vessel with a capacity of 300 m^3. When fully charged, the reservoir contains approximately 484 kg of air, allowing for a maximum stagnation pressure of 40 bar. Due to the large volume of the vessel, the system can operate for around 18 minutes before recharging is required. According to De Kievit [26], using a nozzle with a throat radius of 1 cm would result in a pressure drop of about 0.5 bar during a 60-second run. For shorter test durations, on the order of tens of seconds, the pressure remains effectively constant, eliminating the need for active flow control. However, pressure losses in the feed system between the tank and nozzle amount to approximately 8 bar, limiting the maximum achievable nozzle pressure ratio to around 32. This constraint necessitated designing the test (and, as a consequence, the nozzle) to keep the NPR below this value, considering a margin, to enable visualization of the EER.
Finally, the setup is supported by an electronic box with power supply, terminal blocks and a relay switch. An emergency button is installed in the main valve circuit to allow immediate manual shutdown of the valve in case the connection to the relay module is lost or in an emergency situation.

A detailed schematic of the setup hardware connections is shown in Figure 4.3.

Parameter	**Value/Type**	**Unit**
	Pressure	
Sensor	IFM PT5402	-
Acquisition frequency	2000	Hz
	Schlieren imaging	
Parabolic mirror focal length	1500	mm
Camera type	Photron FASTCAM SA1.1 - Photron FASTCAM Nova S12	-
# of cameras	1	-
Exposure time	1/40000 - 1/150000	s
Image resolution	1024 x 1024 - 384 x 240	pixels
Acquisition frequency	20000 - 100000	Hz
	Run duration	
Test run duration	10	s

Table 4.1: Experimental setup parameters.

4.2.2 Pressure ports

Three Scanivalve DSA3217-PTP absolute pressure scanners [50] were available in the facility for wall pressure measurements on the nozzle. The pressure ports are strategically positioned in three rows, azimuthally distributed and spaced 120 degrees apart. This arrangement is designed to capture asymmetries in the separation location across different quadrants of the nozzle. A total of 16 pressure ports, evenly spaced (4.5mm distance) between the separation point around a NPR of 15 and the nozzle lip, are located along the nozzle contour as presented in Fig. 4.1. The location of the first pressure port had to be selected such that the measurement range of the ScaniValves was never exceeded. The minimum range of the ScaniValves is 15 psi, or 1.04 bar, gauge pressure, so a maximum absolute pressure of approximately 2 bar can be measured. Among the three, one pressure module had a range of 15 psi, while the other two had ranges of 30 psi and 50 psi. Moreover, to study and investigate potential asymmetry phenomena, pressure recordings were conducted with the nozzle oriented in three different positions. Specifically, the initial configuration, referred to as the 0° test, served as the baseline. From this position, the nozzle was subsequently rotated in anticlockwise direction to 90° and 180°, respectively (Figure 4.4). This approach aimed to analyze flow asymmetries as well as the possible influence of the varying ranges of the three pressure modules and/or intrinsic asymmetries in the internal surface of the nozzle.

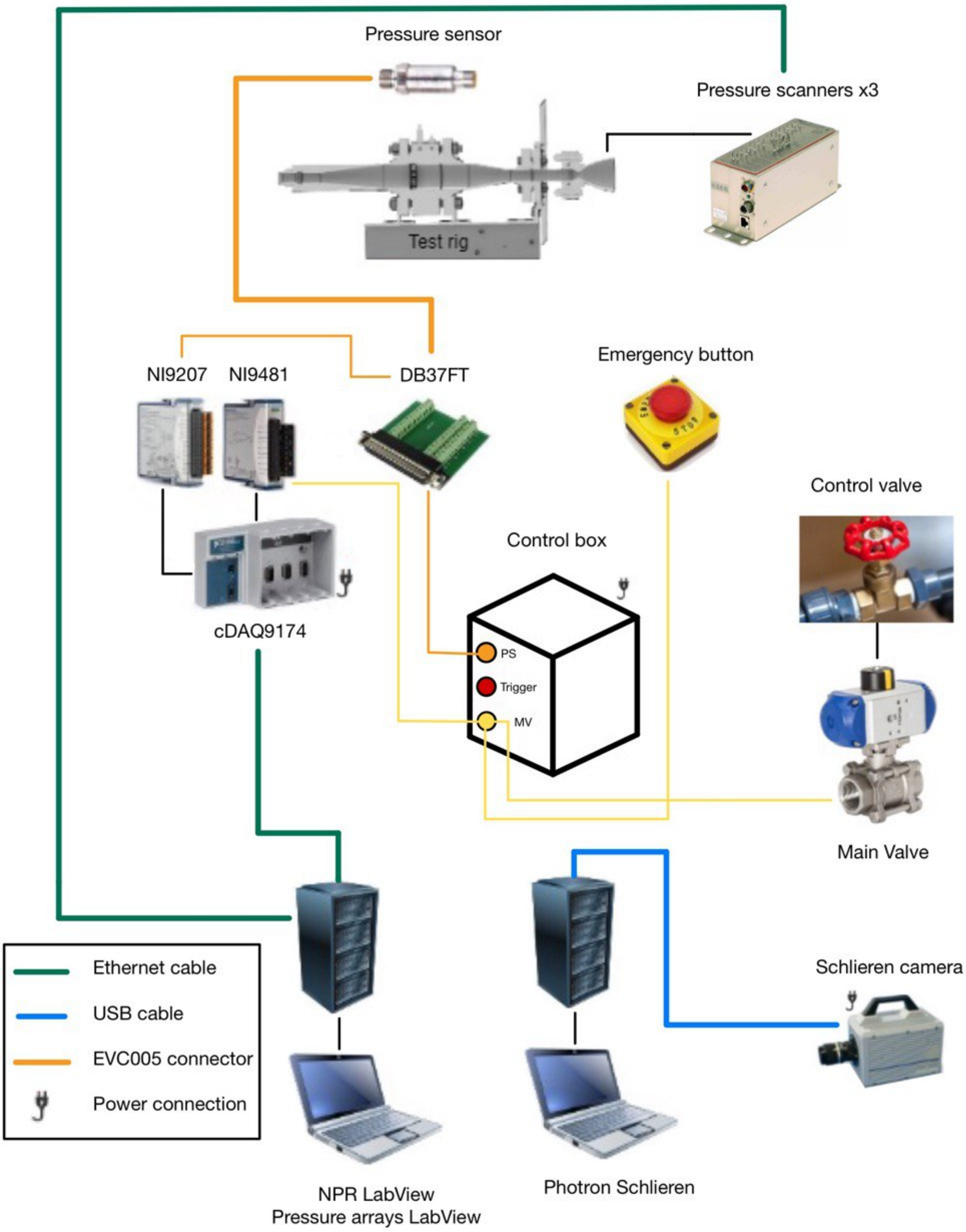

Figure 4.3: Cold flow testing acquisition system flow chart

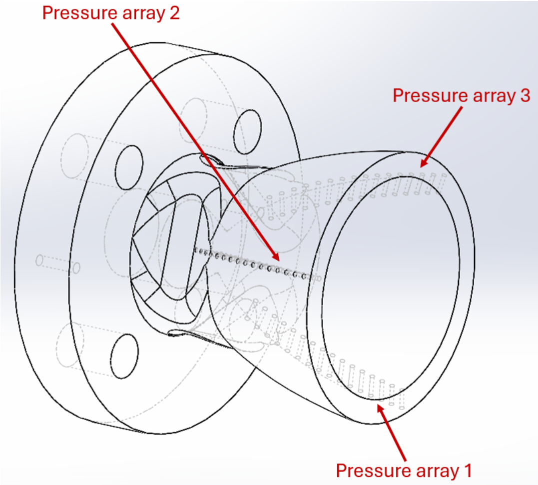

(a) 0° test configuration

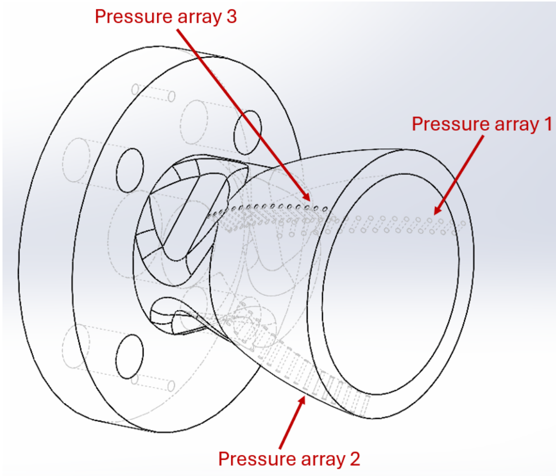

(b) 90° test configuration

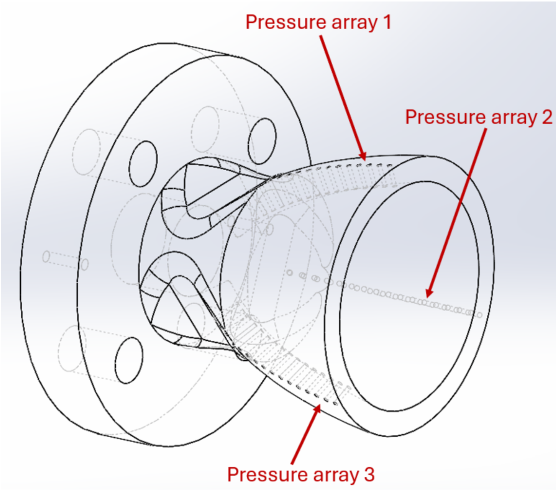

(c) 180° test configuration

Figure 4.4: Nozzle rotation: pressure sensors configurations

4.2.3 LabView interfaces

A specific NI LabView program, previously developed for similar tests, was used to control the test setup. This program allows real-time visualization of the Nozzle Pressure Ratio (NPR) by dividing the total pressure measured by the pressure sensor (via a NI DAQ module) by the input atmospheric pressure in mbar, set as a value of 1012.53. Among the inputs, the option to include the file name where the test data is stored is also available. The most important feature of the program is its control over the main valve actuation in the circuit, achieved through a connected channel in the relay module. The valve opens or closes based on a button press,

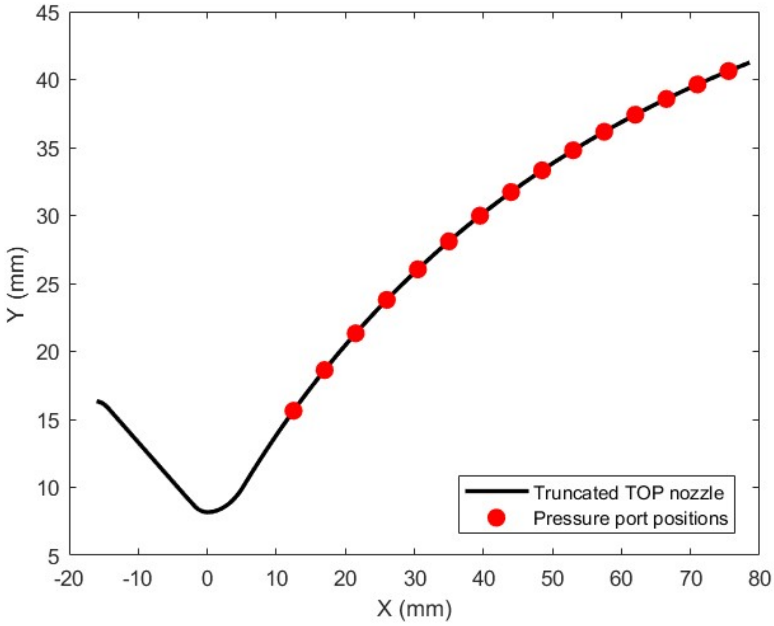

Figure 4.5: Pressure sensors distribution along nozzle contour

where it opens when pressed. At the start of the program, the main valve is always reinitialized to the closed position to prevent accidental opening upon launching the program. Additionally, the program includes an "Update Speed" command, which adjusts the rate at which the NPR value is updated. In the tests presented in this thesis, the temperature sensor channel and triggers were not utilized. When the "Start Measurement" button is clicked, the data acquisition process begins, and the system records measurements for the specified duration of “measurement time” in milliseconds, at the defined “sampling rate.” The elapsed time is displayed below the button. The "Stop Test" command halts all active loops and can be used to stop measurements at any time. This command should be used at the conclusion of the test or in case of an emergency. When activated, it will automatically close the main valve (if open) and terminate data acquisition.

In parallel with the previous program, a separate LabView application is used to read data from the Scanivalve pressure transducers positioned along the nozzle's divergent section to measure wall pressure. In this case as well, an existing program was adapted to handle output readings from three different modules simultaneously, each equipped with an array of 16 pressure ports. To streamline data collection, an Ethernet switch was employed, consolidating the inputs into a single Ethernet port on the computer. Among the settings, a reading rate of 1000 frames per second was chosen to ensure the data was updated as frequently as possible.

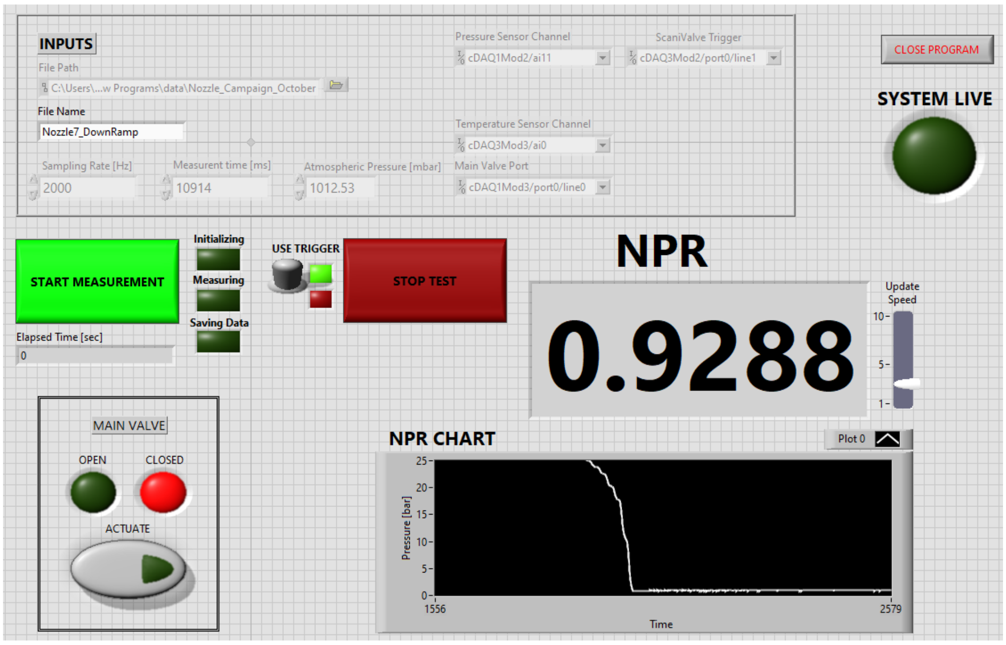

Figure 4.6: MV and NPR control interface

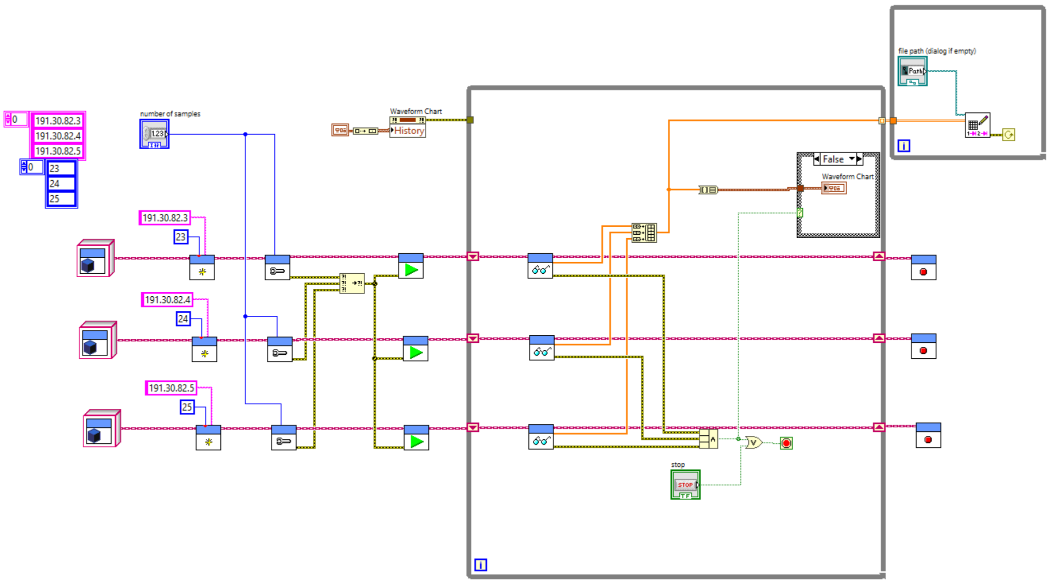

Figure 4.7: Pressure transducers reading scheme

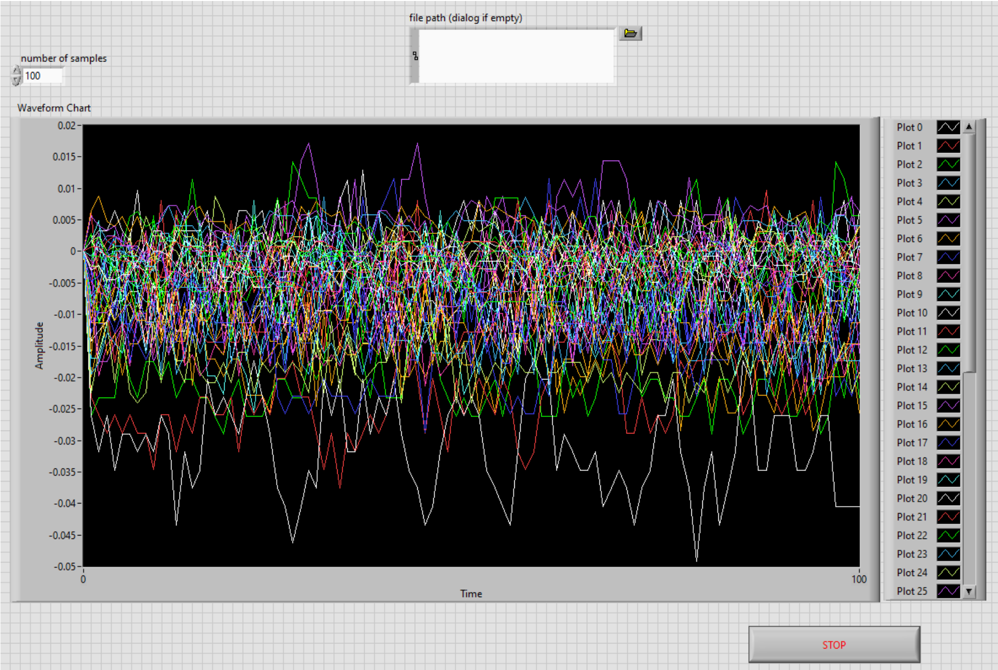

Figure 4.8: Pressure transducers interface

4.3 Visualization techniques

4.3.1 Camera settings

A high-speed camera sensor was required for test applications of Schlieren, Focusing Schlieren, and Shadowgraphy visualizations. As indicated in Table 4.1, two different cameras were employed: the Photron FASTCAM SA1.1 [51] and the Photron FASTCAM Nova S12 [52]. The tests initially used the FASTCAM SA1.1, which performed adequately at frame rates up to 20,000 fps before image resolution began to degrade. Since higher recording rates were necessary for the intended frequency analysis, the ultra-high-speed FASTCAM Nova S12 was subsequently introduced, allowing data collection at 100,000 fps while maintaining satisfactory resolution. Notably, the Nova S12 can reach frame rates as high as 1,100,000 fps at lower resolutions. Additionally, the exposure settings were carefully regulated to ensure that the initial images were sufficiently bright for clear visualization without risk of overexposure. This approach allowed the raw footage to maintain adequate contrast while leaving room for post-processing adjustments—such as enhancing the image brightness—to further improve clarity and detail.

4.3.2 Schlieren

The Schlieren technique was the main flow visualization tool for the current study. Schlieren imaging effectively illustrates the flow state, enabling easy identification of the separation effects in the exhaust plume of the nozzle.
The Schlieren setup used in the experiment is arranged in a Z-configuration due to space limitations, as illustrated in Figure 4.9. A continuous LED light source is directed through a lens that focuses the light into a pinhole. This pinhole ensures that the light behaves like it's coming from a near-point source, resulting in parallel light rays entering the flow. Some opaque tape was put on the pinhole to have a better diffusion of light. The pinhole is positioned at the focal point of a 1500 mm parabolic mirror. These parallel rays then pass through the nozzle test section flow, and after this, an identical parabolic mirror is placed to focus the light. The Schlieren knife edge is positioned at the focal point of this mirror, where the beam converges. It was necessary to block a significant portion of the light, through a schlieren knife, to prevent the images from becoming overexposed. The knife edge was placed in vertical position in order to visualize the vertical density variations, putting it in horizontal did not give significant information for those specific tests. If the Schlieren knife-edge is removed, the setup transitions into a shadowgraph system, without the blocking of refracted light, used for visualization of boundary layers in the nozzle exhaust plume.

4.3.3 Focusing Schlieren

For the focusing schlieren, a proof-of-concept setup was developed and implemented to visualize the shock structures and reduce the contamination caused by three-dimensional effects. However, it must be noted that some issues were encountered during the calibration process, as will be discussed in the Results section. These challenges, which impacted the overall performance of the setup, primarily stemmed from alignment inaccuracies and the limitations of the selected components. Despite these issues, the system was designed to be functional within the constraints of time and budget. A self-aligning focusing schlieren setup was excluded early in the design process due to its prohibitive cost and complexity, favoring instead a more conventional approach.

The setup employed the same high-intensity LED light source used in the conventional schlieren system, operated at its maximum intensity to ensure sufficient illumination. A source grid was integrated with a Fresnel lens, which was chosen to diffuse the light more uniformly across the test section. This step was essential for minimizing variations in light intensity, a common challenge in schlieren setups, and for improving the visibility of density gradients within the flow. The LED light passed through the test section containing the density object, the nozzle, and the

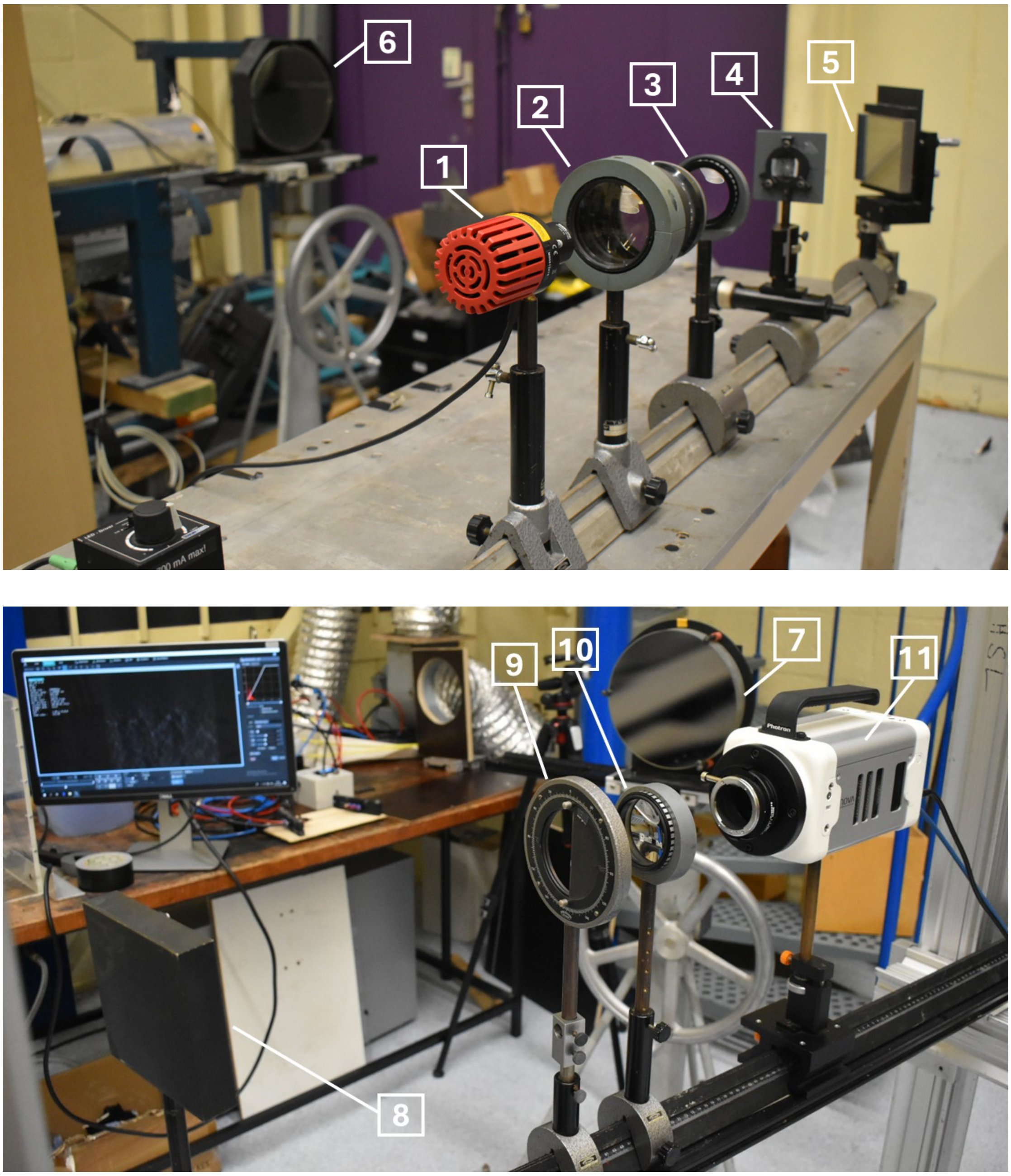

Figure 4.9: Schlieren setup. 1: Light source, 2-3: Lens, 4: Pinhole, 5: Plane reflective mirror, 6: 1500mm parabolic mirror (1), 7: 1500mm parabolic mirror (2), 8: Plane reflective mirror, 9: Vertical knife, 10: 400mm lens, 11: Camera sensor

resulting variations in light intensity were captured by a 250 mm lens positioned at the opposite end of the test section.

The focusing schlieren system's final design aimed to optimize key optical and spatial parameters to enhance its imaging capabilities. The system was designed to achieve a balance between field of view (FOV), depth of focus (Δz), and spatial resolution (Δw). These parameters were adjusted to match the specific requirements of the experimental campaign. The lens-to-source distance (L) and lens-to-focal-plane distance (l) were selected to maximize the sharpness and clarity of the images while ensuring adequate coverage of the flow features under investigation.

Table 4.2 summarizes the final design parameters for the focusing schlieren setup. These values were determined through iterative testing and calculations to ensure that the system could effectively capture the exhaust plume flow field while minimizing optical distortions.

Table 4.2: Design parameters for the focusing schlieren setup.

Parameter	**Symbol**	**Value**
Lens-to-source distance	L	1000 mm
Lens-to-focal-plane distance	l	500 mm
Lens aperture	A	50 mm
Focal length	f	250 mm
Depth of focus	Δz	10 mm
Grid spacing	d	1 mm
Spatial resolution	Δw	0.25 mm

4.3.4 Oil film

For the oil film technique, the setup was relatively simple and quick. The prepared white paint mixture from the laboratory must be thoroughly blended with titanium dioxide to achieve a uniform consistency. This can be done by mixing well with a stick until the texture appears smooth and homogeneous. Once the mixture is ready, a small amount of paint should be applied with a brush. Care should be taken not to overload the brush to ensure an even application. In this case, where a nozzle is being tested, the paint should be applied using random motions. This method ensures that the final streamlines observed at the end of the test are not influenced by the initial brush strokes. The pre-test condition, right after the paint application, and the appearance of the nozzle's internal surface at the end of the test, are shown in 4.11.
For the oil film test recordings, two digital action cameras were used simultaneously, in video mode, to capture the internal flow dynamics. Positioned outside the exhaust plume, on either side of the nozzle, the cameras were strategically placed to provide a comprehensive field of view of the nozzle's internal surface. This

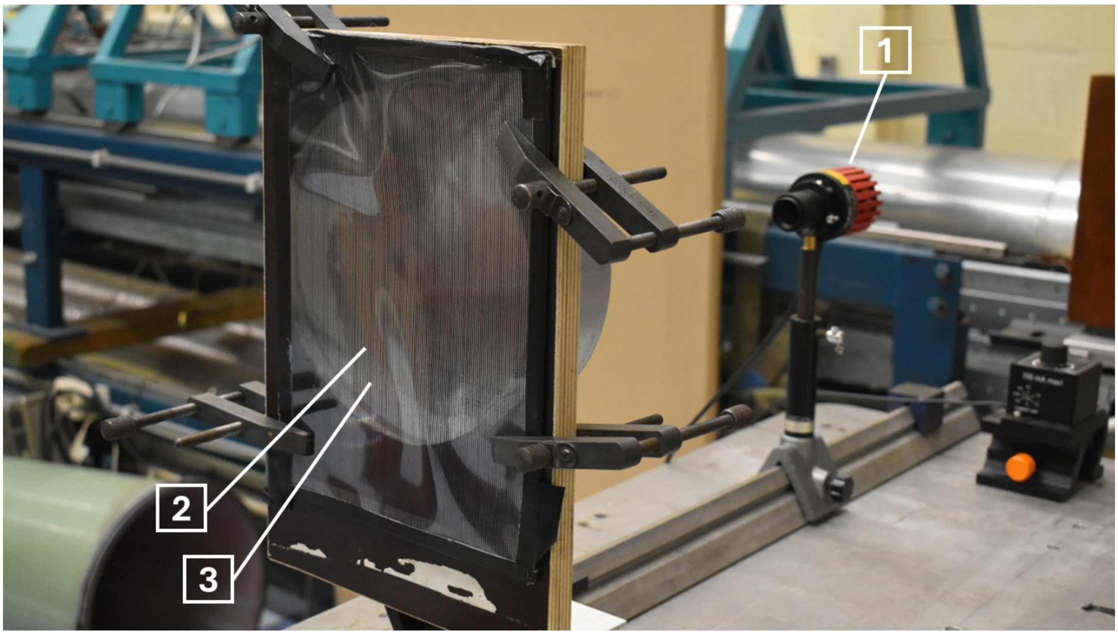

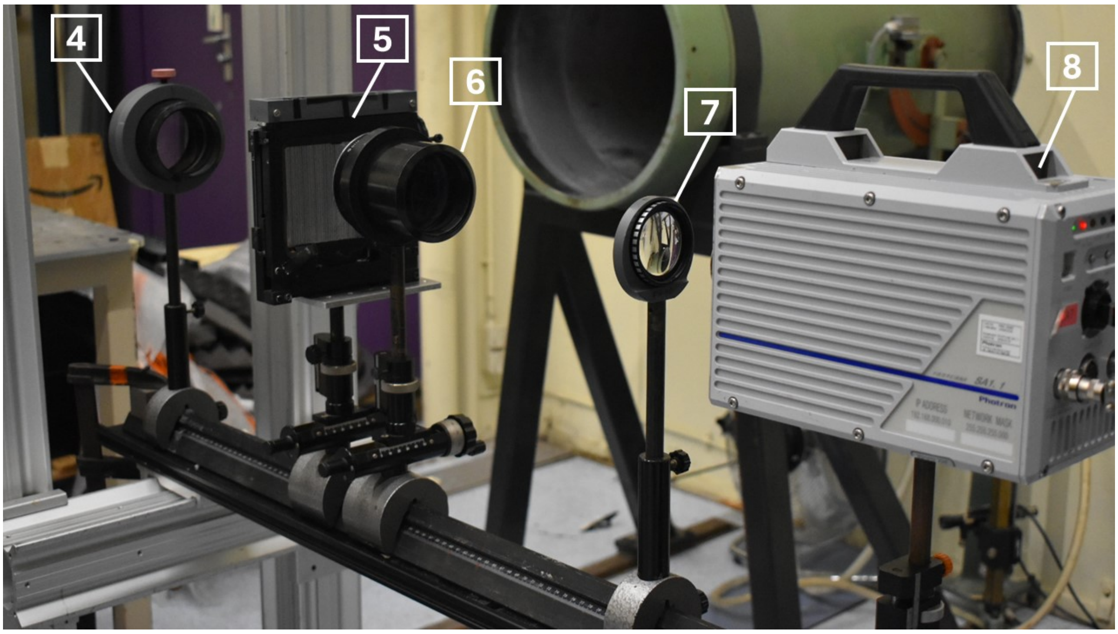

Figure 4.10: Focusing schlieren setup. 1: Light source, 2: Fresnel lens, 3: Source grid, 4: Schlieren lens (f=250mm), 5: Cutoff grid, 6: Relay lens (f=250mm), 7: 150mm lens, 8: Camera sensor

setup allowed for detailed observation of flow asymmetries and enabled a thorough investigation of the flow behavior within the nozzle.

Each test, covering both FSS/RSS transition and EER cases, began by starting the circuit and gradually increasing the NPR to the desired level. Once the target NPR was reached, it was maintained for approximately 10 seconds before the control valve was quickly closed manually. This procedure aimed to capture an oil visualization that accurately reflected the specific unsteady phenomena being investigated.

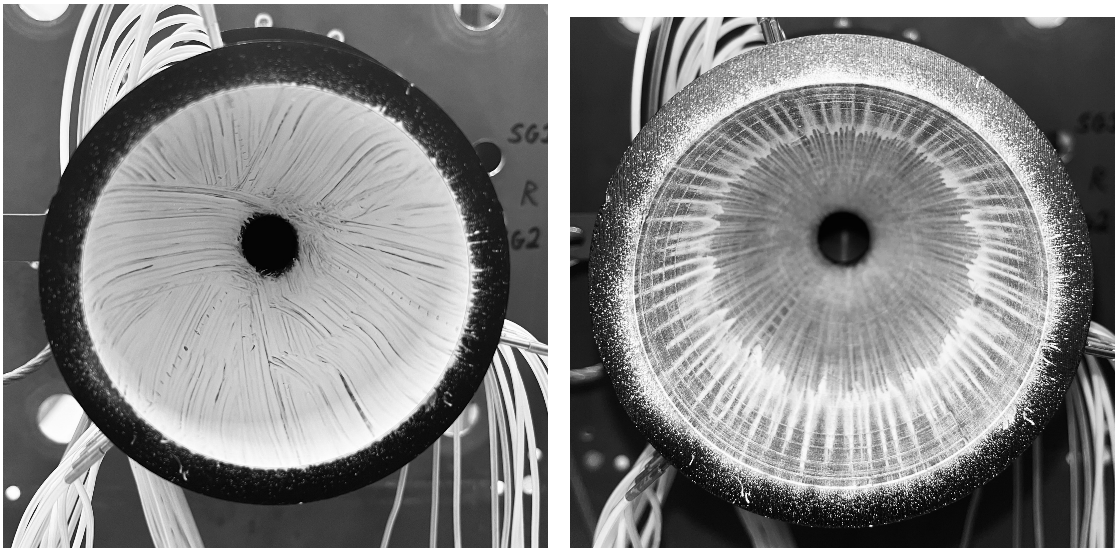

(a) Pre-test condition **(b)** Post-test condition

Figure 4.11: Oil film setup

Chapter 5

Data processing

This chapter aims at briefly presenting and explaining the data processing techniques applied to analyze the different experimental results. It covers the methodology for processing pressure sensor readings, the processing for the visualization of Schlieren images to capture flow structures, and the use of time-resolved imaging for frequency and spectral analysis.

5.1 Pressure sensors measurements

The data processing for this study involved reading experimental datasets containing pressure readings from multiple tests and multiple sensors over several time frames, corresponding to increasing NPR, manually varied by the system control valve. Each dataset was divided into three modules, with each module corresponding to 16 sensors. The data for each module was extracted column-wise from the appropriate time frame, identified by locating the time frame with the maximum pressure within a specific range. Once the data was extracted, corrections were applied to account for anomalies. Specifically, for Module 3, the data from sensor 7 required filtering due to known systematic issues caused by a faulty sensor. To address this, the data was interpolated to ensure consistency and accuracy.
The standard deviation, denoted as σ, was computed for each sensor across the different test repetitions to quantify the variability in pressure readings. It is calculated using the formula:

$$\sigma = \sqrt{\frac{1}{M}\sum_{i=1}^{M}(p_i - \bar{p})^2} \tag{5.1}$$

where p_i represents the pressure reading from test repetition i, $\bar{p}$ is the mean pressure value across all test repetitions, and M is the total number of repeated tests. This statistical measure provides error bars for the pressure data, representing the variability in measurements due to flow fluctuations, sensor accuracy, and experimental repeatability. To ensure a clear representation, the computed standard deviation is applied as symmetric error bars in the plots, visualizing the range of variation for each sensor location and showing deviations that may arise due to possible localized inconsistencies. The pressure data and corresponding error bars are plotted as a function of the normalized sensor position (x/R_t), where R_t is the throat radius, allowing for a consistent comparison across different modules.

5.2 Image processing

Schlieren high-speed images from the two different cameras were taken with various shutter speeds and exposure settings to enhance the visibility of flow features. Reduced exposure times resulted in darker images, which needed to be brightened for better contrast.
Specific MATLAB functions for imaging reading were used for this objective. The `imread` function was used to read the image at the specific selected frame, followed by the application of the `imadjust` function to enhance the brightness. The `brightness_factor` was slightly increased (e.g., 1.1) to adjust the pixel intensity values, improving the clarity and visibility of flow features. These steps ensured that the plume characteristics were more visible, facilitating a clearer visualization and presentation of the experimental data.

5.3 Time-resolved imaging

This section describes the process of analyzing the frequency content of high-speed Schlieren images series. In this case, Welch's method was used for Power Spectral Density (PSD) estimation. Two methods were originally considered to calculate the PSD: one based on individual pixel spectra and another using the averaged time series of pixel intensities. The energy consistency is checked using Parseval's theorem, and several plots are generated to visualize the results.

Given a time series of pixel intensities $x(t)$, the Power Spectral Density (PSD) is estimated using Welch's method, which involves segmenting the time series into overlapping windows, applying a window function (in this case, Hamming window), and computing the Fast Fourier Transform (FFT) for each segment. The resulting PSD is averaged to obtain a reliable estimate of the signal's frequency content.

The frequency resolution df is given by:

$$df = \frac{f_s}{N} \tag{5.2}$$

where f_s is the sampling frequency, set at $f_s = 100000$ for the ultra-high speed images, and N is the length of the data window. The frequency axis f_{lab} is then constructed as:

$$f_{\text{lab}} = \left(0, \frac{1}{N}, \ldots, \frac{N}{2} - 1\right) \cdot df \tag{5.3}$$

5.3.1 Code Description

The MATLAB code processes two sets of Schlieren images from different experimental conditions, NPR = 22 and NPR = 26, and performs the following steps:

1. Loading Image Data: The images are loaded from two different folders using the `imread` function. For each image, a 3x3 pixel block centered around a specific coordinate, indicated by the user, is extracted. A small pixel block is chosen to avoid considering only a single pixel, which would be too variable. A single pixel would not provide a stable measurement, while a 3x3 block ensures the average is meaningful and still representative. In these cases in which flow separation is concerned, the pixel block is chosen to be taken from the boundary layer region just at the nozzle exit and close to the nozzle lip.

2. Welch PSD Computation (Method 1): For each pixel in the 3x3 block, the PSD is computed using Welch's method with the following function:

$$P_{\text{xx}}(f) = \text{pwelch}(x(t), \textit{hamming}(N), \text{noverlap}, N, f_s) \tag{5.4}$$

   where $x(t)$ is the time series of pixel intensities, $\textit{hamming}(N)$ is the Hamming window, N is the window length, noverlap is the number of overlapping points, and f_s is the sampling frequency.
   The MATLAB functions `pwelch` computes the Power Spectral Density using Welch's method. It segments the input time series, applies a window function, and computes the FFT.

3. Averaged Time Series PSD (Method 2): The alternative way of averaging the different pixels data, consists of averaging the time series of pixel intensities across the 9 pixels in the 3x3 block, and then computing the PSD for this averaged time series. The function used is the same as the one above, but with the averaged time series as input.

4. Energy Consistency Check (Parseval's Theorem): The energy of the signal is calculated both in the time domain (variance) and in the frequency domain (integral of the PSD). The ratio between the two is computed to verify the energy consistency, which should ideally be close to 1, as stated by Parseval's theorem:

$$\text{Energy Ratio} = \frac{\int_0^{f_{\max}} P_{\text{xx}}(f)\, df}{\text{Var}(x(t))} \tag{5.5}$$

5. Plotting: There are several ways in which plots can be generated to visualize the results:

   - Non-Premultiplied Spectrum (Log-Log): The PSDs for both methods (individual pixels and averaged time series) are plotted on a log-log scale.
   - Premultiplied Spectrum (Semi-log X): The PSDs are multiplied by the frequency and plotted on a semi-logarithmic scale.
   - Premultiplied Spectrum (Log-Log): The PSDs, pre-multiplied by the frequency to get a better readability of the plot, are also plotted on a log-log scale.

In the end, in the Results are presented only the Premultiplied Semi-log X plots, obtained by averaging the intensity value over the 9 pixels, getting one value for each frame, and then make a time-series of the 9-pixel-average intensity value. Using either of the two ways did not end in having big differences in the frequency peak, but only in the amplitude. In this way, the area under the graph visually represents the total energy in the signal.

This follows from the relationship:

$$\text{Variance} = \int_0^{f_s/2} G_{UU}(f) \cdot f\, d\log f = \int_0^{f_s/2} G_{UU}(f)\, df \tag{5.6}$$

Since:

$$\frac{d\log f}{df} = \frac{1}{f} \quad \Rightarrow \quad f\, d\log f = df \tag{5.7}$$

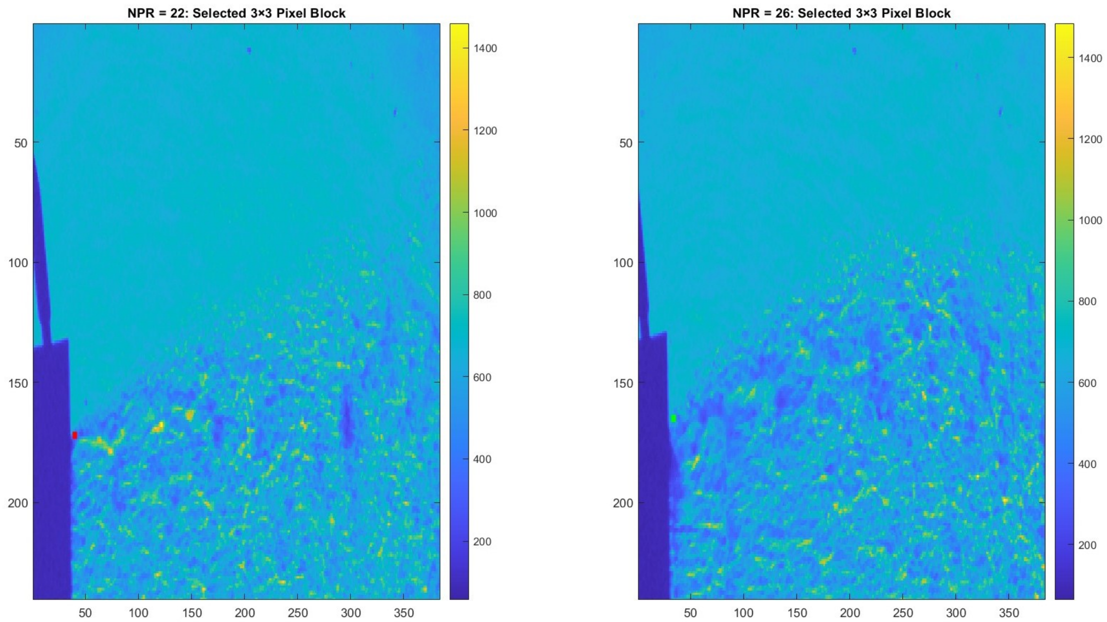

Figure 5.1: 3x3 pixel block selection for NPR=22 and NPR=26

Chapter 6

Results

This chapter presents the findings of the current research, structured into three key sections: cap shock visualization, an in-depth discussion on flow unsteady phenomena, and flow asymmetries at lower NPR.

6.1 Cap shock visualization

As known from previous experiments [53, 54], while the TIC nozzle features a classical Mach disc pattern, the internal shock in TOP nozzles merges into a cap shock pattern. This shock pattern results from an interaction of the overexpansion or the separation shock (coming from the nozzle wall) and an inverse Mach reflection of the internal shock at the nozzle centerline. A specific test was conducted to visualize the cap shock by operating at the maximum NPR achievable within the tunnel constraints, considering the aforementioned limitations due to losses in the circuit. The NPR for this test was 32.8, and the resulting visualization of the shock exiting the nozzle lip section is shown in Figure 6.1. The image is processed by contrast enhancing in order to have a better visualization of all the flow details.

The high sharpness of the figure allows for a detailed visualization of various flow structures. One can clearly identify the curved cap shock as it exits the nozzle, along with the separation shocks occurring near the nozzle lip on both the upper and lower sides. Additionally, the shear layer is distinctly visible, as well as the expansion fans originating from both the internal and external jets. The presence of horizontal flow streaks is also clear. Notably, a certain degree of regularity can be observed in the overall plume pattern, indicating a structured and predictable behavior of the flow.

Furthermore, the position and dynamics of the Mach disk are accurately captured in the grayscale pseudo-schlieren CFD visualization shown in Figure 6.20. This high level of agreement between the visualization and the computational results

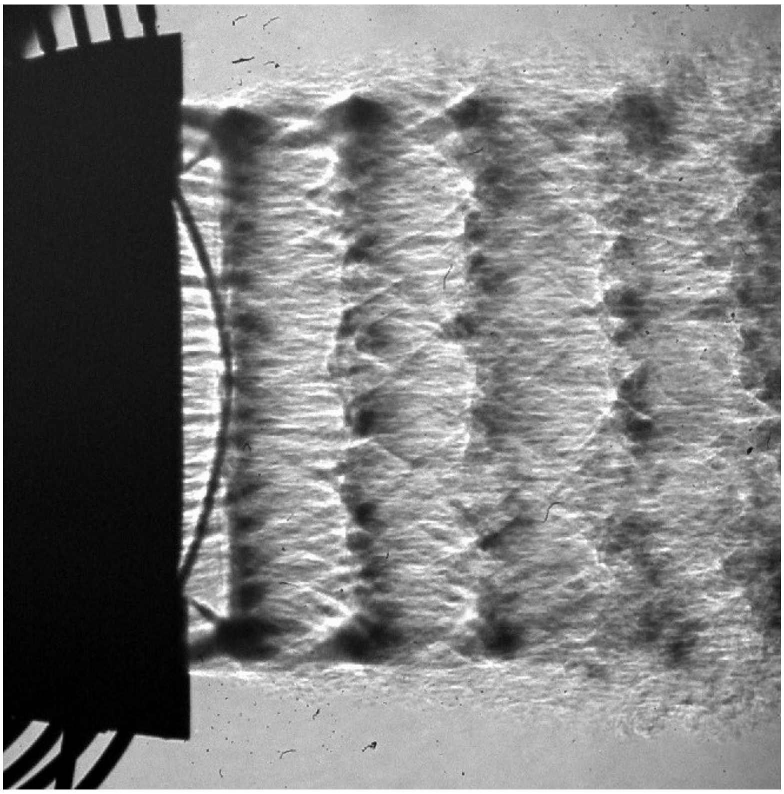

Figure 6.1: Schlieren cap shock visualization (NPR=32.8)

demonstrates the capability of the RANS steady-state simulation in effectively predicting the complex flow dynamics within the nozzle.

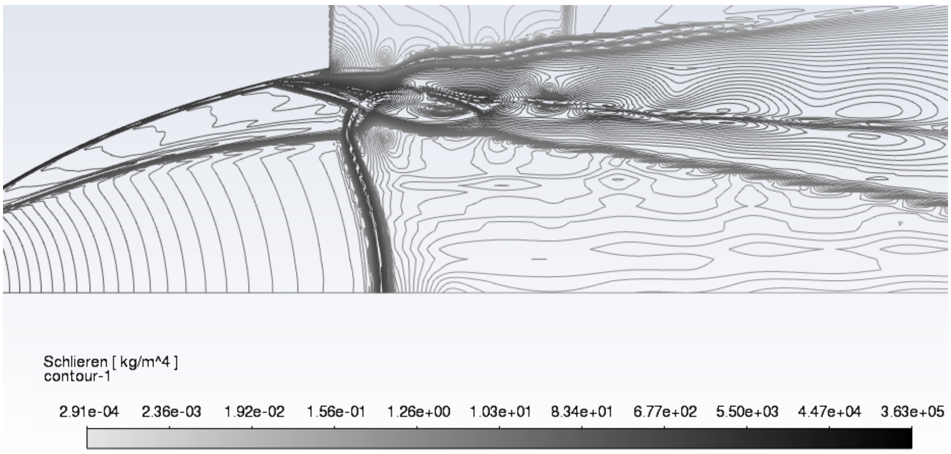

Figure 6.2: CFD pseudo-schlieren cap shock visualization (NPR=32)

6.2 Flow unsteady phenomena

To understand where the pressure peaks inside the nozzle occur—since these peaks reflect the interaction between the separation bubbles and the nozzle wall—the pressure measurements in the startup transient at varying NPR values, referred to the last pressure sensor before the nozzle exit (sensor 16 in each of the three equally azimuthally distributed pressure arrays) are plotted in Figure 6.3. Specifically, the pressure readings are discretized over time steps, which serve solely to indicate the timing of the measurements. The key variable to consider is, as mentioned, the variation of the Nozzle Pressure Ratio (NPR) on the x-axis. This variable cannot be precisely discretized in the graph because the valve regulating the NPR, as explained in the Test Setup chapter, is manually operated, as a consequence only the peaks' NPR is indicated.
The first pressure peak occurs at around NPR=22, representing the highest peak observed. This peak corresponds to the reattachment of the separation bubbles to the nozzle wall. The transition between the two distinct flow regimes — from Free Shock Separation (FSS) to Restricted Shock Separation (RSS) — and the movement of the separation shock closer to the nozzle wall intensify its interaction with the turbulent boundary layer, thereby generating this pressure peak.
After the transition, the flow remains in the RSS regime, which is more stable than the FSS condition. As a result, the pressure decreases. However, when the last recirculation bubble opens to the ambient environment due to a further increase in NPR, a second pressure peak appears. This peak corresponds to the End Effect regime, around NPR=26, where the external flow significantly influences the internal nozzle flow near the exit. These two phenomena are confirmed to generate the highest wall pressure peaks inside the nozzle. Additionally, as indicated by the differences in pressure readings across the three modules, the flow exhibits asymmetry, which implies that these phenomena also contribute to the highest side load peaks. Although side loads were not directly measured in this test campaign, the asymmetry observed in the pressure distribution supports this conclusion.
The in-depth analysis of the two phenomena will be presented separately in the following sections.

6.2.1 Free Shock Separation to Restricted shock separation transition

The phenomenon of flow attachment to the nozzle wall, characterized as Restricted Shock Separation and following the Free Shock Separation regime, is thoroughly explained and analyzed through a comprehensive comparison of various experimental visualization techniques such as Schlieren imaging, oil flow visualization, shadowgraphy, and wall pressure measurements within the nozzle, along with

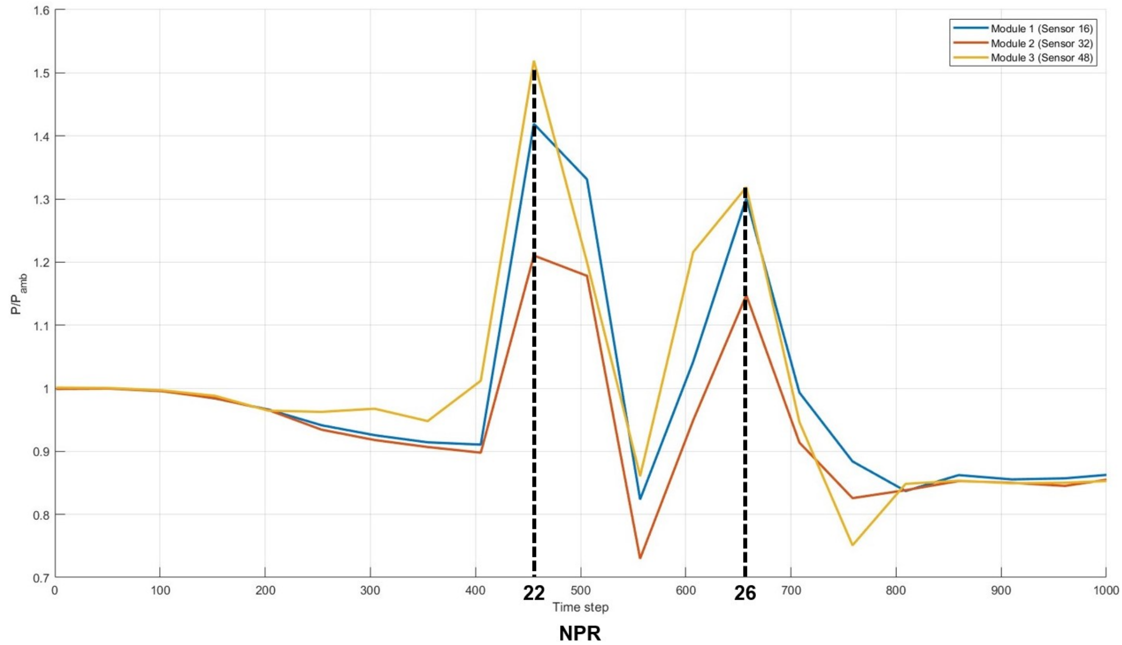

Figure 6.3: Wall pressure readings at variable NPR

numerical results from Computational Fluid Dynamics analyses.

The exhaust plume is first clearly visualized using high-resolution Schlieren imaging (Figure 6.4). What is not visible in individual frames but becomes apparent in the video sequence is a distinct flapping motion that causes the first part of the exhaust plume to move unsteadily up and down near the nozzle lip.

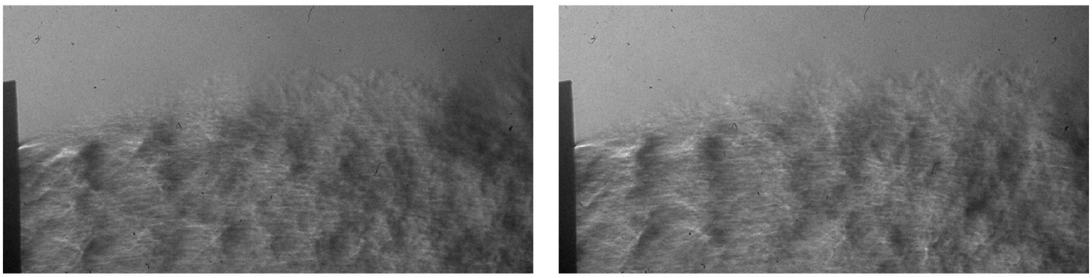

Figure 6.4: Schlieren RSS visualization (NPR=22) at 20,000fps

The boundary layer behavior, analyzed using the Shadowgraphy technique by removing the Schlieren vertical knife from the system, confirms its oscillatory nature, which becomes evident in sequential Shadowgraphy images. The RSS regime is strongly influenced by turbulent Shock-Wave Boundary Layer Interactions.

Although this phenomenon primarily occurs inside the nozzle, its effects extend to the exhaust plume due to the unsteadiness of the separation bubble.

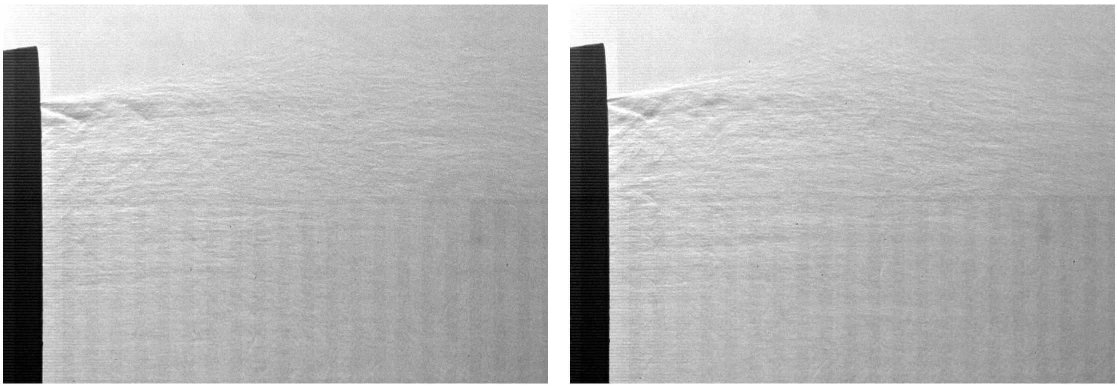

Figure 6.5: Shadowgraphy RSS visualization (NPR=22)

To also obtain insights on the flow flow behavior inside the nozzle, an oil flow test was conducted to examine asymmetries in the separation front position. In the Restricted Shock Separation regime, the denser white line corresponds to separation areas where oil accumulates, making the separation front and streamlines clearly visible. The dense streaks along separation lines result from heightened shear stresses and significant changes in flow behavior, such as detachment from the surface due to adverse pressure gradients. These streaks form as the oil accumulates in areas of intensified shear before being displaced by the flow. This test, conducted with a rapid increase of NPR until the target value and then maintained that NPR for 10 seconds, is particularly useful for validating CFD simulations by comparing the observed separation line position with numerical results, as shown in Figure 3.3.

It is also important to note that while asymmetries are theoretically present, and are confirmed by the following pressure readings, they are not really visually detectable in an oil film test. In contrast, these asymmetries become clearly evident in visualizations at lower pressure ratios.

The pressure readings, plotted in MATLAB, represent the mean values from multiple tests. Bars indicating the standard deviation are included to reflect the variability in the data in different experiments. This method is crucial for assessing the experiment's repeatability, as the inherently unsteady nature of the phenomenon can cause pressure oscillations that influence the measurements. Two different plots are reported: the first aims at comparing, in the single test, the values registered by the three different pressure modules, this is done for the three tests that are made with a rotation of the nozzle, to state flow asymmetries. The second is instead plotting what the same module registers within the different tests

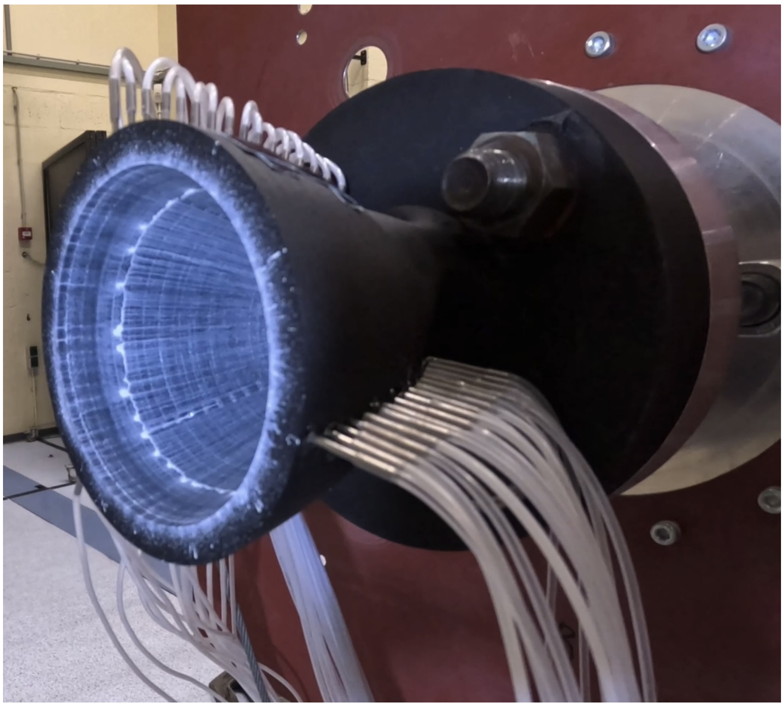

Figure 6.6: RSS oil film separation visualization

with rotated nozzle configurations. This is indeed made to state asymmetries in the internal part of the nozzle that could be linked to manufacturing and to the internal sanding process.

Generally speaking, in both cases, the pressure measurements appear consistent until reaching the last three sensors of the array. This can be explained by the fact that this region is most affected by the unsteady motion of recirculation bubbles interacting with the boundary layer.
Flow asymmetry is a well-documented phenomenon in theory, particularly in relation to the transition from Free Separation (FSS) to Restricted Separation (RSS) conditions, because it is reported as main driving cause for the side-loads happening in the nozzle. The observed differences in flow behavior between the three modules during the same test can be attributed to these flow asymmetries. Conversely, the results from the same module across different tests show greater consistency, with variations small enough to suggest that internal geometric imperfections have a limited impact on the measurements.
Further evidence of flow asymmetry is clearly visible in Figure 6.9 and Figure 6.10. In this example, one side of the nozzle flow has already undergone the transition from Free Shock Separation to Restricted Shock Separation, resulting in flow reattachment. Simultaneously, the opposite side of the flow remains in a free

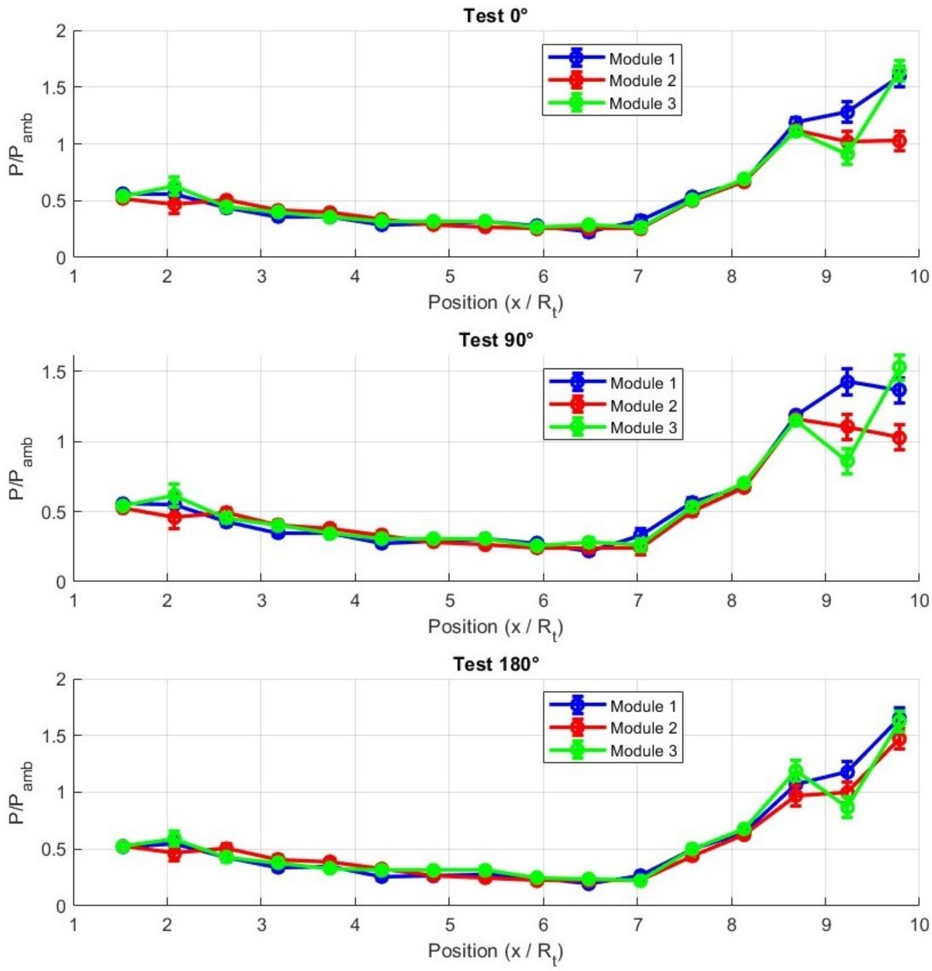

Figure 6.7: Wall pressure readings at NPR=22 - different tests comparison

separation state. This asymmetry becomes even more apparent when comparing tests conducted at different nozzle orientations—specifically the "90 degrees" and "180 degrees" tests shown here. These observations provide a clear explanation for the asymmetries observed in the pressure measurements. As a consequence, it is worth noting that when considering only half of the nozzle for Schlieren visualization to determine the exact NPR at which the transition occurs, the pressure sensors in the remaining part of the nozzle may detect a flow that has not yet fully transitioned.

Preassure measurements from cold flow tests were also compared with the ones obtained by Computational Fluid Dynamycs analyses.
The comparison is shown in the plots of Figure 6.11. The observed slightly higher values in the test results compared to the CFD predictions are consistent with the

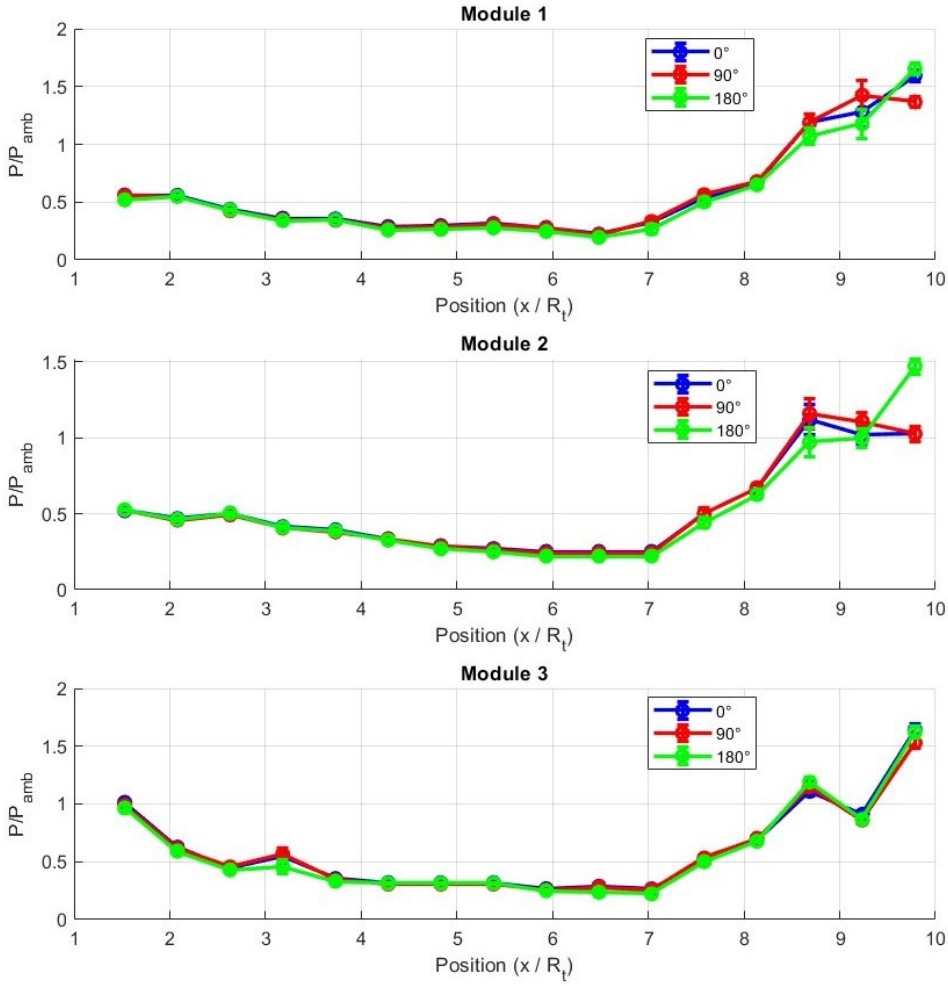

Figure 6.8: Wall pressure readings at NPR=22 - different modules comparison

findings from Ostlund et al.'s experiments [55]. As one can see, even if the CFD values are slightly underpredicting the pressure peak, the comparison in the end results as very good, confirming the goodness of the numerical calculations on the prediction of separation phenomena, despite the simplification assumptions made.

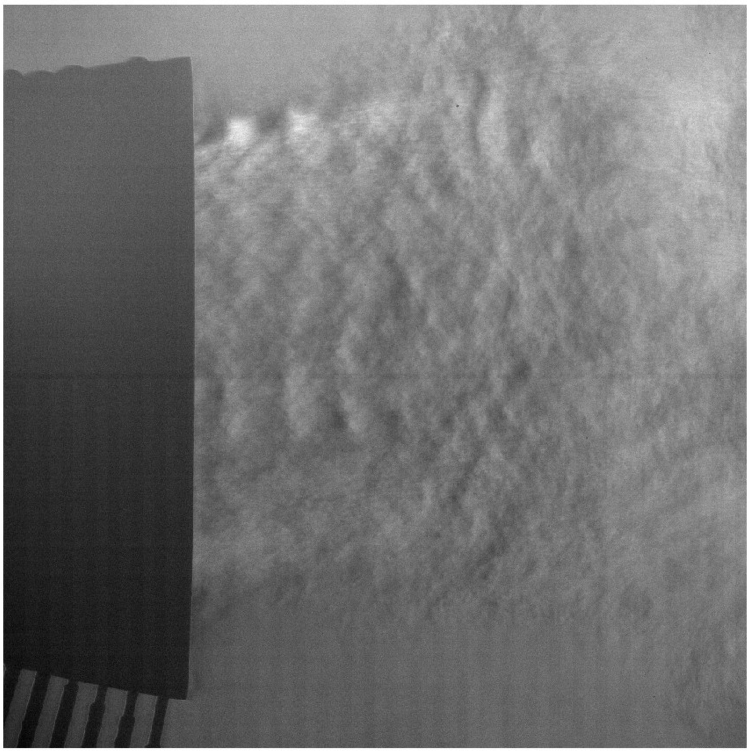

Figure 6.9: Asymmetric separation - 90deg test

Finally, a ultra-high-speed Schlieren visualization at 100,000 fps, with an inevitably lower resolution compared to the previous visualizations, is used to perform a frequency analysis of the intensity signals.

The premultiplied spectrum with a semilog-x representation is reported in Figure 6.13, allowing to correlate the total energy of the signal with the area under the graph. Thus, the premultiplied spectrum $G_{UU}(f) \cdot f$ ensures that the visualized area directly corresponds to the signal's variance.

The first frequency peak is excluded from the representation since it is caused by a drift in the signal, while higher frequencies are excluded as well for presenting very high amplitude peaks, possibly due to camera noise. In the analyzed region, the flow exhibits peak unsteadiness around 300-400 Hz (limit for low to mid frequency), coinciding with the FSS to RSS transition, making it the most energetic event in the sequence. The amplitude variations are indicating the presence of a strong oscillatory mode. This suggests a more pronounced unsteady motion in this frequency range, likely linked to shock-induced separation dynamics. Previous studies ([31]) on a nozzle with the same contour but a different scale reported similar findings using dynamic wall pressure transducer measurements. However,

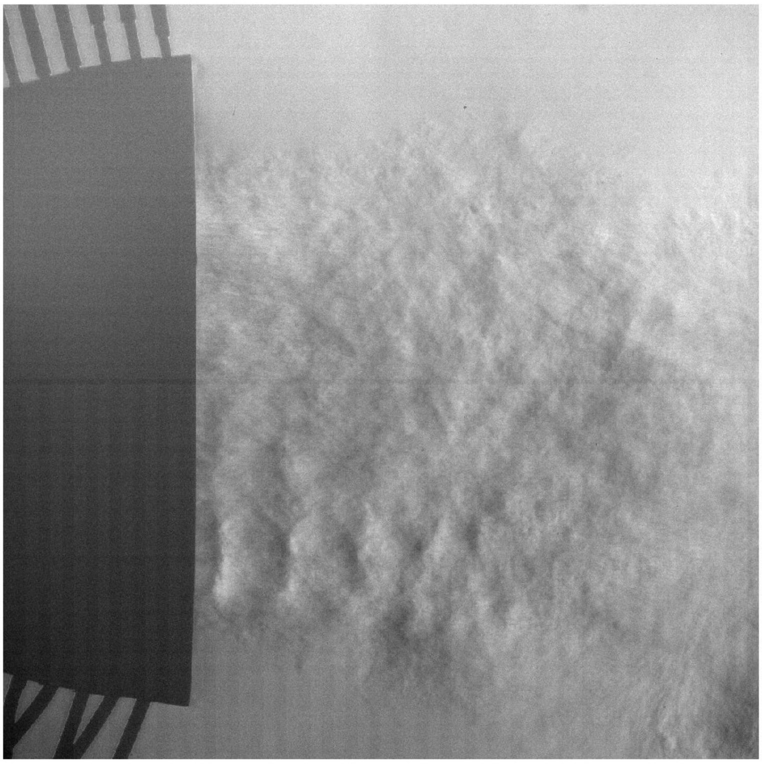

Figure 6.10: Asymmetric separation - 180deg test

due to differences in nozzle dimensions, a direct quantitative comparison is not feasible, but can represent a baseline for further studies.

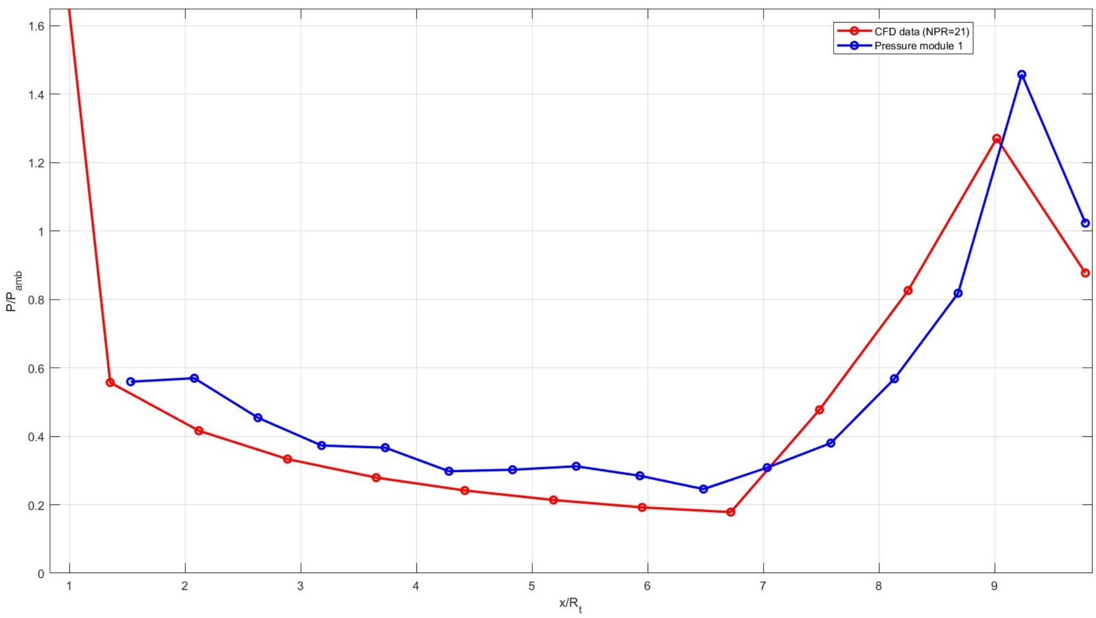

Figure 6.11: Wall pressure comparison between CFD and pressure arrays (RSS)

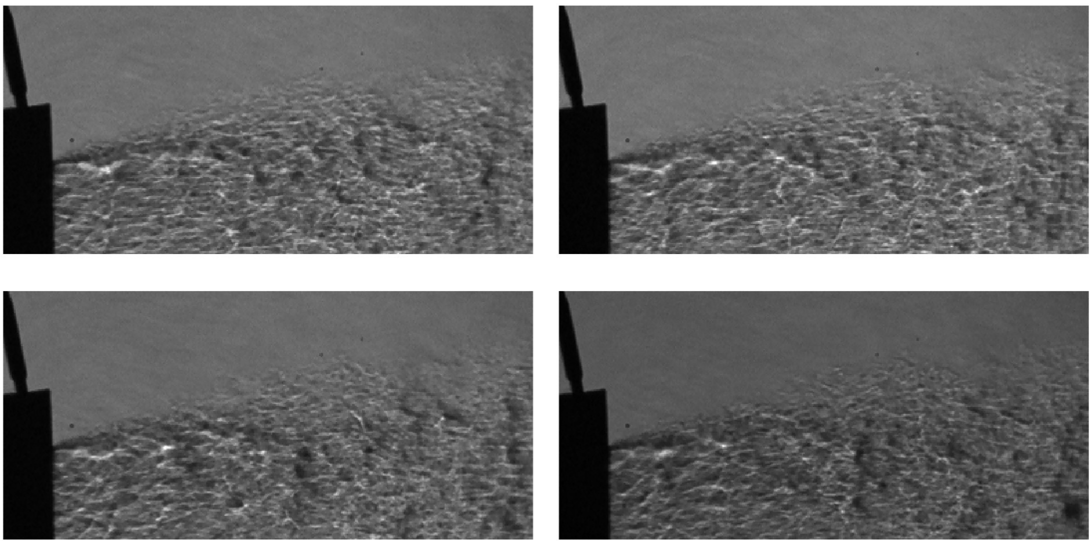

Figure 6.12: Schlieren RSS visualization (NPR=22) at 100,000 fps

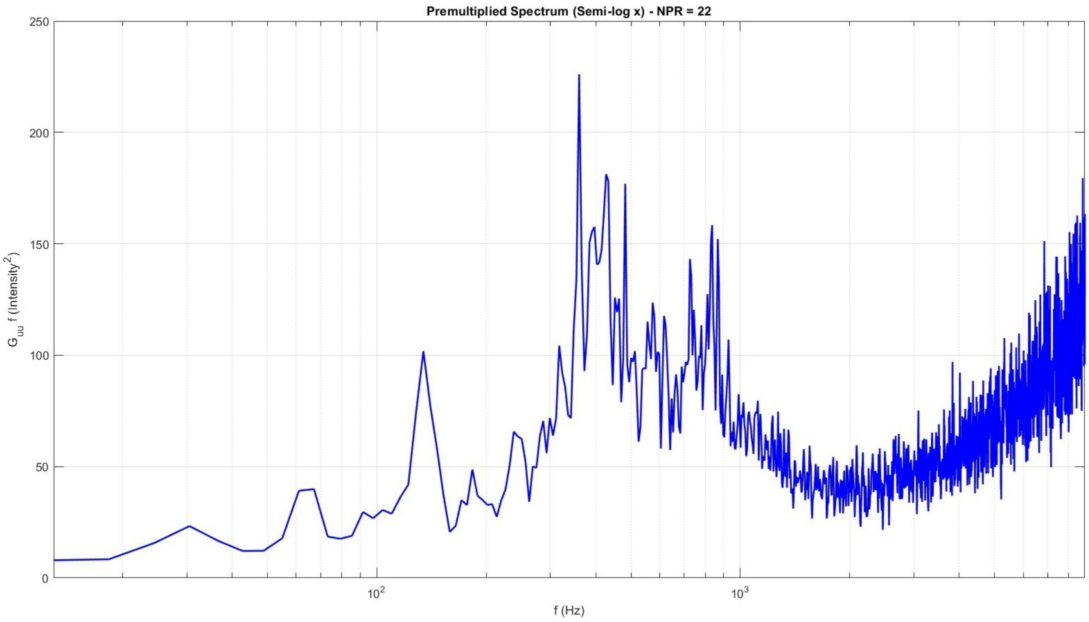

Figure 6.13: Premultiplied spectrum (NPR=22)

6.2.2 End Effect Regime

Increasing NPR up to 26, the transition to the End Effect Regime happens. The same investigation as the one performed for the FSS to RSS transition, was made for this effect, that historically has been less analyzed with respect to the aforementioned phenomenon. The results are thus important for helping to understand and explain, as well as visualize, the physics of the End Effect.

First of all, the Schlieren 20,000 fps visualization in Figure 6.14 is clearly showing how a more turbulent pattern appearance right at the nozzle exit, where, as known from theory, the latest recirculation bubble opens to the external ambient. The small recirculation pocket has moved downstream, so that the separation is located too far downstream for the reattachment to occur and a diverging plume is observed.

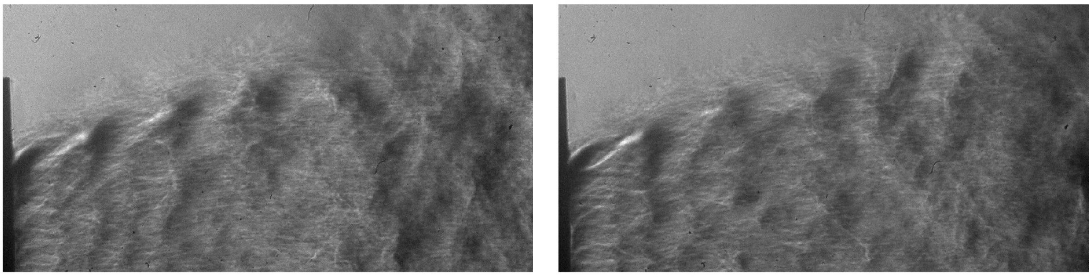

Figure 6.14: Schlieren EER visualization (NPR=26) at 20,000 fps

The boundary layer visualization also captures this effect.

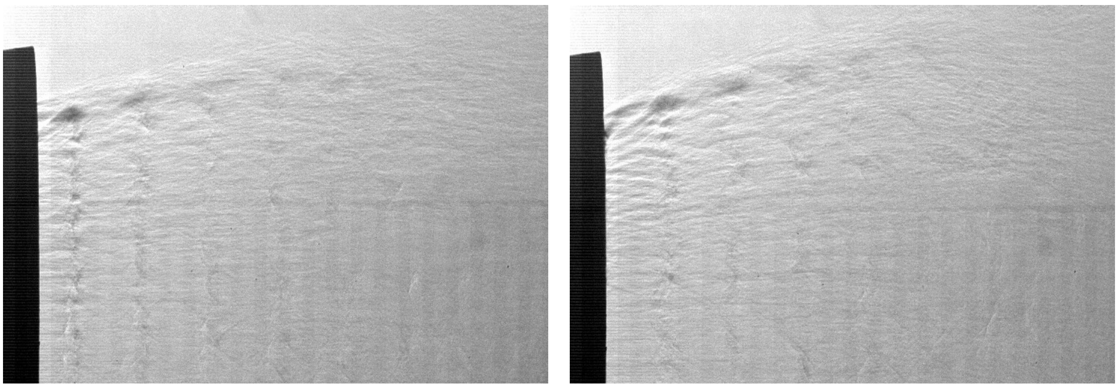

Figure 6.15: Shadowgraphy EER visualization (NPR=26)

As of the end effect, as the NPR increases, both the separation point and the point of partial reattachment shift slightly downstream, and this can be seen in the oil film visualization. At NPR=26, the location of partially reattached flow reaches the nozzle exit, resulting in the opening of the partially closed backflow region. This allows ambient air to rush in, causing the separation point (X_{sep}) to move downstream by approximately 7–8 mm, as illustrated in Figure 6.16. During the shutdown, this phenomenon, marks the point where the flow can no longer reattach (even partially) to the nozzle walls.

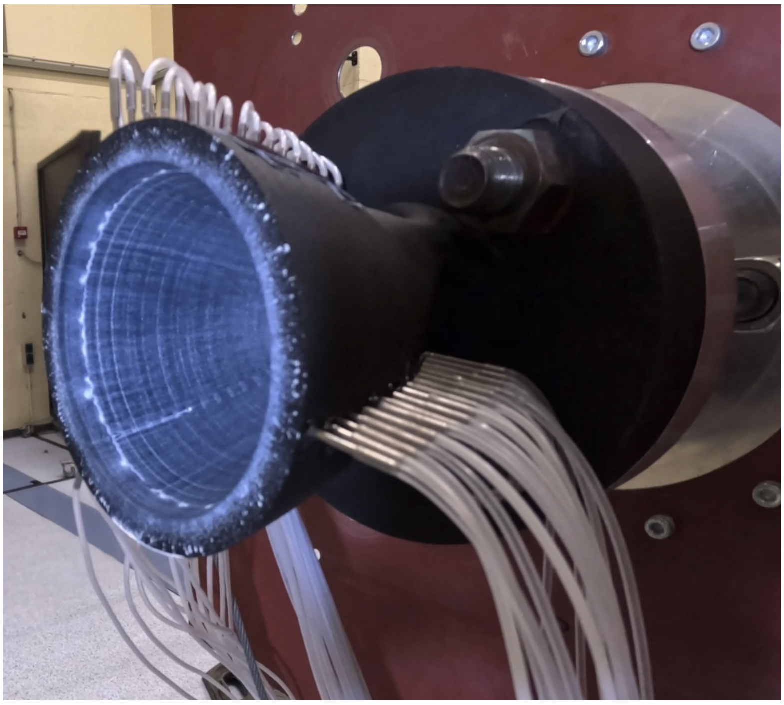

Figure 6.16: EER oil film separation visualization

In the oil flow visualization, it is not visible, or at least it is least clear at a naked eye, the asymmetry of this separation phenomenon. With respect to the FSS to RSS, on the other hand, the pressure measurements of the different modules do not show that much asymmetry either. So one can deduct that the asymmetry is decreasing form the Free Separation Shock condition progressively to the higher NPR unsteady phenomena.

In addition, both wall pressure sensor readings and CFD calculations reveal a clear distinction between the two flow transition phenomena. In the case of the End Effect, the final pressure port always records the peak pressure, while the interaction of separation bubbles in the RSS leads to varying pressure peaks, with the wall pressure fluctuating between its value in the backflow region and that above ambient as a function of time. This could be explained by the fact that EER is characterized by the full reopening of the partially closed backflow region, allowing ambient air to accelerate back into the nozzle.

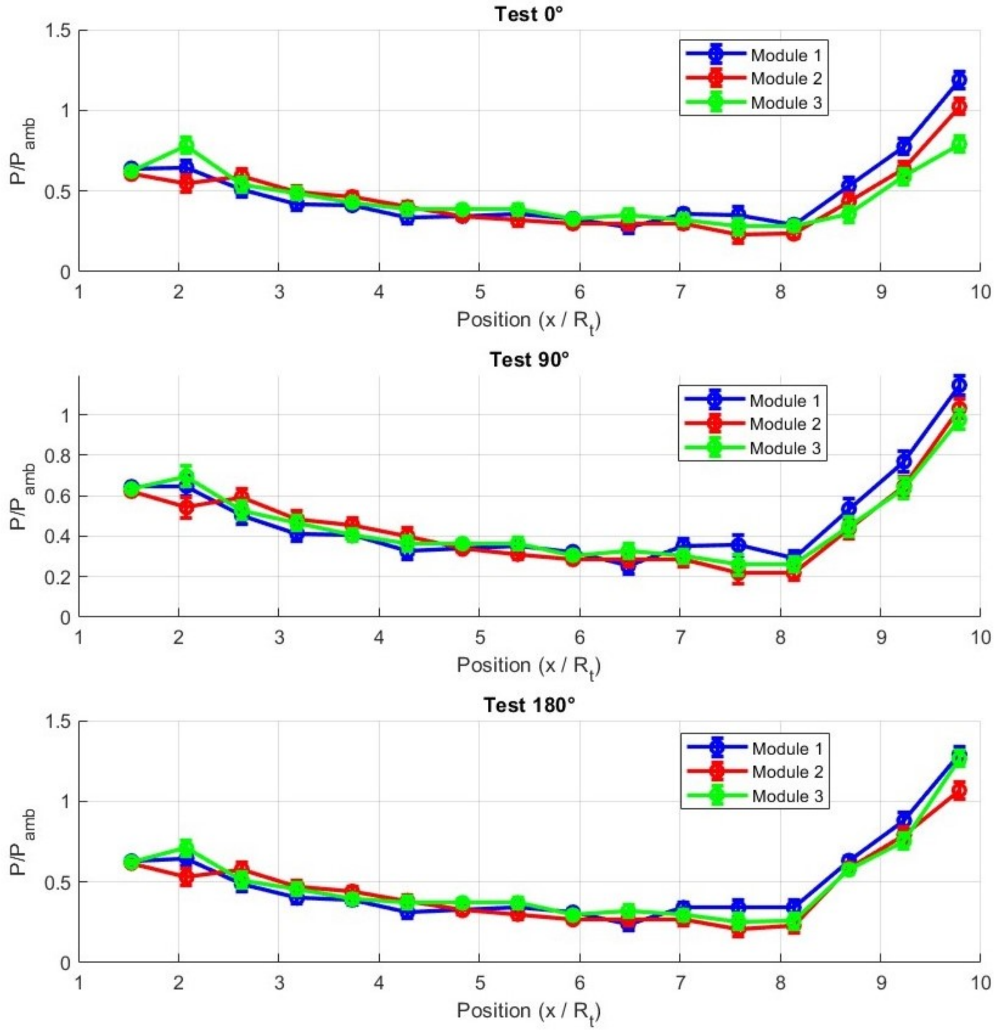

Figure 6.17: Wall pressure readings at NPR=26 - different tests comparison

A good correlation of CFD data is evident also in the case of the End Effect, and presented in Figure **??**.

Ultra-high-speed images at a recording rate of 100,000fps were used to perform the exhaust plume frequency analysis, based on Schlieren visualization and thus on the variation in intensity of the pixels, leading to the spectrum shown in Figure 6.21. The spectrum for NPR=26 shows a smoother transition, suggesting a more gradual energy distribution with fewer dominant unsteady modes in the mid-range, while still exhibiting increased intensity beyond 1000 Hz. Less intense flow oscillations are registered, and the peak in amplitude is around 400 Hz, slightly higher than the one for RSS regime.

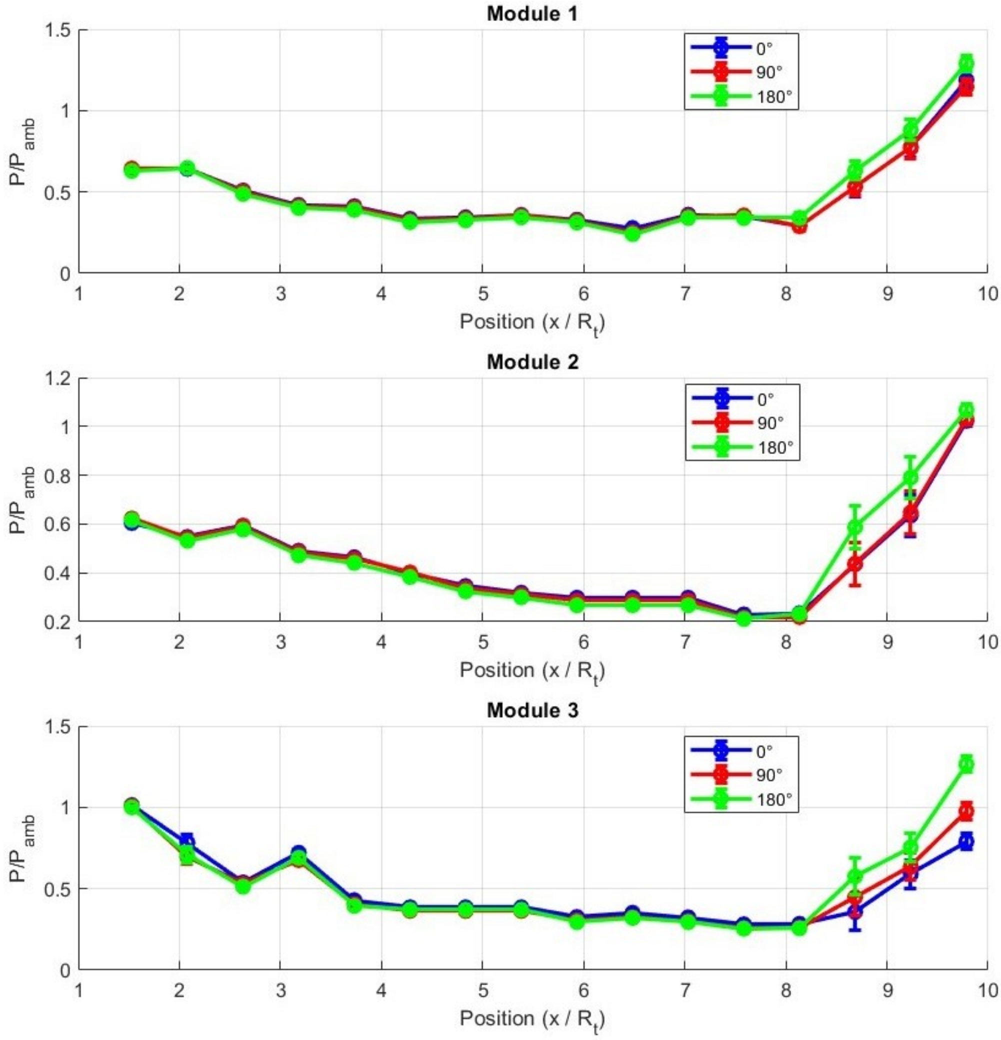

Figure 6.18: Wall pressure readings at NPR=26 - different modules comparison

Hysteresis

The hysteresis effect notably affects the shutdown Restricted Shock Separation to Free Shock Separation transition, such that it happens at NPR=11.4, while in the startup is occurring at NPR=22 for the studied nozzle. The tests confirmed that the End Effect, instead, is not affected by hysteresis and the pressure rate stays the same even in the shutdown transitory. Unlike the interior regions where shock-induced boundary layer separations (like FSS to RSS transition) exhibit hysteresis due to flow history, the flow at the nozzle exit is governed primarily by external atmospheric interactions and the jet expansion dynamics. These factors are less susceptible to the history-dependent effects driving hysteresis within the nozzle for

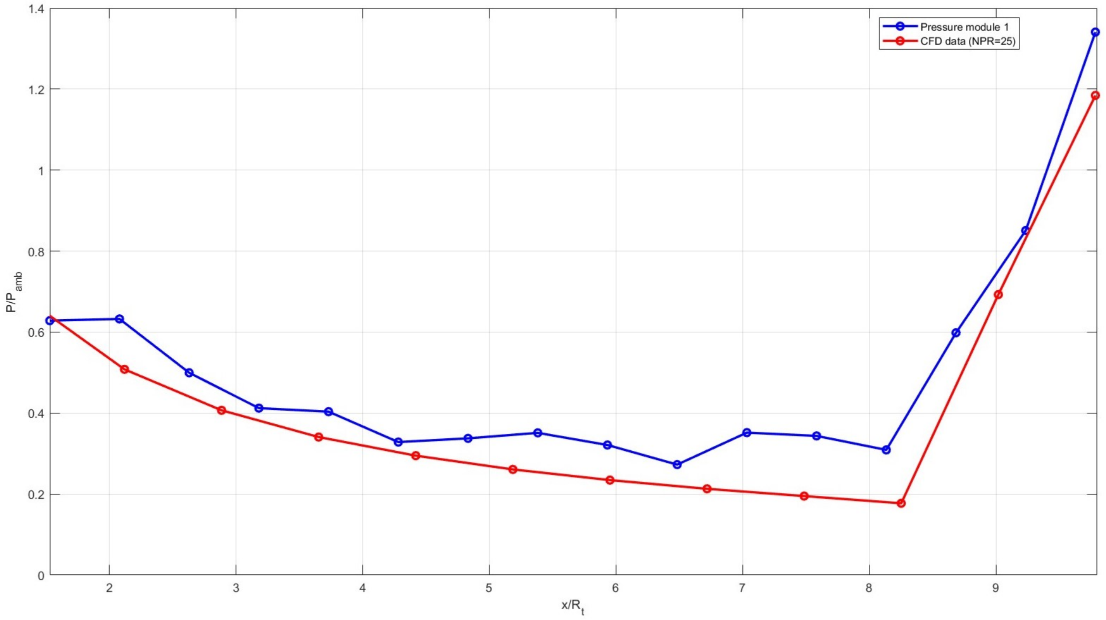

Figure 6.19: Wall pressure comparison between CFD and pressure arrays (EER)

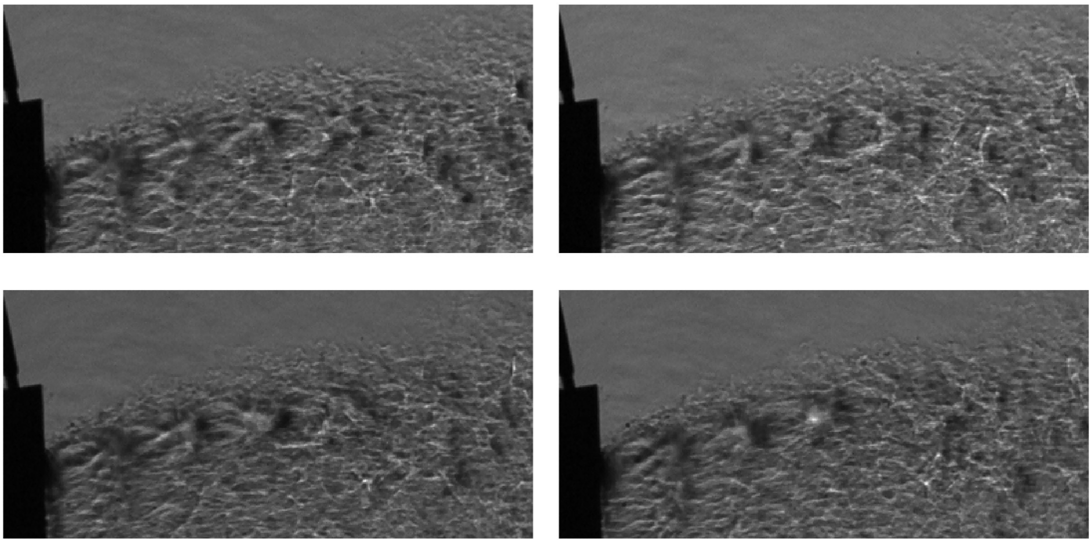

Figure 6.20: Schlieren EER visualization (NPR=26) at 100,000fps

RSS. Specifically, the flow conditions at the exit depend on the external pressure and expansion state of the exhaust plume, which are dictated by the nozzle's geometry and the external environment rather than internal shock structures. Therefore, the pressure distribution near the exit appears to remain relatively stable.

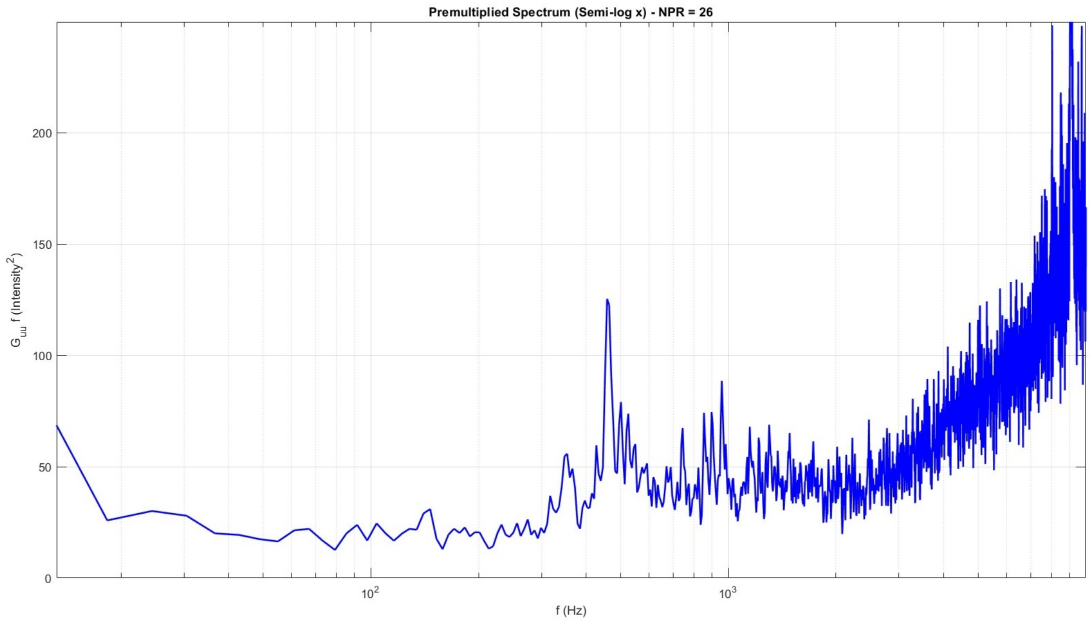

Figure 6.21: Premultiplied spectrum (NPR=26)

6.3 Flow asymmetries at low NPR

The oil film experiments were meant to provide valuable insights into the separation behavior, as already seen in the previous sections for FSS to RSS transition and for the End Effect Regime. Those tests illustrate the varying locations of the separation point under different NPR conditions, so they were used also for lower NPR asymmetries analyses. The analysis of images and video footage reveals noticeable asymmetries in the separation line (thick white line) during the startup transient phase when the regime is still in Free Separation, as shown in Fig. 6.22. However, such asymmetries are less discernible to the naked eye under the conditions of RSS and EER, as previously explained. The key outcome of this experiment is the validation of the asymmetrical separation regime. This asymmetry can be attributed to both the theoretical asymmetry inherent in the separation process and manufacturing imperfections in the nozzle itself.

Pressure readings for the corresponding NPR value are presented in Figure 6.23, where it is evident that Module 3 exhibits a distinct behavior compared to the other two modules. This module also corresponds to the region of maximum asymmetry, as observed in Figure 6.22(b).

Flow separation in a nozzle occurs when the local pressure drops significantly relative to ambient pressure, causing the fluid stream to detach from the nozzle wall. The rightward shift of the curve for Module 3 indicates that pressure remains

(a) Left camera **(b)** Right camera

Figure 6.22: Asymmetry in separation line (oil film)

higher over a longer distance before experiencing a sharp drop. This suggests that the flow remains attached to the wall further downstream compared to the other two modules, leading to a delayed separation point along the nozzle axis.

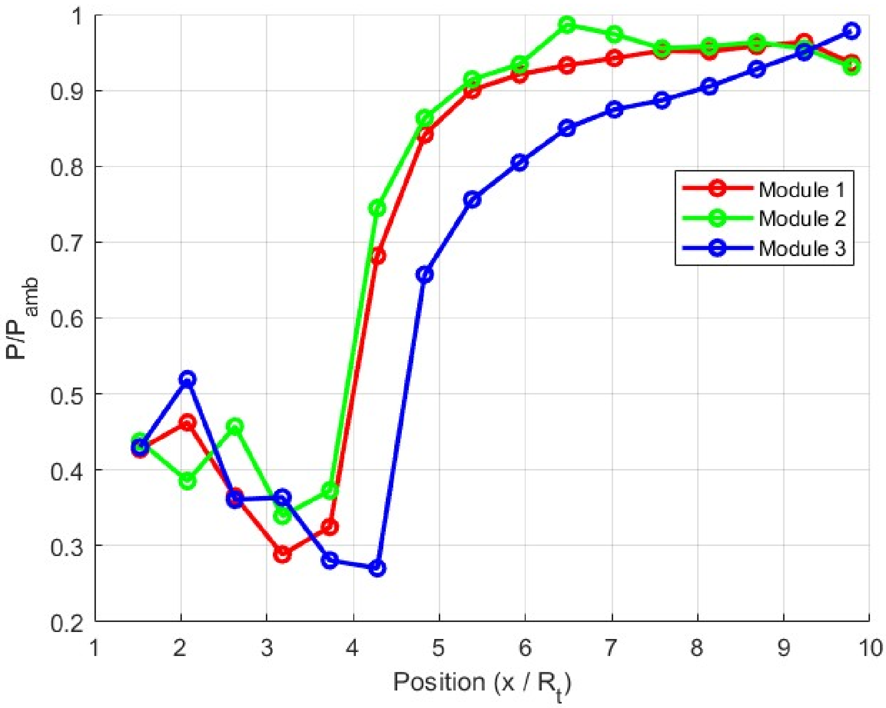

Figure 6.23: Pressure readings low NPR

Chapter 7

Conclusions

This final chapter synthesizes the conclusions from the research presented in this master thesis. It begins by revisiting the original thesis objectives and research questions that guided the study, summarizing the key results and insights. This chapter highlights the main contributions of the work and discusses possible recommendations for future work.

At the start of the research, the following objective was formulated as:

"The objective of this research is to experimentally investigate flow unsteadiness phenomena in a truncated Thrust-Optimized Parabolic (TOP) rocket nozzle, utilizing the TU Delft nozzle test setup. This study focuses on capturing and analyzing unsteady flow behaviors, particularly gaining insights into the end-effect regime. To accomplish this, a range of experimental techniques will be employed, including oil film visualization, synchronized wall pressure measurements, and high-speed Schlieren imaging. Additionally, the research aims to conduct an exhaust plume frequency analysis and validate the experimental findings against CFD simulations."

The nozzle, a truncated version of a thrust-optimized parabolic contour presented in the literature, was successfully designed and validated using Computational Fluid Dynamics analyses. This validation confirmed that the nozzle is capable of investigating a range of unsteady phenomena, including the end-effect regime, and also the visualization of part of the cap-shock structure exiting the nozzle, all within the maximum pressure limits of the TU Delft High Speed Lab setup.
A comprehensive analysis was performed by integrating multiple visualization techniques, including oil flow visualization and schlieren imaging with wall pressure measurements. Although the attempt to incorporate focusing schlieren imaging as testing technique was unsuccessful due to setup issues, the combined data from the other methods provide an exhaustive overview of the unsteady flow phenomena.

These include the transition from Free Shock Separation to Restricted Shock Separation and the manifestation of the End Effect Regime.
Additionally, frequency analysis was applied to ultra high-speed schlieren images of the exhaust plume to extract the dominant frequencies associated with specific instability phenomena.
Finally, beyond their initial role in validating the nozzle design, the CFD results also serve as a benchmark for comparison with the experimental data.

Now the aim is to answer the research questions outlined in the Introduction, demonstrating the achievement of the majority of the study's objectives.

About FSS to RSS Transition and End-Effect Regime:

1. **At what NPR do unsteady phenomena occur?**
   For the current research nozzle, the Free Shock Separation to Restricted Shock Separation is happening at around NPR=22, while the End Effect Regime at around NPR=26, respecting the maximum limitation of the wind tunnel (NPR=32.8).

2. **What are the flow characteristics that distinguish Free Shock Separation (FSS), Restricted Shock Separation (RSS), and the End-Effect Regime (EER)?**

   - FSS: The flow separates from the nozzle wall without reattaching, creating an oblique shock wave that reflects at the nozzle centerline, forming a Mach disk. This regime is characterized by high wall pressure fluctuations and low-frequency oscillations of the separation point.
   - RSS: The separated flow reattaches to the nozzle wall after a recirculation bubble forms due to the interaction of the internal shock with the nozzle centerline. This leads to additional pressure peaks behind the separation bubble and a more complex shock pattern, referred to as the "cap shock pattern."
   - EER: This regime appears at higher NPR values when the reattachment point reaches the nozzle lip. It is characterized by strong global unsteadiness and a pulsating motion of the latest separation bubble, driven by external flow interactions at the nozzle lip.

3. **What are the specific flow features linked to the End Effect Regime?**
   The EER is marked by a significant wall pressure peak at high NPR values, due to the latest recirculation bubble opening to the open ambient, in the final sections of the nozzle contour. This effects features quasi-axisymmetric pulsation of the recirculation bubble at the nozzle exit and intermittent opening

and closing of the separation bubble to the ambient environment, leading to rapid pressure variations.

4. **Are the experimental data coherent with previous literature findings?** Yes, the experimental data are in strong agreement with previous studies presented in the Literature Review section of this thesis.

5. **How do experimental data compare to the CFD analyses results?** The Computational Fluid Dynamics simulations (RANS-based models) successfully captured the key flow structures and pressure distributions within the nozzle necessary for this research. However, the steady-state turbulence modeling used in the CFD analysis had limitations in fully resolving unsteady separation dynamics, leading to slight discrepancies in the prediction of Mach disk position at a certain NPR.

6. **What are the dominant frequency characteristics of the instabilities in the exhaust plume for different NPR conditions?** During the FSS to RSS transition (NPR=22), dominant low-frequency oscillations (100–300 Hz) were observed in the exhaust plume due to the instability in the recirculation pattern and boundary layer interactions. At higher NPR (EER, NPR=26), the pulsation of the last separation bubble led to fluctuations of smaller amplitude with a slightly higher peak in frequency, around the 400 Hz.

For what concerns the visualization techniques:

1. **How do different visualization techniques compare in capturing flow separation phenomena?** High-speed Schlieren imaging captures shocks and expansions structures and plume dynamics with high spatial and temporal resolution. Shadowgraphy highlights density gradients in the flow but is less sensitive to weak shocks and separation features compared to Schlieren. Oil film visualization clearly identifies separation lines and reattachment regions on the nozzle wall but does not capture real-time flow evolution. Focusing Schlieren should have enhanced depth resolution and minimized background noise, improving the visualization of three-dimensional separation effects, but it was not successfully implemented.

2. **How does the use of oil film visualization complement optical techniques in identifying separation lines and flow reattachment?** Oil film visualization reveals detailed surface flow structures, streak lines, and separation points, which complement Schlieren images that primarily highlight shock wave patterns happening in the internal part of the nozzle. The combination of this technique with the others and with wall pressure readings, allows for a more complete understanding of the separation process and its interaction with the nozzle wall.

3. **Can the implementation of a Focusing Schlieren setup provide deeper insights into the three-dimensional effects in the unsteady flow separation phenomena?** The focusing schlieren technique was tested in a proof-of-concept setup to visualize shock structures while minimizing three-dimensional flow contamination. However, alignment challenges and optical component limitations affected precision. Despite this, the setup optimized key parameters like field of view and depth of focus. A self-aligning version was considered but not used due to cost and complexity.

Recommendations and future work

Building upon the original research objectives and the findings of this experimental study, several key recommendations can be formulated to guide future research efforts. The insights gained during this investigation provide a solid foundation for refining experimental methodologies, expanding the scope of analysis, and improving models to further advance the study of flow unsteadiness in TOP rocket nozzles.

- **Focusing Schlieren:** Future iterations of the presented proof-of-concept setup should address the alignment issues identified during the testing of this experimental visualization technique. Incorporating higher-quality optical components, such as a precisely manufactured source grid, may further improve the system's accuracy and reliability. Additionally, integrating alignment mechanisms could significantly reduce the time required for calibration and improve repeatability. These enhancements would not only refine the imaging capabilities of the focusing schlieren system but also enable more detailed and accurate studies in nozzle flow dynamics phenomena, that have not been performed before.

- **Particle Image Velocimetry (PIV):** Since schlieren imaging does not directly capture velocity data, integrating Particle Image Velocimetry (PIV) is recommended to accurately measure the velocity profile within the exhaust plume. This approach would allow for a detailed comparison between experimental results and CFD simulation predictions, thereby enhancing model validation. Additionally, comparing PIV measurements from a truncated nozzle configuration with those from a full (non-truncated) nozzle could provide valuable insights into the influence of nozzle geometry on flow behavior.

- **Wall pressure measurements:** Another key area for improvement involves wall pressure measurement systems. Future experiments could consider incorporating multiple high-frequency pressure transducers, synchronized with

Schlieren imaging, that would allow for frequency analyses in the internal walls of the nozzle, to correlate with the ones performed on the exhaust plume.

- **Shock tracking:** Further investigation can lead to better understand the cap shock structure and its temporal evolution and motion. To extend the current work, time-resolved shock tracking analysis should be conducted for the cap shock, applying a similar approach to that used for the FSS to RSS transition and End Effect Regime, in order to study its flapping and rippling motion. This would involve capturing high-speed Schlieren sequences at the maximum Nozzle Pressure Ratios achievable, and using image-processing techniques to extract shock oscillation frequencies and spatial movements.

- **Comparative frequency analysis:** A comparative analysis of frequency spectra at the nozzle exit using a non-dimensional framework, rather than on absolute frequency values, could yield valuable insights. For example, previous studies on the TOP nozzle have shown frequency peaks that differ from those observed in the current investigation, primarily due to differences in nozzle size and geometry. To facilitate a meaningful comparison, future research should consider normalizing the frequencies using the Strouhal number, carefully selecting appropriate reference values for the characteristic length and fluid velocity, thereby enabling direct comparisons across various nozzle designs, sizes, and NPR conditions.

Appendices

Appendix A: Nozzle contour coordinates

x	y	z
-16.0154	16.3363	0.0000
-15.6808	16.2948	0.0000
-15.3463	16.2249	0.0000
-15.0117	16.1247	0.0000
-14.6770	15.9920	0.0000
-14.3425	15.8230	0.0000
-14.0079	15.6302	0.0000
-13.6733	15.4369	0.0000
-13.3388	15.2438	0.0000
-13.0041	15.0506	0.0000
-12.6696	14.8574	0.0000
-12.3350	14.6643	0.0000
-12.0004	14.4711	0.0000
-11.6659	14.2780	0.0000
-11.3312	14.0847	0.0000
-10.9966	13.8916	0.0000
-10.6621	13.6984	0.0000
-10.3275	13.5052	0.0000
-9.9929	13.3121	0.0000
-9.6583	13.1189	0.0000
-9.3237	12.9258	0.0000
-8.9892	12.7326	0.0000
-8.6546	12.5393	0.0000
-8.3200	12.3462	0.0000
-7.9854	12.1530	0.0000
-7.6508	11.9599	0.0000
-7.3162	11.7667	0.0000
-6.9816	11.5735	0.0000
-6.6471	11.3804	0.0000
-6.3125	11.1871	0.0000
-5.9779	10.9940	0.0000
-5.6433	10.8008	0.0000
-5.3087	10.6077	0.0000
-4.9741	10.4145	0.0000
-4.6396	10.2213	0.0000
-4.3050	10.0282	0.0000
-3.9704	9.8349	0.0000
-3.6358	9.6418	0.0000
-3.3012	9.4486	0.0000
-2.9666	9.2555	0.0000
-1.6283	8.5133	0.0000

-1.2937	8.3851	0.0000
-0.9591	8.2891	0.0000
-0.6245	8.2230	0.0000
-0.2900	8.1853	0.0000
0.0000	8.1750	0.0000
0.0627	8.1752	0.0000
0.1254	8.1760	0.0000
0.1881	8.1771	0.0000
0.2508	8.1788	0.0000
0.3135	8.1810	0.0000
0.3762	8.1837	0.0000
0.4388	8.1868	0.0000
0.5014	8.1904	0.0000
0.5640	8.1945	0.0000
0.6266	8.1990	0.0000
0.6891	8.2041	0.0000
0.7515	8.2096	0.0000
0.8140	8.2156	0.0000
0.8763	8.2221	0.0000
0.9387	8.2290	0.0000
1.0009	8.2365	0.0000
1.0632	8.2444	0.0000
1.1253	8.2528	0.0000
1.1874	8.2617	0.0000
1.2494	8.2711	0.0000
1.3114	8.2809	0.0000
1.3732	8.2912	0.0000
1.4350	8.3020	0.0000
1.4967	8.3132	0.0000
1.5583	8.3249	0.0000
1.6198	8.3371	0.0000
1.6813	8.3498	0.0000
1.7426	8.3629	0.0000
1.8038	8.3765	0.0000
1.8649	8.3906	0.0000
1.9259	8.4051	0.0000
1.9868	8.4201	0.0000
2.0476	8.4356	0.0000
2.1083	8.4516	0.0000
2.1688	8.4679	0.0000
2.2292	8.4848	0.0000
2.2895	8.5022	0.0000
2.3496	8.5199	0.0000
2.4096	8.5382	0.0000
2.4695	8.5569	0.0000
2.5292	8.5761	0.0000
2.5888	8.5957	0.0000
2.6482	8.6158	0.0000
2.7074	8.6363	0.0000
2.7665	8.6573	0.0000
2.8255	8.6788	0.0000
2.8842	8.7007	0.0000
2.9428	8.7231	0.0000
3.0013	8.7459	0.0000
3.0595	8.7691	0.0000
3.1176	8.7928	0.0000
3.1755	8.8169	0.0000
3.2332	8.8415	0.0000
3.2907	8.8665	0.0000
3.3480	8.8920	0.0000
3.4051	8.9179	0.0000

3.4620	8.9443	0.0000
3.5187	8.9710	0.0000
3.5752	8.9982	0.0000
3.6315	9.0259	0.0000
3.6876	9.0540	0.0000
3.7435	9.0824	0.0000
3.7991	9.1114	0.0000
3.8545	9.1408	0.0000
3.9097	9.1706	0.0000
3.9647	9.2007	0.0000
4.0194	9.2314	0.0000
4.0739	9.2624	0.0000
4.1282	9.2939	0.0000
4.1822	9.3258	0.0000
4.2359	9.3581	0.0000
4.2895	9.3908	0.0000
4.3427	9.4239	0.0000
4.3957	9.4574	0.0000
4.4485	9.4913	0.0000
4.5010	9.5257	0.0000
4.5532	9.5603	0.0000
4.6051	9.5955	0.0000
4.6568	9.6310	0.0000
4.7082	9.6669	0.0000
4.7594	9.7032	0.0000
4.8102	9.7399	0.0000
4.8608	9.7771	0.0000
4.9111	9.8146	0.0000
4.9611	9.8524	0.0000
5.0108	9.8907	0.0000
5.0602	9.9293	0.0000
5.1093	9.9683	0.0000
5.1581	10.0077	0.0000
5.2066	10.0475	0.0000
5.2523	10.0855	0.0000
5.5869	10.3649	0.0000
6.1536	10.8327	0.0000
6.7340	11.3046	0.0000
7.3299	11.7818	0.0000
7.5730	11.9744	0.0000
7.9431	12.2653	0.0000
8.3201	12.5587	0.0000
8.7046	12.8551	0.0000
9.0971	13.1548	0.0000
9.4981	13.4580	0.0000
10.0470	13.8681	0.0000
10.4702	14.1805	0.0000
10.9040	14.4975	0.0000
11.0508	14.6040	0.0000
11.4993	14.9270	0.0000
11.8045	15.1448	0.0000
12.1153	15.3651	0.0000
12.4316	15.5877	0.0000
12.5916	15.6995	0.0000
12.9164	15.9254	0.0000
13.2473	16.1536	0.0000
13.5839	16.3843	0.0000
13.7542	16.5003	0.0000
14.1001	16.7342	0.0000
14.4523	16.9706	0.0000
14.8108	17.2093	0.0000

15.1757	17.4504	0.0000
15.5472	17.6935	0.0000
15.9251	17.9390	0.0000
16.3097	18.1864	0.0000
16.7009	18.4361	0.0000
17.0985	18.6876	0.0000
17.5029	18.9411	0.0000
17.9136	19.1965	0.0000
18.3311	19.4536	0.0000
18.7549	19.7121	0.0000
18.9692	19.8420	0.0000
19.1850	19.9722	0.0000
19.6215	20.2335	0.0000
19.8418	20.3645	0.0000
20.0635	20.4957	0.0000
20.2866	20.6272	0.0000
20.5112	20.7589	0.0000
20.9646	21.0228	0.0000
21.1931	21.1548	0.0000
21.4229	21.2869	0.0000
21.6538	21.4191	0.0000
21.8860	21.5513	0.0000
22.3539	21.8158	0.0000
22.5892	21.9478	0.0000
22.8254	22.0798	0.0000
23.3008	22.3433	0.0000
23.5395	22.4746	0.0000
23.7789	22.6057	0.0000
24.0190	22.7366	0.0000
24.5009	22.9970	0.0000
24.7422	23.1266	0.0000
24.9838	23.2557	0.0000
25.4677	23.5122	0.0000
25.7094	23.6395	0.0000
26.1924	23.8918	0.0000
26.6733	24.1406	0.0000
27.1512	24.3856	0.0000
27.6246	24.6259	0.0000
28.3224	24.9759	0.0000
28.7758	25.2008	0.0000
29.2166	25.4176	0.0000
29.8441	25.7229	0.0000
30.2286	25.9081	0.0000
30.4048	25.9926	0.0000
30.9365	26.2455	0.0000
31.4436	26.4844	0.0000
31.9615	26.7259	0.0000
32.4898	26.9697	0.0000
33.0287	27.2160	0.0000
33.5781	27.4644	0.0000
33.8567	27.5893	0.0000
34.4218	27.8409	0.0000
34.9973	28.0943	0.0000
35.5829	28.3491	0.0000
36.1788	28.6056	0.0000
36.7846	28.8636	0.0000
37.4002	29.1226	0.0000
37.7115	29.2525	0.0000
38.3419	29.5132	0.0000
38.6603	29.6438	0.0000
39.3046	29.9055	0.0000

39.9578	30.1676	0.0000
40.6202	30.4302	0.0000
41.2912	30.6930	0.0000
41.9709	30.9559	0.0000
42.6588	31.2187	0.0000
43.3549	31.4812	0.0000
44.0582	31.7431	0.0000
44.7694	32.0046	0.0000
45.4879	32.2652	0.0000
46.2128	32.5246	0.0000
46.9442	32.7831	0.0000
47.6820	33.0405	0.0000
48.4258	33.2963	0.0000
49.1751	33.5507	0.0000
49.5512	33.6771	0.0000
50.3067	33.9284	0.0000
51.0665	34.1776	0.0000
51.8302	34.4248	0.0000
52.5970	34.6695	0.0000
53.3666	34.9119	0.0000
54.1386	35.1516	0.0000
54.9125	35.3886	0.0000
55.6878	35.6227	0.0000
56.4642	35.8541	0.0000
57.2417	36.0825	0.0000
58.0199	36.3079	0.0000
58.7993	36.5306	0.0000
59.5801	36.7505	0.0000
60.3628	36.9679	0.0000
61.1482	37.1832	0.0000
61.9374	37.3962	0.0000
62.7321	37.6079	0.0000
63.5336	37.8182	0.0000
64.3435	38.0278	0.0000
65.1631	38.2368	0.0000
65.9945	38.4456	0.0000
66.8404	38.6548	0.0000
67.7017	38.8647	0.0000
68.5806	39.0755	0.0000
69.4782	39.2874	0.0000
70.3962	39.5005	0.0000
71.3355	39.7149	0.0000
72.2974	39.9306	0.0000
73.2823	40.1476	0.0000
74.2903	40.3657	0.0000
74.8032	40.4752	0.0000
75.3222	40.5849	0.0000
75.8469	40.6947	0.0000
76.3777	40.8047	0.0000
76.9144	40.9147	0.0000
77.4571	41.0250	0.0000
78.0060	41.1354	0.0000
78.5605	41.2458	0.0000

Appendix B: Spectrum plots

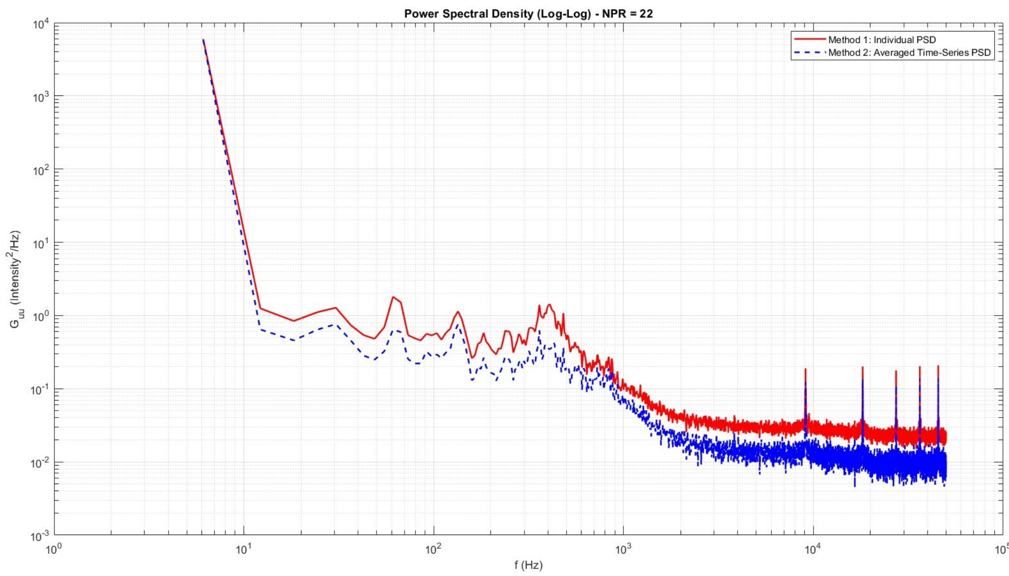

Non-premultiplied PSD at NPR=22

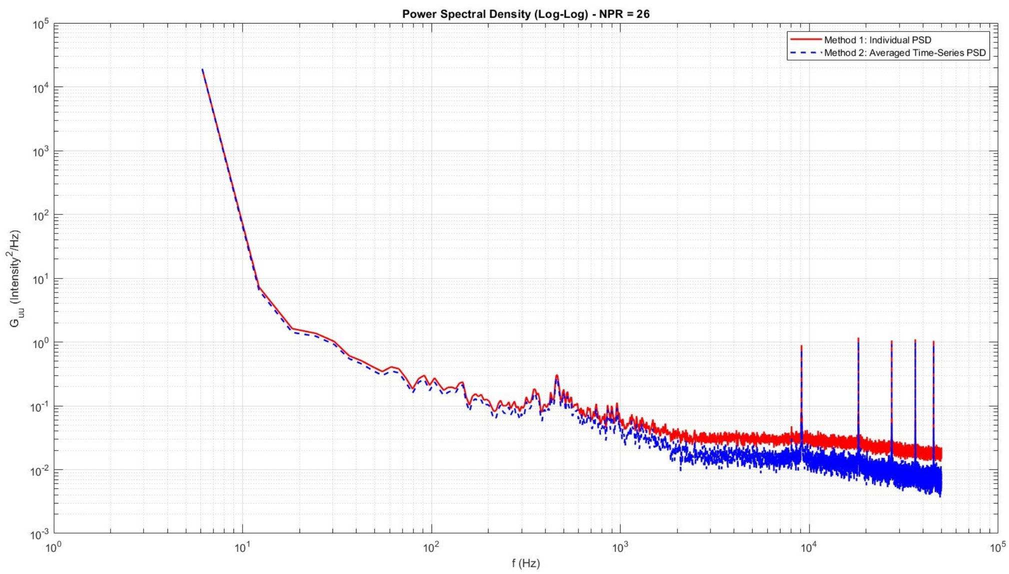

Non-premultiplied PSD at NPR=26

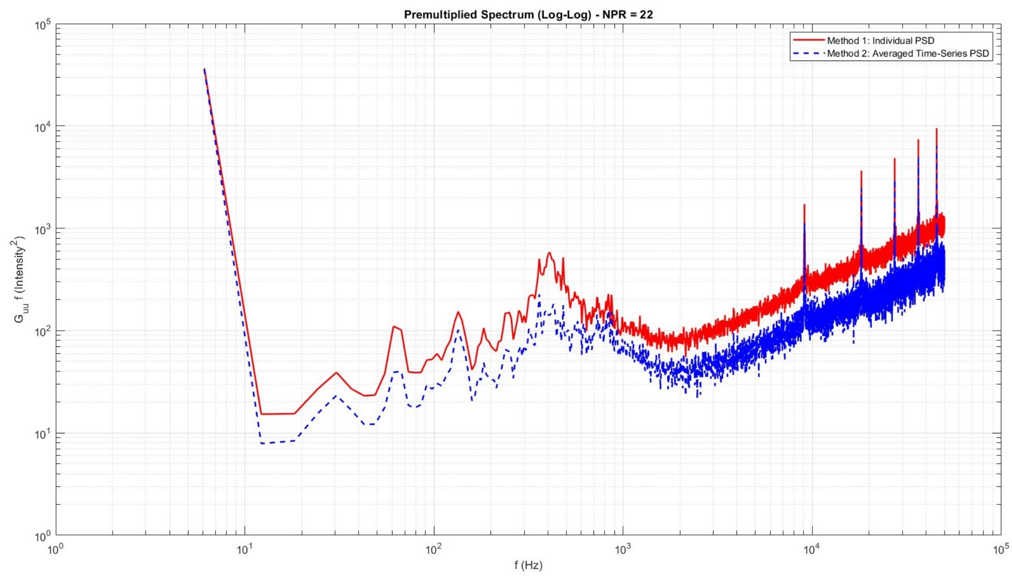

Premultiplied PSD at NPR=22

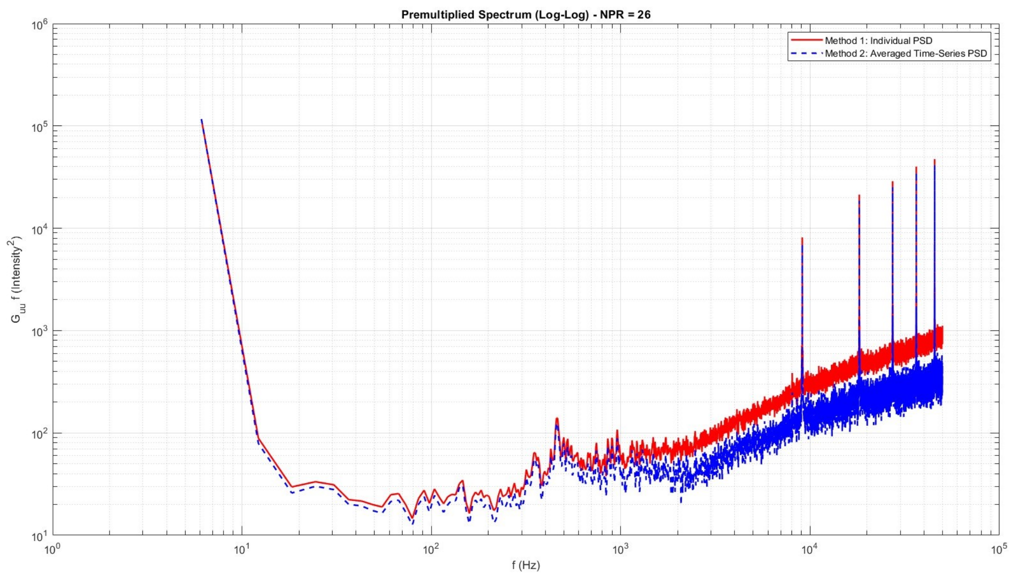

Premultiplied PSD at NPR=26

Appendix C: Technical drawings

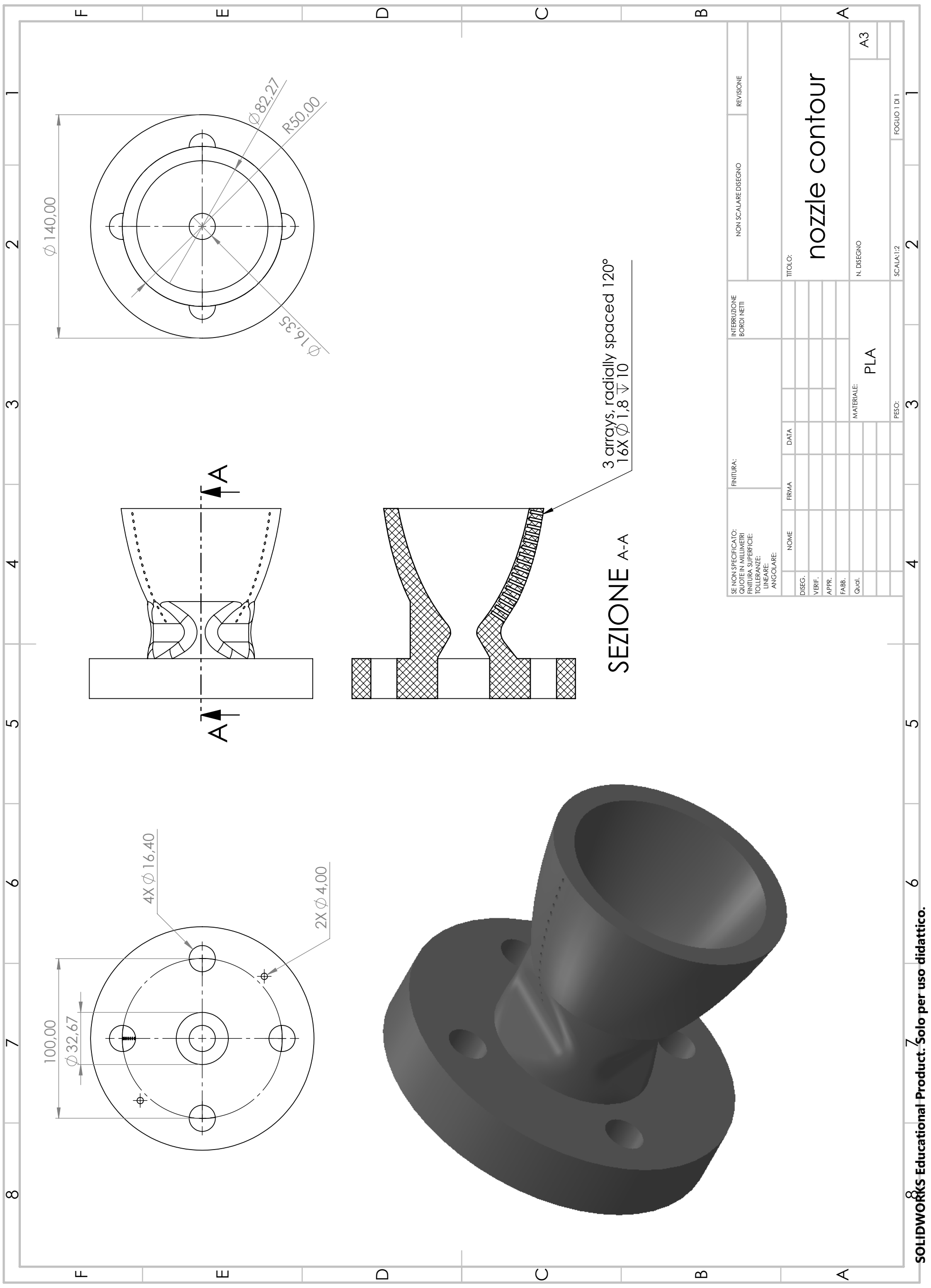

Bibliography

[1] J. H. Ahlberg, S. Hamilton, D. Migdal, and E. N. Nilson. «Truncated Perfect Nozzles in Optimum Nozzle Design». In: *ARS Journal* 31.5 (1961), pp. 614–620. DOI: 10.2514/8.5577. eprint: https://doi.org/10.2514/8.5577. URL: https://doi.org/10.2514/8.5577 (cit. on p. 6).

[2] Manuel Frey and Gerald Hagemann. «Restricted Shock Separation in Rocket Nozzles». In: *Journal of Propulsion and Power* 16.3 (May 2000), pp. 478–484. ISSN: 0748-4658, 1533-3876. DOI: 10.2514/2.5593. URL: https://arc.aiaa.org/doi/10.2514/2.5593 (cit. on pp. 10, 14–17).

[3] George P. Sutton and Oscar Biblarz. *Rocket Propulsion Elements*. 7th. New York: John Wiley & Sons, 2001. ISBN: 9780471326427 (cit. on p. 11).

[4] H. Babinsky and J. Harvey, eds. *Shock Wave-Boundary-Layer Interactions*. 1st ed. Cambridge Aerospace Series. Cambridge: Cambridge University Press, 2011. ISBN: 978-0-521-84852-7 (cit. on p. 9).

[5] J. M. Délery and J. G. Marvin. *Shock wave - boundary layer interactions*. Tech. rep. Tech. Rep., 1986 (cit. on p. 12).

[6] D. S. Dolling. «Fluctuating Loads in Shock Wave/Turbulent Boundary Layer Interaction: Tutorial and Update». In: *31st Aerospace Sciences Meeting*. Reno, NV, U.S.A.: American Institute of Aeronautics and Astronautics, Jan. 1993. DOI: 10.2514/6.1993-284. URL: http://arc.aiaa.org/doi/10.2514/6.1993284 (cit. on p. 11).

[7] Jean-Paul Dussauge, Pierre Dupont, and Jean-François Debiève. «Unsteadiness in Shock Wave Boundary Layer Interactions with Separation». In: *Aerospace Science and Technology* 10.2 (Mar. 2006), pp. 85–91. ISSN: 1270-9638. DOI: 10.1016/j.ast.2005.09.006. URL: https://linkinghub.elsevier.com/retrieve/pii/S1270963805001495 (cit. on p. 11).

[8] M. E. Erengil and D. S. Dolling. «Physical Causes of Separation Shock Unsteadiness in Shock Wave Turbulent Boundary Layer Interactions». In: *AIAA 24th Fluid Dynamics Conference*. AIAA 93-3134. American Institute of Aeronautics and Astronautics. Orlando, FL, USA, Jan. 1993 (cit. on p. 12).

[9] O. Ünalmis and D. S. Dolling. «Decay of Wall Pressure Field and Structure of a Mach 5 Adiabatic Turbulent Boundary Layer». In: *Fluid Dynamics Conference*. Colorado Springs, CO, U.S.A.: American Institute of Aeronautics and Astronautics, June 1994. DOI: 10.2514/6.1994-2363. URL: http://arc.aiaa.org/doi/10.2514/6.19942363 (cit. on p. 12).

[10] S. J. Beresh, N. T. Clemens, and D. S. Dolling. «Relationship Between Upstream Turbulent Boundary-Layer Velocity Fluctuations and Separation Shock Unsteadiness». In: *AIAA Journal* 40.12 (Dec. 2002), pp. 2412–2422. ISSN: 0001-1452, 1533-385X. DOI: 10.2514/2.1609. URL: https://arc.aiaa.org/doi/10.2514/2.1609 (cit. on p. 12).

[11] B. Ganapathisubramani, N. T. Clemens, and D. S. Dolling. «Effects of Upstream Boundary Layer on the Unsteadiness of Shock-Induced Separation». In: *Journal of Fluid Mechanics* 585 (Aug. 2007), pp. 369–394. ISSN: 0022-1120, 1469-7645. DOI: 10.1017/S0022112007006799. URL: https://www.cambridge.org/core/product/identifier/S0022112007006799/type/journal_article (cit. on p. 12).

[12] S. Piponniau, J.-P. Dussauge, J.-F. Debiève, and P. Dupont. «A Simple Model for Low-Frequency Unsteadiness in Shock-Induced Separation». In: *Journal of Fluid Mechanics* 629 (June 2009), pp. 87–108. ISSN: 0022-1120, 1469-7645. DOI: 10.1017/S0022112009006417. URL: https://www.cambridge.org/core/product/identifier/S0022112009006417/type/journal_article (cit. on p. 12).

[13] Stephan Priebe and M. Pino Martín. «Low-Frequency Unsteadiness in Shock Wave–Turbulent Boundary Layer Interaction». In: *Journal of Fluid Mechanics* 699 (May 2012), pp. 1–49. ISSN: 0022-1120, 1469-7645. DOI: 10.1017/jfm.2011.560. URL: https://www.cambridge.org/core/product/identifier/S002211201100560X/type/journal_article (cit. on p. 12).

[14] L. Prandtl. «Ueber Fluessigkeitsbewegung bei sehr kleiner Reibung». In: *International Mathematical Congress*. On Fluid Movement at Low Friction (in German). Heidelberg, 1904 (cit. on p. 13).

[15] G. Hagemann, M. Frey, and W. Koschel. «Appearance of Restricted Shock Separation in Rocket Nozzles». In: *Journal of Propulsion and Power* 18.3 (May 2002), pp. 577–584. ISSN: 0748-4658, 1533-3876. DOI: 10.2514/2.5971. URL: https://arc.aiaa.org/doi/10.2514/2.597 (cit. on pp. 15, 17, 18, 31).

[16] Anh Thi Nguyen, H. Deniau, S. Girard, and T. Alziary de Roquefort. «Unsteadiness of Flow Separation and End-Effects Regime in a Thrust-Optimized Contour Rocket Nozzle». In: *Flow, Turbulence and Combustion* 71 (2003).

© 2004 Kluwer Academic Publishers, pp. 161–181. DOI: 10.1023/B:APPL.0000024894.92054.98 (cit. on p. 16).

[17] M. Frey and G. Hagemann. «Status of Flow Separation Prediction in Rocket Nozzles». In: *AIAA Paper 98-3619*. American Institute of Aeronautics and Astronautics. 1998 (cit. on p. 16).

[18] M. Frey and G. Hagemann. «Flow separation and side loads in rocket nozzles». In: *AIAA Paper*. 99-2815. 1999 (cit. on p. 17).

[19] L. H. Nave and G. A. Coffey. «Sea level side loads in high-area-ratio rocket engines». In: *AIAA Paper*. 73-1284. 1973 (cit. on p. 17).

[20] M. Frey, R. Stark, H.K. Ciezki, F. Quessard, and W. Kwan. «Sub-scale nozzle testing at the P6.2 test stand». In: *AIAA Paper*. 2000-3777. 2000 (cit. on p. 17).

[21] Sébastien Deck. «Delayed detached eddy simulation of the end-effect regime and side-loads in an overexpanded nozzle flow». In: *Shock Waves* 19 (2009), pp. 239–249. DOI: 10.1007/s00193-009-0199-5 (cit. on p. 18).

[22] Emanuele Martelli, Francesco Nasuti, and Marcello Onofri. «Numerical calculation of FSS/RSS transition in highly overexpanded rocket nozzle flows». In: *Shock Waves* 20.2 (Apr. 2010), pp. 139–146. ISSN: 0938-1287, 1432-2153. DOI: 10.1007/s0019300902444. URL: http://link.springer.com/10.1007/s0019300902444 (cit. on p. 17).

[23] Joseph H. Ruf, David M. McDaniels, and Andrew M. Brown. «Nozzle Side Load Testing and Analysis at Marshall Space Flight Center». In: *NASA Marshall Space Flight Center* (2009) (cit. on p. 19).

[24] Jan Östlund. *Flow Processes in Rocket Engine Nozzles with Focus on Flow Separation and Side-Loads*. Licentiate Thesis TRITA-MEK Technical Report 2002:09. Stockholm, Sweden: Royal Institute of Technology, 2002. ISRN: KTH/MEK/TR–02/09-SE (cit. on pp. 19–21).

[25] G. S. Settles. *Schlieren and Shadowgraph Techniques: Visualizing Phenomena in Transparent Media*. Springer, 2001 (cit. on p. 22).

[26] K. de Kievit. «Development of Rocket Nozzle Test Facility for Measurements of Fluid-Structure Interaction Phenomena». Copyright © 2021 Krijn de Kievit. Master's thesis. Faculty of Aerospace Engineering: Delft University of Technology, July 2021 (cit. on pp. 23, 31, 36, 41).

[27] John A. Valdez and Charles E. Tinney. «Measurements of a Mach 3 Jet Using High-Speed Optical Flow Techniques». In: *Proceedings of the 2018 AIAA/CEAS Aeroacoustics Conference*. Atlanta, Georgia: American Institute of Aeronautics and Astronautics, 2018. DOI: 10.2514/6.2018-3148 (cit. on p. 23).

[28] G. S. Settles, T. J. Fitzpatrick, and S. M. Bogdonoff. «Detailed Study of Attached and Separated Compression Corner Flowfields at High Reynolds Number Supersonic Flow». In: *AIAA Journal* 17.6 (1979), pp. 579–585. DOI: 10.2514/3.61100 (cit. on p. 25).

[29] R. L. Maltby. *Flow Visualization in Wind Tunnels Using Indicators*. AGARDograph. NATO, Rue de Varenne, Paris VII: Advisory Group for Aerospace Research and Development, Apr. 1962 (cit. on p. 25).

[30] S. B. Verma and O. Haidn. «Study on Restricted Shock Separation Phenomena in Rocket Nozzles». In: *44th AIAA Aerospace Sciences Meeting and Exhibit*. AIAA-2006-1431. Reno, Nevada: AIAA, Jan. 2006 (cit. on p. 26).

[31] W. J. Baars and C. E. Tinney. «Transient wall pressures in an overexpanded and large area ratio nozzle». In: *Experiments in Fluids* 54 (2013), p. 1468. DOI: 10.1007/s00348-013-1468-8 (cit. on pp. 27, 66).

[32] Joseph Ruf, David McDaniels, and Andrew Brown. «Details of Side Load Test Data and Analysis for a Truncated Ideal Contour Nozzle and a Parabolic Contour Nozzle». In: *46th AIAA/ASME/SAE/ASEE Joint Propulsion Conference & Exhibit*. Nashville, TN: American Institute of Aeronautics and Astronautics, 2010. ISBN: 9781600869587. DOI: 10.2514/6.2010-6813. URL: http://arc.aiaa.org/doi/abs/10.2514/6.20106813 (cit. on p. 31).

[33] Joseph H. Ruf, David M. McDaniels, and Andrew M. Brown. «Nozzle Side Load Testing and Analysis at Marshall Space Flight Center». In: *AIAA Journal* (2009), p. 14 (cit. on p. 31).

[34] Woutijn J. Baars, Charles E. Tinney, Joseph H. Ruf, Andrew M. Brown, and David M. McDaniels. «Wall Pressure Unsteadiness and Side Loads in Overexpanded Rocket Nozzles». In: *AIAA Journal* 50.1 (Jan. 2012), pp. 61–73. ISSN: 0001-1452, 1533-385X. DOI: 10.2514/1.J051075. URL: https://arc.aiaa.org/doi/10.2514/1.J051075 (cit. on p. 31).

[35] M. Frey. «Behandlung von Strömungsproblemen in Raketendüsen bei Überexpansion». PhD thesis. Stuttgart, Germany: Stuttgart University, Jan. 2001 (cit. on p. 31).

[36] Wiehan Kwan and Ralf Stark. «Flow Separation Phenomena in Subscale Rocket Nozzles». In: *38th AIAA/ASME/SAE/ASEE Joint Propulsion Conference & Exhibit*. Indianapolis, Indiana: American Institute of Aeronautics and Astronautics, 2002. ISBN: 9781624101151. DOI: 10.2514/6.2002-4229. URL: http://arc.aiaa.org/doi/abs/10.2514/6.20024229 (cit. on p. 31).

[37] J. Mattsson, U. Högman, and L. Törngren. «A Subscale Test Programme on Investigation of Flow Separation and Side Loads in Rocket Nozzles». In: *Proceedings of the 3rd European Symposium on Aerothermodynamics of Space Vehicles*. The Netherlands: ESA-ESTEC, Nov. 1998 (cit. on p. 31).

[38] Jan Östlund, Tomas Damgaard, and Manuel Frey. «Side-Load Phenomena in Highly Overexpanded Rocket Nozzles». In: *Journal of Propulsion and Power* 20.4 (July 2004), pp. 695–704. ISSN: 0748-4658, 1533-3876. DOI: 10.2514/1.3059. URL: https://arc.aiaa.org/doi/10.2514/1.3059 (cit. on p. 31).

[39] Anh Nguyen, H. Deniau, S. Girard, and T. Alziary de Roquefort. «Wall Pressure Fluctuations in an Overexpanded Rocket Nozzle». In: *38th AIAA/ASME/SAE/ASEE Joint Propulsion Conference & Exhibit*. Indianapolis, Indiana: American Institute of Aeronautics and Astronautics, July 2002. ISBN: 9781624101151. DOI: 10.2514/6.2002-4001. URL: http://arc.aiaa.org/doi/abs/10.2514/6.20024001 (cit. on p. 31).

[40] Raymundo Rojo, Charles E. Tinney, and Joseph H. Ruf. «Effect of Stagger on the Vibroacoustic Loads from Clustered Rockets». In: *AIAA Journal* 54.11 (Nov. 2016), pp. 3588–3597. ISSN: 0001-1452, 1533-385X. DOI: 10.2514/1.J055017. URL: http://arc.aiaa.org/doi/10.2514/1.J055017 (cit. on p. 31).

[41] Charles E. Tinney, Kenneth Scott, Mandi Routon, Jayant Sirohi, and Joseph Ruf. «Effect of Aeroelasticity on Vibroacoustic Loads during Startup of Large Area Ratio Nozzles». In: *23rd AIAA/CEAS Aeroacoustics Conference*. Denver, Colorado: American Institute of Aeronautics and Astronautics, June 2017. ISBN: 9781624105043. DOI: 10.2514/6.2017-3361. URL: https://arc.aiaa.org/doi/10.2514/6.20173361 (cit. on p. 31).

[42] Takeo Tomita, Mamoru Takahashi, Masahiro Takahashi, Shuichi Ueda, Hiroshi Tamura, and Kenji Aoki. «Visualization of the Formation of Separation Bubbles on a Bell-Shaped Nozzle Surface in Relation to Serious Side-Load». In: *37th Joint Propulsion Conference and Exhibit*. Salt Lake City, UT, U.S.A.: American Institute of Aeronautics and Astronautics, July 2001. DOI: 10.2514/6.2001-3559. URL: http://arc.aiaa.org/doi/10.2514/6.20013559 (cit. on p. 31).

[43] Changjin Yoon, Yu Matsutomi, William Anderson, and Charles Merkle. «Investigation of the Cap-Shock Pattern in a Thrust-Optimized Rocket Nozzle». In: *47th AIAA/ASME/SAE/ASEE Joint Propulsion Conference & Exhibit*. San Diego, California: American Institute of Aeronautics and Astronautics, July 2011. ISBN: 9781600869495. DOI: 10.2514/6.2011-5685. URL: http://arc.aiaa.org/doi/abs/10.2514/6.20115685 (cit. on p. 31).

[44] Afaque Shams, Stève Girard, and Pierre Comte. «Detached Eddy Simulation of Restricted Shock Separated Flow in a Thrust Optimized Contoured Nozzle». In: *CFM 2009 - 19ème Congrès Français de Mécanique*. hal-03378285. Marseille, France, Aug. 2009 (cit. on p. 33).

[45] M. Formidabile. «Effect of Aeroelasticity on the Acoustic Signature of TOP Contoured Rocket Nozzles in Overexpanded Conditions». Defended publicly on May 22, 2023 at 14:30. Master's thesis. Delft, Netherlands: Delft University of Technology, 2023. URL: `http://repository.tudelft.nl/` (cit. on p. 36).

[46] R. Schmucker. *Flow Processes in Overexpanding Nozzles of Chemical Rocket Engines*. Tech. rep. TB-7, -10, -14. Munich, Germany: Technical University Munich, 1973 (cit. on p. 37).

[47] J. Östlund and B. Muhammad-Klingmann. «Supersonic Flow Separation with Application to Rocket Engine Nozzles». In: *Journal of Fluids Engineering* 126.3 (2004). Volvo-Aero Corporation, S-461 SI Trollhättan, Sweden and Department of Mechanics, Royal Institute of Technology, S-144 00 Stockholm, Sweden, pp. 498–505. DOI: `10.1115/1.1894402` (cit. on p. 37).

[48] R.H. Schmucker. *Flow Processes in Overexpanded Chemical Rocket Nozzles. Part 2: Side Loads due to Asymmetric Separation*. Tech. rep. TM77395. Santa Barbara, USA: NASA, Feb. 1984 (cit. on p. 38).

[49] *ST-15 Supersonic Wind Tunnel - TU Delft*. `https://www.tudelft.nl/en/ae/organisation/departments/flow-physics-and-technology/facilities/high-speed-wind-tunnels/st-15-supersonic-windtunnel`. Accessed: 2024-10-22. 2024 (cit. on p. 40).

[50] Scanivalve. *DSA3217 PTP Pressure Scanner*. Accessed: 2024-10-23. 2024. URL: `https://scanivalve.com/products/pressure-measurement/ethernet-intelligent-pressure-scanners/dsa3217-ptp-pressure-scanner/` (cit. on p. 42).

[51] Photron. *FASTCAM SA1.1 / FASTCAM SA1.1 RV Hardware Manual. Rev. 1.13 E*. Hardware Manual (cit. on p. 47).

[52] Photron. *Fastcam Nova S*. Accessed: March 10, 2025. URL: `https://photron.com/fr/fastcam-nova-s/` (visited on 03/10/2025) (cit. on p. 47).

[53] Ralf Stark, Dirk Schneider, Jan Martin, and Stephan General. «Experimental Study on Jet Acoustics of Subscale Rocket Nozzles with a Different Divergent Contour Design». In: *8th European Conference for Aeronautics and Space Sciences (EUCASS)*. German Aerospace Center. Lampoldshausen, Germany: EUCASS Association, 2019 (cit. on p. 58).

[54] S. B. Verma and O. Haidn. «Study of Restricted Shock Separation Phenomena in a Thrust Optimized Parabolic Nozzle». In: *Journal of Propulsion and Power* 25.5 (Sept. 2009), pp. 1108–1117. DOI: `10.2514/1.42351` (cit. on p. 58).

[55] J. Östlund and B. Muhammad-Klingmann. «Supersonic Flow Separation with Application to Rocket Engine Nozzles». In: *Applied Mechanics Reviews* 58.3 (2005), p. 143. DOI: `10.1115/1.1894402` (cit. on p. 65).